Acoustics-induced Fluid Motions

by

Chuyi Chen

Department of Mechanical Engineering and Materials Science
Duke University

Date:_____
Approved:

_____
Tony Jun Huang, Advisor

_____
Steven A. Cummer

_____
Erica E. Davis

_____
Benjamin B. Yellen

_____
Po-Chun Hsu

Dissertation submitted in partial fulfillment of the requirements
for the degree of Doctor of Philosophy in the Department of
Mechanical Engineering and Materials Science
in the Graduate School of Duke University

2021

ABSTRACT

Acoustics-induced Fluid Motions

by

Chuyi Chen

Department of Mechanical Engineering and Materials Science
Duke University

Date:_____
Approved:

_____
Tony Jun Huang, Advisor

_____
Steven A. Cummer

_____
Erica E. Davis

_____
Benjamin B. Yellen

_____
Po-Chun Hsu

An abstract of a dissertation submitted in partial fulfillment of the requirements for the degree of Doctor of Philosophy in the Department of Mechanical Engineering and Materials Science in the Graduate School of Duke University

2021

Copyright by
Chuyi Chen
2021

Abstract

Acoustic waves, as a form of mechanical vibration, not only induces the force directly on the object, but also induces the motion of the medium that propagates throughout the system. The study of acoustofluidic mainly focuses on the exploration of the underlying mechanism of the acoustic waves and fluid motion and the methodology of applying this technique to practical applications. Featuring its contactless, versatile, and biocompatible capabilities, the acoustofluidic method makes itself an ideal tool for biosample handling. As the majority of the bio-related samples (e.g., cell, small organism, exosome) possess their native environment within liquids, there is an urgent need to study the acoustic induced fluid motion in order to cooperate with the development of the acoustic tweezing technique. While both the theoretical study and application exploration have been established for the combination of acoustics and microfluidics, the fluid motion on a larger scale is still under-developed. One reason is that, although the acoustofluidic methods hold great potential in various biomedical applications, there is a limited way to form an organized motion in a larger fluid domain, which may lead to the imprecise manipulation of the target. On the other hand, the theoretical study for the microfluidic domain is on the basis of a simplified model with certain assumptions, when applying to the larger fluid area, and significantly influences both the accuracy and computation cost.

In this dissertation, we have first developed a series of theoretical and numerical methods in order to provide insights into the acoustofluidic phenomenon in different domain scales. Specifically, we explored the non-linear acoustic dynamics in fluids with the perturbation theory and Reynolds' stress theory. Then we presented that the vortex streaming can be predicted and designed with our theoretical and numerical study, which can be utilized for various fluid systems and expanded to practical biomedical applications. The boundary-driven streaming and Reynolds' stress-induced streaming are studied and applied to the digital acoustofluidic droplet handling platform and droplet spinning system, respectively. We demonstrated that within the digital acoustofluidic platform, the droplet can be manipulated on the oil layer in a dynamic and biocompatible manner. Meanwhile, in the droplet spinning system, we can predict and guide the periodic liquid-air interface deformation, as well as the particle motion inside the droplet. We demonstrated that with the theoretical and experimental study, this platform can be utilized for the nanoscale particle (e.g., DNA molecule and exosome) concentration, separation, and transport.

Next, based on our study of the acoustically induced fluid motion, we developed an integrated acoustofluidic rotational tweezing platform that can be utilized for zebrafish larvae rapid rotation (~1s/rotation), multi-spectral imaging, and phenotyping. In this study, we have conducted a systematic study including theory development, acoustofluidic device design/fabrication, and flow system implementation. Moreover, we

have explored the multidisciplinary expansion combining the acoustofluidic zebrafish phenotyping device with the computer-vision-based 3D model reconstruction and characterization. With this method, we can obtain substantial information from a single zebrafish sample, including the 3D model, volume, surface area, and deformation ratio. Moreover, with the design of the continuous flow system, a flow-cytometry-like system was developed for zebrafish larvae morphological phenotyping. In this study, a standard workflow is established which can directly transfer the groups of samples to a statistical digital readout and provide a new guideline for applying acoustofluidic techniques to biomedical applications. This work represents a complete fusion of acoustofluidic theory, experimental function, and practical application implementation.

Dedication

This dissertation is dedicated to my family.

Table of Contents

Abstract iv

List of Tables xiii

List of Figures xiv

Acknowledgements xix

1. Introduction and Background 1

1.1 Acoustics induced fluid motion 1

1.1.1 Basics of acoustic waves 1

1.1.2 Acoustic streaming 3

1.1.3 Acoustic induced interface deformation 4

1.2 Acoustofluidic based object manipulation 6

1.2.1 Micro/Nanoscale particle manipulation 6

1.2.2 Droplet manipulation 9

1.2.3 Small organism manipulation 11

1.3 Dissertation outline 12

2. Theoretical Aspects of Acoustofluidics 15

2.1 Motivation 15

2.1 SAWs in piezoelectric substrate 18

2.2 Non-linear acoustic dynamics in the fluids 19

2.2.1 Perturbation theory 19

2.2.2 Reynolds' stress 23

2.3 Particle motion 24

2.3.1 Acoustic radiation force (ARF) 24
2.3.2 Drag force 26
2.4 Summary 26
3. Vortex-streaming Acoustofluidics 28
3.1 Acoustic streaming by standing SAWs 28
3.1.1 2D Numerical model 29
3.1.2 Boundary driven streaming 34
3.1.3 Slip Velocity Method 36
3.1.4 Validation of the slip Velocity Method 39
3.2 Vortex streaming generated by IDTs merged in the oil 45
3.2.1 Motivation 45
3.2.2 Numerical simulation 47
3.2.3 Droplet manipulation by the streaming pattern 62
3.2.4 Discussion and conclusion 66
3.3 Vortex streaming generated in spinning droplet 68
3.3.1 Motivation 68
3.3.2 SAW-induced fluid motion in the spinning droplet 70
3.3.3 Particle concentration in the spinning droplet 75
3.3.4 Nanoparticle isolation using the ARC 83
3.3.5 Discussion and conclusion 88
3.4 Summary 88
4. Zebrafish Phenotyping Using Acoustofluidic Rotational Tweezing Platform 89

4.1 Motivation 89
4.2 Generation of single vortex streaming 95
4.2.1 Designing principle 95
4.2.1 Numerical simulation 97
4.2.2 Effect of width of the effective IDT area (e) to the streaming pattern 100
4.2.3 Effect of channel width 103
4.2.4 Feasibility of zebrafish rotation 105
4.2.4 Conclusion 107
4.3 Device fabrication 108
4.4 Experimental validation of single vortex streaming pattern 110
4.4.1 Methods 110
4.4.2 Measurement of acoustic streaming 111
4.5 Rotational manipulation of zebrafish larvae 112
4.5.1 Zebrafish larvae preparation 113
4.5.2 Rotational manipulation of zebrafish larvae 113
4.5.3 Discussion 120
4.6 Conclusion 121
5. ART System with 3D Multispectral Imaging and 3D Reconstruction 124
5.1 Motivation 125
5.2 3D multispectral imaging using the ART device 127
5.2.1 Zebrafish larvae preparation 127
5.2.2 3D multispectral imaging 128

5.3 3D model reconstruction 131
5.3.1 Camera matrix 131
5.3.2 3D reconstruction pipeline 132
5.4 validation of the accuracy of the 3D models 136
5.4.1 Zebrafish larvae models 136
5.4.2 Zebrafish yolk models 140
5.4.1 Zebrafish liver models 141
5.4.1 Conclusion 142
5.5 Discussion and conclusion 143
6. Zebrafish Phenotyping Using the ART Platform 147
6.1 Motivation 147
6.2 Methods 148
6.2.1 Flow system 149
6.2.2 Zebrafish larvae preparation 152
6.2.3 Assessment of zebrafish health 153
6.3 Phenotype ethanol-induced morphological abnormalities in larval body 155
6.3.1 3D models 156
6.3.2 Quantification of morphological abnormalities based on 3D models 159
6.3.3 Zebrafish phenotyping based on the abnormality factor 165
6.4 Phenotype ethanol-induced morphological abnormalities in larval liver 168
6.5 Discussion and conclusion 172
7. Conclusion and Prospects 177

7.1 Achievements 177

7.2 Prospects 179

References 182

Biography 194

List of Tables

Table 3.1: Parameters used in the simulation (at 298K). 30

Table 3.2: Essential forces in the spinning droplet that effect the particle movement. 79

Table 6.1: Status of the acoustics, syringe pump, and valve in each mode of the flow system. 151

Table 6.2: Average time of each step. * Each time and standard deviation are averaged from n=20. 152

List of Figures

Figure 2.1: Illustration of SAWs propagation in piezoelectric substrate and the leaky SAWs in the liquid. 17

Figure 2.2: Rayleigh SAWs propagation in the elastic solid. 17

Figure 3.1: Cross-section of the channel in the classic standing surface acoustic wave (SAW) device..……..29

Figure 3.2: Color plots of solutions from the traditional approach.. 32

Figure 3.3: Variation of the normalized value of the line averages $\boldsymbol{gz}$ of the variables. . 34

Figure 3.4: Boundary driven streaming. 35

Figure 3.5: The change of the convergence functions the variables with respect to h, the thickness of the inner streaming domain. 40

Figure 3.6: Simulation domain of the 3D numerical model. 42

Figure 3.7: 3D streaming pattern in classic standing SAW device with one pair of IDTs.. 43

Figure 3.8: 3D streaming pattern in classic standing SAW device with two pairs of IDTs. 44

Figure 3.9: Illustration of the contactless droplet manipulation via boundary-driven streaming activated by an IDT. 47

Figure 3.10: Sketch of the computational domain in our SAW microfluidic device. 48

Figure 3.11: Simulation results in the substrate ($\boldsymbol{\Omega 1}$) and inner streaming domain ($\boldsymbol{\Omega 2}$) when the IDT was activated at the frequency of 23.9 MHz and the voltage of 40 V_{PP}..... 55

Figure 3.12: Numerical and experimental results of acoustic streaming in an outer oil domain ($\boldsymbol{\Omega 3}$) in our SAW microfluidic device. 57

Figure 3.13: Comparison of the numerical and experimental streaming pattern on 2D planes. 59

Figure 3.14: Droplet manipulation using the streaming pattern generated by the IDTs merged in the oil. 60

Figure 3.15: Droplet tracing in our SAW microfluidic device. 65

Figure 3.16: Droplet manipulation achieved using a SAW microfluidic device with 1×10 IDT arrays. 66

Figure 3.17: Schematic illustration of acoustic streaming in sessile droplet generated by SAW. 68

Figure 3.18: Simulation results of acoustic streaming pattern in the sessile droplet (radius: R) activated by SAW beams with different width. 70

Figure 3.19: Schematic illustration of the acoustofluidic centrifuge (AFC) system. 72

Figure 3.20: Image sequence of the droplet spinning motion taken from the side view. . 73

Figure 3.21: Measurement of the period of the droplet spinning motion. 73

Figure 3.22: Stacked particle trajectories showing the flow pattern in (a) a droplet without spin motion and (b) a droplet with spinning motion. 76

Figure 3.23: Numerical simulation results analyzing the mechanism of the particle concentration in the AFC system. 78

Figure 3.24: Particle movement in the spinning droplet. 82

Figure 3.25: Separation of the 28-nm particles and 100-nm particles using the AFC system. 82

Figure 3.26: Nano particle separation and transportation using the AFC system with two ring-confined droplets connected by a microchannel. 84

Figure 3.27: Numerical simulation to explore the flow pattern in the microchannel. 86

Figure 3.28: Separation and transport of the exosome subpopulations using the AFC.... 87

Figure 4.1: A 5 dpf zebrafish larva. The pigmentation (red arrows) obstructs the fluorescent imaging of the zebrafish liver……...91

Figure 4.2: Designing principle of the acoustofluidic chip and the geometric variables relative to device design..... 97

Figure 4.3: 3D domain of the numerical simulation..... 99

Figure 4.4: Simulation results showing the effect of width of the effective IDT area (e) to the streaming pattern. 102

Figure 4.5: Labeled schematic and geometric variables of the acoustofluidic rotational manipulation device. 104

Figure 4.6: The distribution of the body force (red arrows) and the streaming pattern (black streamlines) in the devices with a=1.34 mm (a) and a=0.8 mm (b). 105

Figure 4.7: Numerical Simulation results showing the streaming pattern with a zebrafish larva in the channel (a=1.34 mm) 106

Figure 4.8: Schematic illustration of the acoustofluidic rotational manipulation device. 108

Figure 4.9: Schematic illustration of the fabrication of the acoustic device. 109

Figure 4.10: Design of the mold for PDMS channel fabrication. 110

Figure 4.11: Experimental and numerical demonstration of acoustic streaming in the channel with a width of 1.34 mm (a) and 0.8 mm (b). 112

Figure 4.12: Zebrafish larvae rotational motion evaluation in a channel with 0.8×0.8 mm^2 in the cross section. 115

Figure 4.13: The performance of the acoustofluidic chip for high-speed, rotational manipulation of 5 dpf zebrafish larvae. 117

Figure 4.14: Comparison of zebrafish tail curling before (no vortex streaming), during (with vortex streaming), and after rotation (no vortex streaming). 119

Figure 4.15: Rotation and imaging of a zebrafish embryo (0 dpf, prior to tail extension). 121

Figure 5.1: The Shape-From-Silhouette problem scenario 126

Figure 5.2: Cytometry-like workflow of the acoustofluidic rotational tweezing (ART) platform. 127

Figure 5.3: Multispectral imaging of a 5 dpf 2CLIP zebrafish larva. 129

Figure 5.4: 3D multispectral imaging. 130

Figure 5.5: Silhouettes based 3D reconstruction. 135

Figure 5.6: Comparison between the optical microscope image sequence and projected 3D model images at the corresponding viewing angles. 136

Figure 5.7: Comparison between the Hough transform plots of the features of the microscope image and the projected image at 315° in Figure 5.6. 138

Figure 5.8: The binary cross-entropy loss for 3D reconstructed models of zebrafish larvae, livers, and pancreases. 140

Figure 5.9: Validation of the 3D reconstruction by reconstruction and size evaluation of a zebrafish yolk. 141

Figure 5.10: 3D reconstruction of the same liver based on image sequences captured in five rotation cycles. 142

Figure 5.11: Comparison of the silhouette outlines between the microscope images, digital re-projection images, and the re-projection images 144

Figure 6.1: A photo showing the assembled ART chip for zebrafish phenotyping……..149

Figure 6.2: Schematic representation of the operating modes of the flow system. 151

Figure 6.3: The processing time of the routine use of the ART platform for zebrafish 3D multispectral imaging. 153

Figure 6.4: Assessment of zebrafish health. 155

Figure 6.5: Procedure of using the ART system to phenotype ethanol-induced morphological abnormalities in zebrafish larval body. 156

Figure 6.6: 3D reconstructed models of zebrafish larvae. 157

Figure 6.7: An outline analysis in the transverse (y-z) plane for size differences along x-axis. 158

Figure 6.8: Distribution of normal vectors on the surface of reconstructed 3D models of a zebrafish larva. 160

Figure 6.9: The angle distribution and variance of normal vectors relative to the x-axis along the zebrafish body. 162

Figure 6.10: Distributions of the angle ($\boldsymbol{\theta}$) between normal vectors and the x-axis for zebrafish 3D models. 164

Figure 6.11: Gaussian fitting curves of the angle distribution statistics of 15 larvae in the control group. 165

Figure 6.12: Morphological phenotyping based on automated quantitative measurements. 166

Figure 6.13: Flow chart of the abnormal level characterization and pipeline for morphological abnormal criteria standardization. 167

Figure 6.14: Schematic illustration shows the setup for imaging zebrafish samples. 168

Figure 6.15: 3D models and quantification of zebrafish liver. 170

Figure 6.16: Outline contours from the projection of the typical reconstructed 3D model of a zebrafish liver in the (a) control and (b)1.5%-EtOH groups. 172

Acknowledgements

First and foremost, I would like to express my most sincere gratitude to my Ph.D. advisor, Prof. Tony Jun Huang, for his guidance and support. His guidance directed the completion of this dissertation. His trust gave me a free environment to conduct my research and his encouragement supported me to go through the challenges I met during the Ph.D. journey.

I would like to thank my dissertation committee, Prof. Erica Davis, Prof. Steven A. Cummer, Prof. Benjamin Yellen, and Prof. Po-chun Hsu for their valuable suggestions on my dissertation work. I would also like to acknowledge Prof. Francesco Costanzo, Prof. John Rawls, Prof. John D.H. Mai, Prof. Yun Jing, and Prof. Xiasheng Guo for their insightful suggestions and strong support to my research.

Additionally, I would like to thank my mentor Dr. Zhangming Mao for his friendship, patience, and guidance in my research. I am grateful to Dr. Nitesh Nama for his guidance on the numerical simulations and fruitful discussions during my studies. I am thankful to Yuyang Gu, Dr. Peiran Zhang, Dr. Hunter Bachman, Dr. Julien Philippe, and Jinxin Zhang for their immense support to each of my projects. My dissertation work was done in collaborations with so many great people within and outside of Acoustofluidic research group. My sincere thanks to Dr. Po-Hsun Huang, Dr. Zhenhua Tian, Dr. Mengxi Wu, Dr. Feng Guo, Dr. Adem Ozcelik, Dr. Nanjing Hao, Joseph Rufo, Pengzhan Liu, Hai Fu, Shujie Yang, Zeyu Wang, Shuaixiang Zhao, Haodong Zhu,

Geonsoo Jin, Jianping Xia, Zhehan Ma, Kaichun Yang, Ruoyu Zhong, Ty D. Naquin, Ryan Becker, Joseph T. Rich, Ye He, and Defei Liao for their help in many different ways. I would like to thank all the past and present members of the Acoustofluidics group.

I also want to thank the Department of Mechanical Engineering and Materials Science at Duke University for offering me this precious opportunity to work and study here. I also want to thank various funding agencies for my research.

Last but not least, I would like to express my love to my family. Their love, caring, tolerance, and support made this dissertation possible. I would also like to thank my friends who have always been there for me

1. Introduction and Background

Acoustofluidic techniques have brought extensive research interests due to its unique contactless, versatile, and biocompatible features, especially in life sciences studies(Ozcelik et al., 2018). While the majority of the biological samples are contained in the fluid environment, the acoustic induced fluid motion utility becomes an unavoidable effect and can be extremely useful with proper controlling. Generally, the acoustic induced fluid motion is a phenomenon of energy transfer between the mechanical vibration and fluid dynamics. In this chapter, we will introduce the brief history of the theory and application development for acoustic induced fluid motion, and review the research works that apply the acoustofluidic methods to the manipulation of object with different sizes/properties.

1.1 Acoustics induced fluid motion

1.1.1 Basics of acoustic waves

Acoustic wave as one of the classic wave formats, indicates a process of energy propagation (wikipedia, n.d.-a). It can propagate through different mediums, e.g., gas, liquid, and solid, by consistent compression and decompression. Specifically, it presents a way of particle vibration and movement. With different propagation mediums, the acoustic wave can express different motions. For example, transverse waves may be excited when propagating in solids, where particles move parallel to the wave

propagation direction, or longitudinal waves when propagating in the fluid (i.e., gas and liquid) displaces particles perpendicular to the direction of wave propagation.

The major parameters to characterize the acoustic waves are frequency, amplitude, phase, wave speed, and particle velocity. The classic wave equation can be derived through the relationship between these parameters in order to indicate the wave propagation motion. With certain assumptions that simply the physics scenarios, the linear wave equation can be deduced from three governing equations: Euler's equation (1.1), the continuity equation (1.2), and the state equation (1.3)(Hansen, 2001; Kinsler, Frey, Coppens, & Sanders, 1999).

$$\rho_0 \frac{\partial \boldsymbol{v}}{\partial t} = -\nabla p \tag{1.1}$$

$$\rho_0 \nabla \cdot \boldsymbol{v} = 0 \tag{1.2}$$

$$c = \sqrt{\frac{p}{\rho_0}} \tag{1.3}$$

Thus, the basic wave equation can be obtained as:

$$\nabla^2 p = \frac{1}{c^2} \frac{\partial^2 p}{\partial t^2} \tag{1.4}$$

And the acoustic theory starts from this equation and is greatly expanded to broader research.

On the other hand, as acoustic wave can provide consistent vibration, researchers found this time averaged effect can provide the force to different objects, e.g., small particles or liquids. One classic example is the acoustic standing wave can be utilized to

trap particles with different properties. With the current developed techniques, nowadays, acoustic waves have been broadly applied for particle manipulation and fluid actuation.

1.1.2 Acoustic streaming

Generally, when acoustic waves propagate in the liquid, acoustic streaming can be activated as the acoustic waves are attenuated and the energy is transferred to the fluid. More specifically, acoustic wave can generate a time-averaged momentum flux in the fluid and cause acoustic streaming(Sadhal, 2012; Wiklund, Green, & Ohlin, 2012). Different flow patterns can be induced by different acoustic excitations (e.g., frequency, amplitude) and geometry shapes. The acoustic streaming can be approximately categorized into three types: Eckart streaming, inner and outer boundary layer streaming, and microbubble/microstructure vibration induced streaming. Among the three types of streaming, the boundary layer streaming is induced by the acoustic energy viscously dissipated by the boundary layer between the liquid and solid (Lei, Hill, & Glynne-Jones, 2014; Wiklund et al., 2012). This type of streaming is usually seen in the microfluidic device where the thermal viscous effect cannot be neglected. The inner boundary streaming can then provide an external force term to the outer boundary layer fluid and initiate the streaming in a larger domain. The Eckart streaming is another type of streaming that is induced directly by the acoustic energy dissipation in the bulk fluid. Within the bulk fluid, there will be a circulating flow formed and aligned with the acoustic

wave propagation path. The microbubble/microstructure induced microstreaming is, as the term stated, induced by the vibration of the bubble or microstructure (e.g., sharp edge). As this small vibration can be driven by the acoustic wave, the generated microstreaming is usually localized around the vibration source. There are various studies towards different types of the acoustic streaming. With the understanding acoustic streaming motion, one research direction is trying to minimize the acoustic streaming especially when precious particle manipulation is needed. Another research direction is toward actively utilizing the streaming-induced drag force to complement the insufficient acoustic radiation force when dealing with small particles. Besides the particle manipulation, the fluid driving can also be useful for different applications, e.g., droplet manipulation, fluid pumping, and mixing.

1.1.3 Acoustic induced interface deformation

When the acoustic wave reaches the liquid-air interface, the large acoustic impedance mismatch will reflect the acoustic wave. At the same time, with relatively large incidence wave energy, the acoustic radiation pressure will act on the liquid-air interface and balance the surface tension. This will cause the liquid-air interface deformation. The first study on acoustic radiation pressure was by L. Rayleigh(Rayleigh, 1879, 1902), and further expanded to different research area. Elrod et al. discussed using focused acoustic beams to generate the droplet formation. They have investigated the droplet formation parameters (e.g., time and droplet size) with the relationship of the acoustic parameters

(e.g., frequency and pulse width)(Elrod et al., 1989) in detail. Meanwhile, C. Cinbis et al. further explored the influence of the surface tension effect during the deformation process, such as the maximum deformation height and the time to reach the height(Cinbis, Mansour, & Khuri-Yakoub, 1993). This study demonstrated the relationship between the surface tension, acoustic parameters, and deformation, which may be useful especially using the acoustic wave to identify the surface tension of a certain fluid. N. Bertin et al. studied the morphologies of the interface deformation induced by acoustic radiation pressure(Bertin, Chraïbi, Wunenburger, Delville, & Brasselet, 2012). They indicated that the shape of the interface deformation could be the result from the interaction between the wave propagation and the geometry of the fluid boundary. As these studies are leaning more towards the theoretical analysis of the phenomenon and revealing the physics problems. The interaction between the droplet and surface acoustic wave also attracts various researchers as more applications may be conducted inside or outside the droplet. Tan et al. demonstrates that capillary waves are formed on the surface of the droplet when high frequency acoustic waves are applied to it(M. K. Tan, Friend, Matar, & Yeo, 2010). Brunet et al. presented that the droplet may experience a creeping-jumping oscillation under the surface acoustic wave(Brunet, Baudoin, Matar, & Zoueshtiagh, 2010). Within their experiment, they found that the droplet interface deformation is resulted from the combined effect between acoustic radiation pressure and vortex streaming. These studies have built on the basis of the acoustic induced interface deformation and

could be expanded to different research topics and combined with the particle motion inside the droplet.

1.2 Acoustofluidic based object manipulation

1.2.1 Micro/Nanoscale particle manipulation

Acoustic waves are widely known as an effective tool to manipulate particles. Starting from researchers utilized the classic standing wave to trap single particle with different properties, various acoustic tweezers technologies have been developed over the years. As acoustic waves can propagate in different mediums, solid particles containing in the air and liquid can be manipulated with acoustic generated forces. While the classic standing wave serves as the basis of particle trapping, further development mainly focuses on the versatility of the manipulation in 2D or 3D spatial areas. For example, Marzo et al. demonstrated that by building the ultrasound emitter array, arbitrary acoustic fields can be accomplished and utilized for dynamic manipulation of the particle in air (Marzo et al., 2015). Three different methods of performing the trap are presented in their work, including the twin trap, the vortex trap, and the bottle trap. This generated trapping position can levitate and hold one single particle in the air, and by dynamically changing the position of the trap, particles can be moved along the designed path. This method significantly expands the capability and versatility of acoustic-based manipulation. Meanwhile, this dynamic single particle manipulation concept is also demonstrated in the liquid medium. Yang et al. demonstrated a self-navigated 3D acoustic

tweezers technique that can provide a stable trapping effect in the liquid(Y. Yang et al., 2021). With the real-time modulation of the acoustic fields, multiple functions can be realized with a 1.04 MHz, 256 elements transducer array. Meanwhile, as underwater acoustic waves have strong transmission capability, the acoustic waves can propagate through different solid materials with a change of phase and amplitude. While this wave distortion caused by solid material is usually seen as a side effect for precise manipulation, they applied the time-reversal principle to the system, so that the distortion can be minimized and the designed acoustic fields can be formed even with the obstacle on the propagation path. Meanwhile, Ghanem et al. also demonstrated the capability of using transducer arrays to achieve in-vivo particle manipulation(Ghanem et al., 2020). Benefitting from the high transmission ability of acoustic waves, they indicate that the stable trapping effect can be accomplished in the animal body. And with the similar wave modulation method, they are able to dynamically move the particle in the bladder of a pig. As the transducer array provides a great capability of dynamic manipulation, the current array technique still targets the particle with relatively large size (e.g., cm to mm) due to the relatively low frequency. And various small particles that possess high biomedical implications will need higher frequency and smaller devices in order to precisely manipulate them. Surface acoustic wave as an effective energy delivery method has been widely studied for particle manipulation(Ozcelik et al., 2018). Different frequencies and wave fields can be obtained simply by changing the geometry of the

interdigital transducers. With the combination of microfluidics, the SAW acoustic manipulation technique has been developed towards the direction of on-chip manipulation that can be applied to various biological, chemical, and material science applications. For example, Ding et al. demonstrate a SAW-based manipulation chip that can move single microparticles and cells in a contactless, label-free, and biocompatible manner (Ding et al., 2012). Guo et al. further developed the 3D surface acoustic wave tweezer platform that can manipulate the single particle in three-dimensional space in the liquid (Guo, Mao, Chen, Xie, Lata, Li, Ren, Liu, Yang, Dao, et al., 2016). Along with the single particle manipulation, they further demonstrate that they can control the cell-cell distance by modulating the acoustic signal (Guo et al., 2015). Besides the single particle spatial movement, acoustic separation also expresses great potential in the application of liquid biopsy, apheresis, and point-of-care devices. For example, Li et al. demonstrated a SAW based system that can separate the circulating tumor cells from white blood cells (P. Li et al., 2015). Since the particles with different dimensions will experience different acoustic radiation forces, by combining with laminar flow condition, particles with different sizes can be guided at different flow rates and collected from different outlets. Wu et al. demonstrate a platform that can directly separate the exosome from whole blood(Wu et al., 2017). With a two-unit system, blood cells can be removed in the first unit, and large microvesicles and apoptotic bodies can be further separated out in the second unit. This method indicates the acoustic wave can be applied to common biological

samples and achieve functional material/sample collection for diagnosis and therapy purposes. On the other hand, with the combination of acoustic waves and acoustic streaming, even smaller particles can be manipulated in the liquid. For example, Collins et al. utilize the high frequency acoustic wave and vortex streaming to guide the motion of nanoparticles(Collins, Ma, Han, & Ai, 2017). With the synergetic effect of fluid motion induced drag force and acoustic radiation force, nanoparticles can be concentrated or separated in a continuous flow. These methods represent a direction of studying and applying the acoustofluidic particle manipulation technique to various applications.

1.2.2 Droplet manipulation

Besides the solid particles, acoustic waves can also be applied to the droplet manipulation study. Some classic directions include droplet vibration, on-demand droplet generation, droplet ejection, nebulization, and dynamic droplet spatial manipulation. For example, Foresti et al. present an acoustic droplet levitation method, showing that with the transducer surrounded, the droplet can be levitated and rotated in the air (Foresti & Poulikakos, 2014). Meanwhile, with the consistent rotation, the droplet performs a deformation phenomenon and changes to the ellipsoid shape. Brunet et al. demonstrate that the surface acoustic wave can induce both acoustic streaming inside the droplet and liquid-air interface deformation with the synergetic effect of streaming and acoustic radiation pressure (Brunet et al., 2010). Mutafopulos et al. demonstrate a SAW-based platform that can generate the droplet containing single particles or cells

(Mutafopulos, Lu, Garry, Spink, & Weitz, 2020). With the traveling surface acoustic wave, the acoustic radiation pressure can generate force at the interface between oil and water medium and push the water droplet to the oil flow. In addition, the size of the droplet can be controlled by the acoustic wave amplitude and duration. Chen et al. report a digital acoustofluidic device that can directly eject the water droplet in an on-demand and oil-free manner(K. Chen et al., 2018). With an interdigital transducer with a circular configuration, the acoustic energy can be focused on a small area near the liquid-air interface and generate a strong force to push the droplet to the air. This method indicates a simple way of droplet ejection and generation with a controllable volume. Rajapaksa et al. demonstrate an integrated surface acoustic wave based nebulizer system that can generate the mist containing shear sensitive biomolecules(Rajapaksa, Qi, Yeo, Coppel, & Friend, 2014). This method indicates a significantly effective way for drug delivery and vaccination therapy. Furthermore, Zhang et al. developed a digital acoustofluidic platform that utilizes the interdigital transducer array to achieve the dynamic, rewritable, fluid droplet spatial transport(S. P. Zhang et al., 2018). They utilized the acoustic streaming effect generated in oil to drive the motion of the water droplet on top of the oil layer. This method represented a novel method for non-contact and label-free digital fluid processing.

1.2.3 Small organism manipulation

Model organism studies can provide numerous insights for drug screening, disease modeling, and genetic/cellular mechanism exploration. Acoustofluidic techniques as a noncontact manipulation method can provide the desired alignment for small organisms, which can be combined with microscopy or bioassay techniques. Specifically, acoustofluidic manipulation can provide the acoustic radiation force and induce acoustic streaming effect for organism imaging and sorting. For example, Ahmed et al. demonstrate an acoustic-based, on chip control technique for single cell and organism manipulation (Ahmed, Ozcelik, Bojanala, Nama, Upadhyay, Chen, Hanna-Rose, et al., 2016). They designed a microfluidic channel with the cavity on the channel sidewall. With the fluid flowing through, the cavity can form/trap the microbubble in it and form the liquid-air-solid structure. With the acoustic excitation, the microbubble can generate the vibration and further induce the vortex streaming nearby. Multiple microbubbles induced vortex streaming can collectively generate the rotational motion of the C. elegans. Thus, with the rotational manipulation of the C. elegans, Multiview imaging can be obtained with the microscope. Furthermore, Ozcelik et al. demonstrate that by utilizing the sharp edge solid structure, similar acoustic streaming can also be initiated and utilized for C. elegans rotation(Ozcelik et al., 2016). On the other hand, Zhang et al. develop a SAW-based device that can be utilized for C. elegans rotation(J. Zhang et al., 2019). With the specific excitation manner of two interdigital transducers, the C. elegans can be rotated

along with different directions (i.e., clockwise, or anti-clockwise) or be fixed in the middle of the channel. By tuning the acoustic amplitude, the rotation speed can be modified as desired. Moreover, they utilized the pulse signal to achieve the jogging mode of the rotation which can obtain the 2D image for certain angles of the organism. And they further demonstrate that by combining with the fluorescent detection unit and flow systems, they can achieve C. elegans sorting with the specific labeled fluorescent signal using surface acoustic waves(J. Zhang et al., 2020). Besides the small organism rotational manipulation, Yang et al. demonstrate an acoustic confinement method that can levitate and align the zebrafish larvae in the air(Z. Yang et al., 2019). They also demonstrate the potential of combing the acoustic setup with advanced microscopy technique (i.e., light-sheet microscope) so that high-resolution images can be obtained for in-vivo phenotyping.

1.3 Dissertation outline

This dissertation describes our research effort on exploring the underlying mechanism of acoustic induced fluid motion and designing new devices that can be utilized for different small object manipulation (e.g. particle, droplet, and small organism). Chapter 2-6 are expanded version of published, submitted, or prepared research manuscript. A short motivation and a brief state-of-the-art work introduction are discussed at the beginning of each chapter to introduce the innovation and features of our study.

Chapter 2 presents the theoretical and numerical analysis of the acoustofluidics based technique, including the surface acoustic wave generation and propagation, fluid motion driven by acoustic waves, and corresponding particle force analysis. We have revisited the basic formulas and introduced the general principle when simulating and characterizing the acoustofluidic phenomenon.

Chapter 3 introduces more specific fluid motion actuated by acoustic waves, that is the vortex acoustic streaming. Different scenarios involving acoustic generated vortex streaming are discussed, including standing surface acoustic wave induced small vortices, travelling surface acoustic induced vortex in a relatively large domain, and the vortex streaming in a spinning droplet. Detailed theoretical and numerical simulation are discussed.

Chapter 4 demonstrates a novel acoustofluidic device we have developed that utilizes the "polarized streaming" for large object manipulation in a relatively broad fluid domain. Device design, fabrication, and mechanism are introduced. Then particle tracing and zebrafish rotational manipulation are demonstrated in order to validate the performance.

Chapter 5 introduces an acoustofluidic rotational tweezing system building based on the device we described in the previous chapter. 3D multispectral imaging and 3D reconstruction functions are developed and integrated with the device to form the ART

system. This enables the contactless rotational manipulation and highly efficient 3D imaging of different objects, e.g., zebrafish larvae, yolk, and inside organs.

Chapter 6 describes the substantial effort building the flow system and characterization standard in order to obtain the quantitative analysis of the zebrafish morphological features (e.g., zebrafish body abnormal ratio, and organ volume/surface area) and provide statistical analysis for different groups of samples.

Chapter 7 summarizes this dissertation and presents perspectives for future study.

2. Theoretical Aspects of Acoustofluidics

Acoustofluidics devices have been applied increasingly in biological sample handling (e.g., bio-particle manipulation and liquid handling). Understanding the theoretical aspects of acoustofluidics is significant for revealing the underlying working principle of the devices and developing novel devices with advanced functions.

In this Chapter, we summarized the theoretical models of common physical processes in acoustofluidic devices. Sections 2.1 introduces the theory of the generation and propagation of surface acoustic waves (SAWs) in the piezoelectric substrate. Section 2.2 presents the theory of non-linear acoustic dynamics in the fluids, which includes acoustic wave propagation and acoustic streaming. Section 2.3 describes the mechanism of particle manipulation using acoustofluidic devices.

2.1 Motivation

This section introduces the background and theory of generating surface acoustic waves (SAWs) in acoustofluidic devices and the phenomenon generated by the SAWs propagation.

Surface acoustic waves are the non-dispersive electro-mechanical waves generated near the surface of the elastic solid medium. During the waves' propagation, their displacement exponentially decays in depth direction away from the substrate surface so that the acoustic energy (usually >95%) is confined in a layer with a depth equal to one wavelength near the surface of the substrate (Morgan, 1973). Since the 1940's, the

SAWs devices have been applied in electronic and communication systems to achieve multiple functions, including signal filter and signal processing (Atanasoff & Hart, 1941; Datta, 1986). With the emergence of the interdigital transducers (IDTs), SAWs with a broad range of wavelengths were artificially engineered in the piezoelectric substrate to achieved versatile capabilities. The IDTs contain a series of interleaved metal electrodes deposited on the surface of the piezoelectric substrate as shown in Figure 2.1. The width of the electrodes equals to the width of the gaps in between. Through the piezoelectric effect, when applying alternating electric voltage to the electrodes, the electric field penetrates the piezoelectric substrate and SAWs with a wavelength of λ can be activated. The wavelength λ equals to four times of the width of electrode.

Microfluidics, which first emerged during the 1970's, studies the fluid motion in channels with dimensions in micrometer scale (H. Li, Friend, & Yeo, 2007; Terry, Jerman, & Angell, 1979). With the rise of the microfluidics, lab-on-a-chip systems combining the SAWs and microfluidics have been developed for application, including chemical sensing (Barnkob, Augustsson, Laurell, & Bruus, 2012; Fu et al., 2017), particle manipulation (Collins, Khoo, et al., 2017; Guo, Mao, Chen, Xie, Lata, Li, Ren, Liu, Yang, & Dao, 2016; Mao et al., 2017), and liquid processing (M. Alghane, Chen, et al., 2012; S. P. Zhang et al., 2018). These systems, as a portion of acoustofluidic devices, presents essential characteristics, including compact dimensions, bio-compatibility, label-free, and inexpensive.

The SAW-based acoustofluidic devices are an acoustic-driven microfluidic system that use SAWs to activate fluidic or particle motions. As reported by (Viktorov, 1967), SAWs (also known as Rayleigh waves) contain transversal wave components and longitudinal wave components with a lag in phase (Figure 2.2). Thus, the particles at the substrate surface oscillate in an anticlockwise eclipse path as the SAWs propagate rightwards. When the SAWs meet liquid loading on the substrate, the SAWs will obliquely leak into the liquid and generate acoustic fields inside the liquid medium (Figure 2.1). In the SAW-based acoustofluidic devices, the handling of liquid/particle can be performed by utilizing the force induced by acoustic fields.

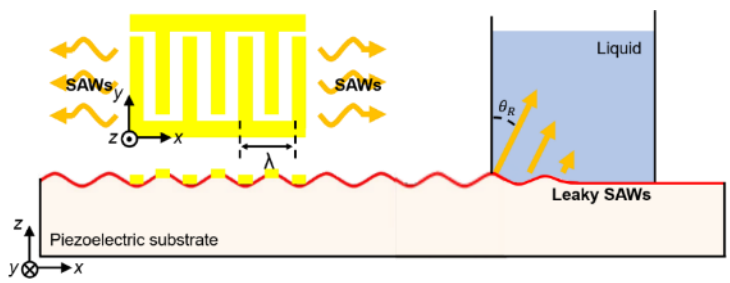

Figure 2.1: Illustration of SAWs propagation in piezoelectric substrate and the leaky SAWs in the liquid. $\boldsymbol{\lambda}$: wavelength of the SAWs. $\boldsymbol{\theta_R}$: Rayleigh angle.

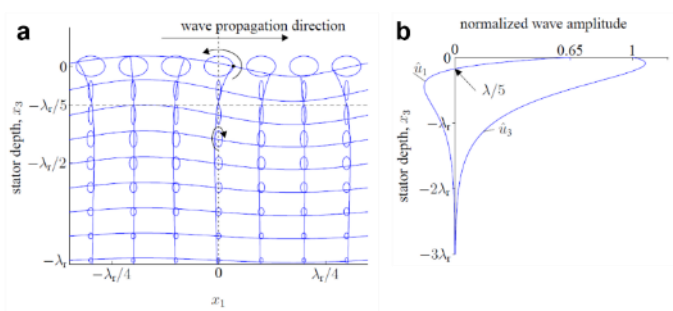

Figure 2.2: Rayleigh SAWs propagation in the elastic solid. a, Displacement field distribution in the substrate. b, The displacement amplitude decays away from the surface of the substrate (Feenstra, 1978).

2.1 SAWs in piezoelectric substrate

The 128° Y-X cut lithium niobate ($LiNbO_3$) is a piezoelectric material which has been wildly used as the substrate for SAW-based acoustofluidic devices for the generation of SAWs by applying alternating current signals to the IDTs. In this substrate, an applied alternating current signal to the IDTs can generate the strain and surface acoustic waves.

The mechanical vibration of the piezoelectric solid is governed by the momentum equations. The charge conservation equation governs the electrical behavior in the piezoelectric materials. In the piezoelectric material, the stress, strain, electrical displacement field, and the electric field are coupled as expressed by the constructive equations (Kannan, 2006):

$$T_{ij} = C_{ijkl}^{E} \cdot S_{kl} - e_{ijk}^{T} \cdot E_k, \tag{2.1}$$

$$D_j = e_{jkl} \cdot S_{kl} + \epsilon_{jk}^{S} \cdot E_k, \tag{2.2}$$

These equations are stated in the stress-charge form. In the equations, T_{ij} is the stress vector, S_{kl} is the strain vector, D_j is the electrical displacement, E_k is the strength of the electric field, C_{ijkl}^{E} is the elasticity matrix ($\mathrm{N/m^2}$), e_{jkl} is the piezoelectric matrix ($\mathrm{C/m^2}$), and ϵ_{ij} is the permittivity matrix (F/m).

The electrical field strength E_k can be estimated by calculating the gradient of the electrical potential φ: $E_k = \frac{\partial \varphi}{\partial x_k}$. The governing equation of the displacement in the piezoelectric material can be acquired as follows (M. M. Alghane, 2013):

$$\rho \frac{\partial^2 u_i}{\partial t^2} - C_{ijkl}^E \frac{\partial^2 u_l}{\partial x_j \partial x_k} - e_{jkl}^T \frac{\partial^2 \varphi}{\partial x_j \partial x_k} = 0 \tag{2.3}$$

$$e_{jkl} \frac{\partial^2 u_l}{\partial x_j \partial x_k} - \epsilon_{jk}^S \frac{\partial^2 \varphi}{\partial x_j \partial x_k} = 0 \tag{2.4}$$

In acoustofluidics, the SAWs obliquely leak into the liquid medium situated on the substrate and manipulation of the flow motion and particles within the liquid. The vibratory velocity of the surface of the substrate induced by 2D standing Rayleigh SAW can be modeled by the classic analytical expression (Guo, Mao, Chen, Xie, Lata, Li, Ren, Liu, Yang, Dao, et al., 2016):

$$v_x = \chi A_m \omega \left\{ e^{i(\omega t - kx) - \alpha x} + e^{i[\omega t - k(W-x)] - \alpha(W-x)} \right\} \tag{2.5}$$

$$v_z = -i A_m \omega \left\{ e^{i(\omega t - kx) - \alpha x} - e^{i[\omega t - k(W-x)] - \alpha(W-x)} \right\} \tag{2.6}$$

where χ is the ratio between the amplitude of longitudinal vibration component and transverse vibration component of Rayleigh SAW, A_m indicates the displacement amplitude of the transverse vibration component, and α indicates the attenuation coefficient of the amplitude of vibratory displacement along the route of the wave propagation.

2.2 Non-linear acoustic dynamics in the fluids

2.2.1 Perturbation theory

In acoustofluidics, the non-linear acoustic dynamics is the fundamental principal for the applications. The dynamics in viscous compressible fluid is governed by the

continuity equation (mass conservation) and the compressible Navier-Stokes equation (momentum conservation) (C. Chen et al., 2018):

$$\frac{\partial \rho}{\partial t} + \nabla \cdot (\rho \boldsymbol{v}) = 0, \tag{2.7}$$

$$\rho \frac{\partial \boldsymbol{v}}{\partial t} + \rho(\boldsymbol{v} \cdot \nabla)\boldsymbol{v} = -\nabla p + \mu \nabla^2 \boldsymbol{v} + \left(\frac{1}{3}\mu + \mu_B\right)\nabla(\nabla \cdot \boldsymbol{v}), \tag{2.8}$$

where $\rho, \mu,$ and μ_B are the mass density, dynamic shear viscosity, and dynamic bulk viscosity of fluid, respectively; p and $\boldsymbol{v}$ are velocity and pressure in the fluid, respectively. By assuming a linear relation between pressure and density, the constitutive relation between the pressure p and fluid density ρ can be expressed as (Nama et al., 2015):

$$p = c_0^2 \rho, \tag{2.9}$$

where c_0 is the speed of sound in the fluid medium. The non-linear acoustic dynamics in the liquid include the acoustic waves propagation and the resulting acoustic streaming. The acoustic streaming is a steady streaming commonly observed in the acoustofluidic devices. Therefore, the fluid motion generated during the acoustic process compose of two components: (1) a component in fast time-scale whose period equals to the period of the substrate vibration generated with acoustic wave propagation, and (2) a component in slow time-scale. The slow time scale component is generated because of the viscous dissipation. This component is known as the acoustic streaming, which can be considered to be steady comparing with the fast time scale component (Nama et al., 2015). Nyborg's perturbation assumption was applied to expand the fluid velocity, pressure, and density to the sum of component with different time-scales:

$$\boldsymbol{v} = \boldsymbol{v_0} + \boldsymbol{v_1} + \boldsymbol{v_2} + O(\varepsilon^3) + \cdots, \tag{2.10a}$$

$$p = p_0 + p_1 + p_2 + O(\varepsilon^3) + \cdots, \tag{2.10b}$$

$$\rho = \rho_0 + \rho_1 + \rho_2 + O(\varepsilon^3) + \cdots, \tag{2.10c}$$

Among Eqns. (2.10), the subscript *j* refer to the jth order component of the variables, i.e., ~ O(ε^j), where ε is a small dimensionless parameter. With the small dimensionless parameter, Eqs. (2.10) can also be written as:

$$\boldsymbol{v} = \boldsymbol{v_0} + \varepsilon\tilde{\boldsymbol{v}}_{\boldsymbol{1}} + \varepsilon^2\tilde{\boldsymbol{v}}_{\boldsymbol{2}} + O(\varepsilon^3) + \cdots, \tag{2.11a}$$

$$p = p_0 + \varepsilon\tilde{p}_1 + \varepsilon^2\tilde{p}_2 + O(\varepsilon^3) + \cdots, \tag{2.11b}$$

$$\rho = \rho_0 + \varepsilon\tilde{\rho}_1 + \varepsilon^2\tilde{\rho}_2 + O(\varepsilon^3) + \cdots, \tag{2.11c}$$

By substituting Eqns. (2.11) into the governing equations and collecting the zeroth-order terms O(ε^0), the 0th-order equations that govern the background flow velocity, which is not relative to acoustic dynamics, can be obtained as:

$$\rho_0\nabla\cdot(\boldsymbol{v_0}) = 0, \tag{2.12}$$

$$\rho_0\frac{\partial\boldsymbol{v_0}}{\partial t} + \rho_0(\boldsymbol{v_0}\cdot\nabla)\boldsymbol{v_0} = -\nabla p_0 + \mu\nabla^2\boldsymbol{v_0} + \left(\frac{1}{3}\mu + \mu_B\right)\nabla(\nabla\cdot\boldsymbol{v_0}), \tag{2.13}$$

in which ρ_0 is the density of the fluid, μ is the dynamic viscosity of the fluid, μ_B is the bulk viscosity of the fluid, and $\boldsymbol{v_0}$ is the background flow velocity.

By collecting the first-order terms O(ε^1), the 1st-order equations that govern the acoustic field can be obtained as:

$$\frac{\partial\rho_1}{\partial t} + \rho_0\nabla\cdot(\boldsymbol{v_1}) = 0, \tag{2.14}$$

$$\rho_0\frac{\partial\boldsymbol{v_1}}{\partial t} = -c_0^2\nabla\rho_1 + \mu\nabla^2\boldsymbol{v_1} + \left(\frac{1}{3}\mu + \mu_B\right)\nabla(\nabla\cdot\boldsymbol{v_1}), \tag{2.15}$$

For harmonic acoustic field ($p(\boldsymbol{r},t) = (p(\boldsymbol{r})e^{i\omega t}$), the 1st-order equations can be written as:

$$i\omega\rho_1 + \rho_0\nabla\cdot(\boldsymbol{v_1}) = 0, \tag{2.16}$$

$$\rho_0 i\omega\boldsymbol{v_1} = -c_0^2\nabla\rho_1 + \mu\nabla^2\boldsymbol{v_1} + \left(\frac{1}{3}\mu + \mu_B\right)\nabla(\nabla\cdot\boldsymbol{v_1}), \tag{2.17}$$

where i is the imaginary unit, i^2= -1. Similarly, By obtaining only the second-order terms O(ε^2), the 2nd-order equations can be acquired as:

$$\frac{\partial\rho_2}{\partial t} + \rho_0\nabla\cdot(\boldsymbol{v_2}) + \nabla\cdot(\rho_1\boldsymbol{v_1}) = 0, \tag{2.18}$$

$$\rho_0\frac{\partial\boldsymbol{v_2}}{\partial t} + \rho_0\frac{\partial\boldsymbol{v_1}}{\partial t} + \rho_0(\boldsymbol{v_1}\cdot\nabla)\boldsymbol{v_1} = -\nabla p_2 + \mu\nabla^2\boldsymbol{v_2} + \left(\frac{1}{3}\mu + \mu_B\right)\nabla(\nabla\cdot\boldsymbol{v_2}), \tag{2.19}$$

As the acoustic streaming is a steady fluid motion, by performing time average each term in these equations, the governing equations of acoustic streaming can be derived as:

$$\rho_0\nabla\cdot\langle\boldsymbol{v_2}\rangle = -\nabla\cdot\langle\rho_1\boldsymbol{v_1}\rangle, \tag{2.20}$$

$$-\nabla\langle p_2\rangle + \mu\nabla^2\langle\boldsymbol{v_2}\rangle + \left(\frac{1}{3}\mu + \mu_B\right)\nabla(\nabla\cdot\langle\boldsymbol{v_2}\rangle) = \rho_0\langle j\omega\boldsymbol{v_1}\rangle + \rho_0\langle(\boldsymbol{v_1}\cdot\nabla)\boldsymbol{v_1}\rangle, \tag{2.21}$$

where $\langle X(\boldsymbol{r},t)\rangle$ indicates that the term was integrated and averaged in a time equals to the period of acoustic waves. The mass source term ($-\nabla\cdot\langle\rho_1\boldsymbol{v_1}\rangle$) and the force sources terms ($\rho_0\langle j\omega\boldsymbol{v_1}\rangle + \rho_0\langle(\boldsymbol{v_1}\cdot\nabla)\boldsymbol{v_1}\rangle$) on the right sides of Eqs. (2.20) and (2.21) reify the resulting effect of the 1st-order on the 2nd-order problem.

Thus, the fluid dynamics including the background flow, propagation of acoustic waves, and acoustic streaming can be explored by solving Eqns. (2.12), (2.13), (2.16), (2.17), (2.20) and (2.21).

2.2.2 Reynolds' stress

The governing equation of acoustic streaming are the continuity equation and the Navier-Stokes equation:

$$\rho_0 \nabla \cdot \boldsymbol{v}_{dc} = 0 \tag{2.22}$$

$$\rho_0 (\boldsymbol{v}_{dc} \cdot \nabla) \boldsymbol{v}_{dc} = -\nabla p_{dc} + \mu \nabla^2 \boldsymbol{v}_{dc} + \left(\mu_B + \frac{1}{3}\mu\right) \nabla(\nabla \cdot \boldsymbol{v}_{dc}) + \boldsymbol{F} \tag{2.23}$$

where ρ_0 is the fluid density, μ_B and μ are the bulk viscosity and shear viscosity, $\boldsymbol{v_{dc}}$ is the steady streaming velocity, and $\boldsymbol{F}$ is the external body force. In this case, $\boldsymbol{F}$ in Eqn. (2) is the acoustic process induced body force that generate acoustic streaming which can be express as the spatial gradient of Reynolds' stress (M. Alghane, Chen, et al., 2012; Lighthill, 1978):

$$F_j = -\rho_0 \sum_{i=1}^{3} \frac{\partial \overline{v_i v_j}}{\partial x_i} \tag{2.24}$$

in which $\boldsymbol{v}$ is the leaky SAW velocity, and the subscripts i, j, k represent the components of the variable. The Eqn. (2.24) can be expanded as:

$$F_x = -\rho_0 \left(\frac{\partial \overline{u_1 u_1}}{\partial x} + \frac{\partial \overline{v_1 u_1}}{\partial y} + \frac{\partial \overline{w_1 u_1}}{\partial z} \right) \tag{2.25a}$$

$$F_y = -\rho_0 \left(\frac{\partial \overline{u_1 v_1}}{\partial x} + \frac{\partial \overline{v_1 v_1}}{\partial y} + \frac{\partial \overline{w_1 v_1}}{\partial z} \right) \tag{2.25b}$$

$$F_z = -\rho_0 \left(\frac{\partial \overline{u_1 w_1}}{\partial x} + \frac{\partial \overline{v_1 w_1}}{\partial y} + \frac{\partial \overline{w_1 w_1}}{\partial z} \right) \tag{2.25c}$$

Since the harmonic leaky SAW displacement $\boldsymbol{u}$ can be approximately expressed by1

$$u_1 = 0 \tag{2.26b}$$

$$v_1 = A_m e^{i\omega t} e^{-ik_L y} e^{-\alpha k_L z} \tag{2.26b}$$

$$w_1 = -i\alpha A_m e^{i\omega t} e^{-ik_L y} e^{-\alpha k_L z} \tag{2.26b}$$

By taking $v_i = i\omega u_i$ and taking Eqn. (4a)-(4c) into Eqn. (3), the leaky SAW-induced body force cab be expressed as1

$$F_x = 0 \tag{2.27b}$$

$$F_y = -(1 + \alpha_1^2) A_m^2 \omega^2 k_i e^{[2(k_i y + \alpha_1 k_i z)]} \tag{2.27b}$$

$$F_z = -(1 + \alpha_1^2) A_m^2 \omega^2 k_i \alpha_1 e^{[2(k_i y + \alpha_1 k_i z)]} \tag{2.27b}$$

where $\alpha = i\alpha_1$.

2.3 Particle motion

2.3.1 Acoustic radiation force (ARF)

For a spherical particle suspended in the fluid, it experiences an acoustic radiation force which is induced by acoustic scattering on the particle. The acoustic radiation force is one of the two essential forces that drive particle movement in the acoustofluidic devices. This section introduces the theoretical model of the acoustic radiation force for a spherical particle.

The theoretical expression for the acoustic radiation force on an incompressible particle suspended in the inviscid fluid was derived by (King, 1934). The acoustic radiation force for a compressible particle was derived by (Yosioka & Kawasima, 1955). Based on these works, the acoustic radiation force for a small spherical particle (diameter smaller than a wavelength of the acoustic wave) can be expressed as (Gor'kov, n.d.):

$$\boldsymbol{F_{rad}} = -\nabla\left\{V_p\left[\frac{f_1}{2\rho_0 c^2}\langle p_1^2\rangle - \frac{3\rho_0 f_2}{4}\langle \boldsymbol{v_1}\cdot\boldsymbol{v_1}\rangle\right]\right\} \tag{2.28a}$$

in which

$$f_1 = 1 - \frac{\rho_0 c^2}{\rho_p c_p^2} \tag{2.28b}$$

$$f_2 = \frac{2(\rho_p - \rho_0)}{2\rho_p + \rho_0} \tag{2.28c}$$

where ρ_o and c are the density and speed of sound of the fluid, V_p, ρ_p, and c_p are the volume, density, and speed of sound of the particle, respectively. Here the p_1 and $\boldsymbol{v_1}$ are the acoustic pressure and acoustic particle velocity. This theoretical expression calculates acoustic radiation force for particles suspended in fluid with arbitrary acoustic field distributions.

By taking the expression of 1D standing acoustic wave ($p = P_a cos(\omega t) cos(kx)$) into the above expression, the acoustic radiation force generated by 1D standing acoustic wave can be reduced to

$$F_{rad} = V_p E_a k \Phi sin(2kx) \tag{2.29a}$$

where

$$\Phi = \frac{5\rho_p - 2\rho}{2\rho_p + \rho} - \frac{c^2\rho}{c_p^2\rho_p} \tag{2.29b}$$

where E_a is the acoustic energy density, k is the wave number, and Φ is the acoustic contrast factor relative to the density and compressibility of the medium and the particle. The positive value of the acoustic contrast factor determines that the particle will be

moved to pressure nodes whereas the negative value of Φ indicates that the particle will be moved to the antinodes of the standing acoustic wave.

2.3.2 Drag force

In acoustofluidic devices, viscous drag force is another essential force that drives the movement of the particles suspended in the fluid medium. The viscous drag force acting on a particle sufficiently far from the walls can be formulated by the Stokes drag force (Guo, Mao, Chen, Xie, Lata, Li, Ren, Liu, Yang, Dao, et al., 2016):

$$\boldsymbol{F_d} = 6\pi R\mu\left(\boldsymbol{v_f} - \boldsymbol{v_p}\right) \tag{2.30}$$

where $\boldsymbol{v_p}$ is the velocity of the particle and $\boldsymbol{v_f}$ is the velocity of the fluid. The particle motion driven by the acoustic radiation force and the viscous drag force can be described by:

$$m\frac{d\boldsymbol{v_p}}{dt} = \boldsymbol{F_{rad}} + \boldsymbol{F_d} \tag{2.31}$$

where m is the mass of the particle.

2.4 Summary

In this chapter, we introduced the basic governing equations of the acoustofluidic phenomenon, including the SAWs generation and propagation in the piezoelectric substrate, non-linear acoustic dynamics and the generation of acoustic streaming, and particle movement driven by acoustic radiation force and viscous drag force. On the basis of these theoretical frameworks, theoretical analysis and numerical modeling are

performed in the following chapters to explore the working mechanism of acoustofluidic device with different setups.

3. Vortex-streaming Acoustofluidics

In this chapter, we explored the generation and application of vortex streaming with multiple patterns and dimensions using acoustofluidic devices. Sections 3.1 introduces the streaming pattern in the classic standing SAW device and the slip velocity method to simplify and reduce the calculation amount in the numerical simulation of acoustic streaming. Section 3.2 presents the vortex streaming pattern generated by IDTs merged in the oil and the application of this streaming pattern for droplet manipulation. The work presented in this subsection has been published on *Lab on a Chip* (C. Chen et al., 2018). Section 3.3 describes the vortex streaming pattern and particle concentration mechanism in the spinning droplet. Most of the work presented in this subsection has been published on *Science Advances* (Gu et al., 2021). Lastly, we summarized the generation and capabilities of the vortex streaming pattern we discussed in this chapter.

3.1 Acoustic streaming by standing SAWs

The typical configuration of generating standing SAW (SSAW) in microfluidic devices is bonding a microchannel or microchamber between a pair of interdigital transducers (Figure 3.1). When AC signals are applied to the IDTs, two SAWs with the same frequency and uniform amplitude are activated and propagate like two plane waves in opposite directions. The SSAW fields in the microfluidic channel/chambers with static fluid has been broadly applied in on-chip cell culture, cell patterning, and cell-cell interaction studies. The acoustic streaming generated within the SSAW devices are also

applied to manipulate objects in these studies (Guo, Mao, Chen, Xie, Lata, Li, Ren, Liu, Yang, Dao, et al., 2016). In these sections, we explored the acoustic streaming pattern generated by SSAW and introduced a numerical simulation method called "slip velocity method" that can reduce calculation amount for the simulation of acoustic streaming in large fluid domain.

3.1.1 2D Numerical model

Due to the uniformity of the SSAW along the long longitudinal direction of the channel, the numerical model of the classic SSAW can be reduce to a 2D modeling on the lateral cross-section of the device. Figure 3.1 shows the cross-section of the typical SSAW device configuration, in which the fluid is confined in a PDMS channel bonded on the substrate between a pair of IDTs. The rectangular fluid domain which has a width of W and a height of H, was selected to be the computational domain for the numerical modeling.

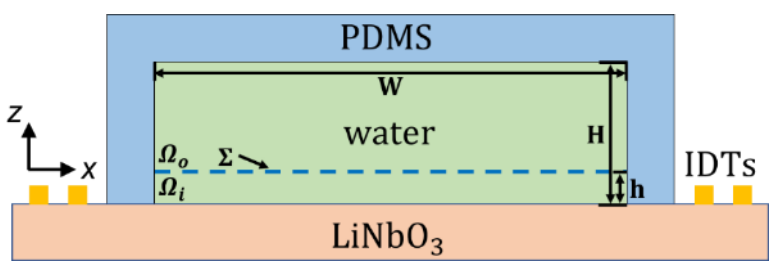

Figure 3.1: The schematic showing the classic SAW device at a cross-section view. $\boldsymbol{\Omega_i}$ and $\boldsymbol{\Omega_o}$ indicate the area of inner acoustic streaming (Stokes boundary layer) and the area of the outer acoustic steaming, respectively. The boundary of the two area (**Σ**) is marked by a blue-dashed line.

In this study, the frequency of the SAW is set to be 13 MHz (corresponding to a wavelength of λ=300 μm). As the distribution of the SSAW and the resulting acoustic streaming pattern is periodic, we set the channel width (W) to 300 μm and height (H) to 100 μm to study the typical physics within one wavelength. The governing equations are Eqs. (2.16), (2.17), (2.20), and (2.21) as stated in Section 2.2.1. The parameters used in this study are listed in Table 3.1.

Table 3.1: Value of the variables applied in the simulation (at 298K)(Nama et al., 2015)**.**

Density of water	ρ_0	997 kg/m^3
Speed of sound in water	c_0	1495 m/s
Dynamic viscosity of water	μ	8.9×10^{-4} Pa·s
Kinematic viscosity of water	ν	8.93×10^{-7} m^2/s
Speed of sound in $LiNbO_3$	c_s	3900 m/s
Density of PDMS	ρ_P	970 kg/m^3
Speed of sound in PDMS	c_P	1080 m/s
Driving frequency	f	13 MHz
Wavelength of SAW	λ	300 μm
Displacement amplitude	A_m	0.748 nm
Amplitude ratio between the longitudinal and transverse vibrations of Rayleigh SAW	χ	0.7428
Displacement decay coefficient	α	176 m^{-1}

Solving the acoustic streaming patterns in a fluid field contains two steps (Guo et al., 2015; Guo, Mao, Chen, Xie, Lata, Li, Ren, Liu, Yang, Dao, et al., 2016). First, the first-order equations (Eqs. (2.16) and (2.17)) are solved to determine the 1st-order SSAW field in the fluid domain. Based on the first-order solution of p_1 and $\boldsymbol{v_1}$, the mass source term

($m_s = -\nabla \cdot \langle \rho_1 \boldsymbol{v_1} \rangle$) and the force sources terms ($\boldsymbol{F_s} = \rho_0 \langle j\omega \boldsymbol{v_1} \rangle + \rho_0 \langle (\boldsymbol{v_1} \cdot \nabla) \boldsymbol{v_1} \rangle$) on the right side of Eqs. (2.20) and (2.21) can be determined. These terms show the effect of the first-order acoustic field on the second-order acoustic streaming pattern. Second, the 2nd-order acoustic streaming problem is solved in the fluid domain based on the first-order solution from the first step. This model follows the methods in the work of (Guo, Mao, Chen, Xie, Lata, Li, Ren, Liu, Yang, Dao, et al., 2016). The above-stated problem is solved via the finite element software package COMSOL Multiphysics 5.2a. A "Thermoviscous Acoustics" physics package is used to solve Eqs. (2.16) and (2.17) in the first step. The vibration velocity of the piezoelectric substrate of the 2D standing Rayleigh SAW pattern (Eqs. (2.5) and (2.6)) is applied as the boundary condition at the bottom of the water domain. A "normal impedance" boundary condition with the impedance of the PDMS is applied to the two sides and top of the fluid domain. A "Frequency Domain" solver is applied to solve this boundary value problem at the driving frequency 13 MHz. Next, a "Laminar Flow" physics package is applied to solve the 2nd-order equations (Eqs. (2.20) and (2.21)) based on the 1st-order solution in the whole fluid domain from the previous step. The mass source term ($m_s = -\nabla \cdot \langle \rho_1 \boldsymbol{v_1} \rangle$) and force source terms ($\boldsymbol{F_s} = \rho_0 \langle \frac{\partial \boldsymbol{v_1}}{\partial t} \rangle + \rho_0 \langle (\boldsymbol{v_1} \cdot \nabla) \boldsymbol{v_1} \rangle$) are added in the entire fluid domain using the "weak contribution" and "volume force" conditions. The boundary condition of "No Slip Wall" is applied to all the boundaries. The second-order problem was solved using a "Stationary" solver.

The solution of absolute acoustic pressure p_1 (1st-order pressure) and acoustic streaming velocity $\langle \boldsymbol{v_2} \rangle$ (averaged second-order velocity) are shown in Figure 3.2a-c. As shown in Figure 3.2a, two pressure antinodes are generated by the leaky SSAW in the channel with a width equal to one wavelength. Figure 3.2b shows that four vortex streaming are generated in the acoustic fields with two pressure antinodes, and the speed of streaming is relatively high near the bottom and decreases as the height increases. Figure 3.2c, which zooms in the acoustic streaming $\langle \boldsymbol{v_2} \rangle$ distribution in a layer at the bottom with a thickness of $4\delta_v$ (0.588 μm in this case). In this thin layer, the streamlines are almost horizontally distributed lines, which indicates no vortex tendency. The streaming velocity gradually increases from zero (at the bottom) away from the channel bottom.

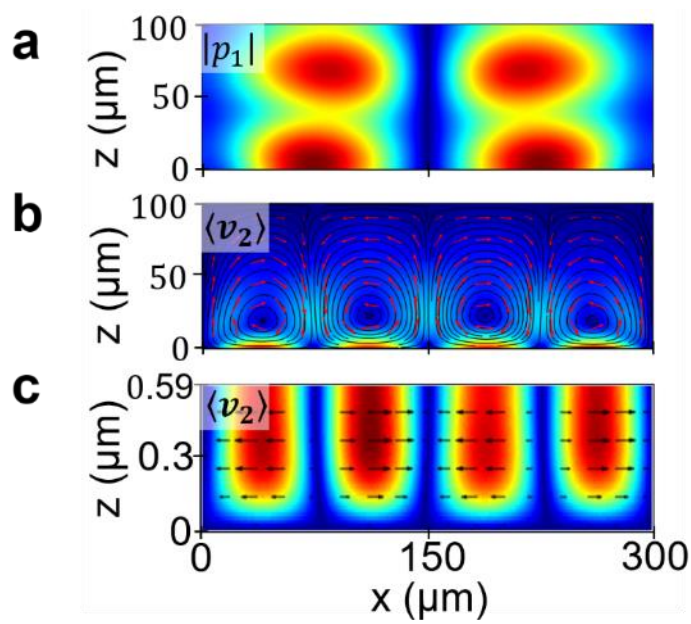

Figure 3.2: Simulation results of the acoustic field and acoustic streaming in the classic SAW device. The problem was solved using the traditional approach. a, Color plot

showing the amplitude of the 1st-order pressure $\boldsymbol{p_1}$ in the fluid domain ($\boldsymbol{\Omega_i} \cup \boldsymbol{\Omega_o}$). The color map indicates zero value in blue and highest value of 0.28 MPa in red. Two pressure anti-nodes are generated within the one-wavelength-wide fluid domain. b, Acoustic streaming velocity $\langle \boldsymbol{v_2} \rangle$ in the whole fluid domain (value: minimum: zero (blue), maximum: of 4.32×10^{-4} m/s (red)). The streaming pattern are shown by the streamlines with arrows. Four vortices are generated by acoustic field with two anti-nodes. c, Zoomed-in figure of the streaming in the inner boundary layer (thickness: $4\,\boldsymbol{\delta_\nu} = \mathbf{0.588}$ μ**m** for 13MHz SAW in the water medium). The streaming velocity in the boundary is mainly in the horizontal direction. The streaming speed has a minimum value at the bottom and a maximum value at the top of the boundary layer.

To further evaluate the variation tendency of variables in the vertical direction in the channel, the averages of the variables on the horizontal lines are calculated. We define the horizontal line average function $\overline{g(z)}$ for a variable $g(x,z)$ to be the integration of the absolute value of $g(x,z)$ on a horizontal line at depth z in the channel divided by the channel width W:

$$\overline{g(z)} = \frac{\int |g(x,z)|\, dx}{W}. \tag{3.1}$$

Figure 3.3 shows the normalized average functions along the line for the time-averaged horizontal (u_2, black) and vertical (v_2, green) components, respectively. The u_2 is zero at the bottom; it reaches to the maximum at around z=2.23δ_ν (0.338 μm); it starts to decrease to another minimum at the center of the vortices; then it increases again with increase in the z value. The value of v_2 is zero at the bottom; it reaches to the first maximum at z=21.179 μm (vertical position of the center of the vortices); and it decreases to zero again at the top of the domain. The $\overline{g(z)}$ of the curl of the force source term ($\nabla \times \boldsymbol{F_s}$) and the mass source term (m_s) is normalized based on their maximum value (1.066×10^{14} N/m^4 at z=0 for m_s and 56.245 Pa • s/m^2 at z=0 for $\nabla \times \boldsymbol{F_s}$). These values vibrate sharply

within the area of z ⊂ $[0,12\delta_\nu = 1.76\ \mu m]$. The sharp vibration section of the curves is zoomed in in the right-top corner of Figure 3.3.

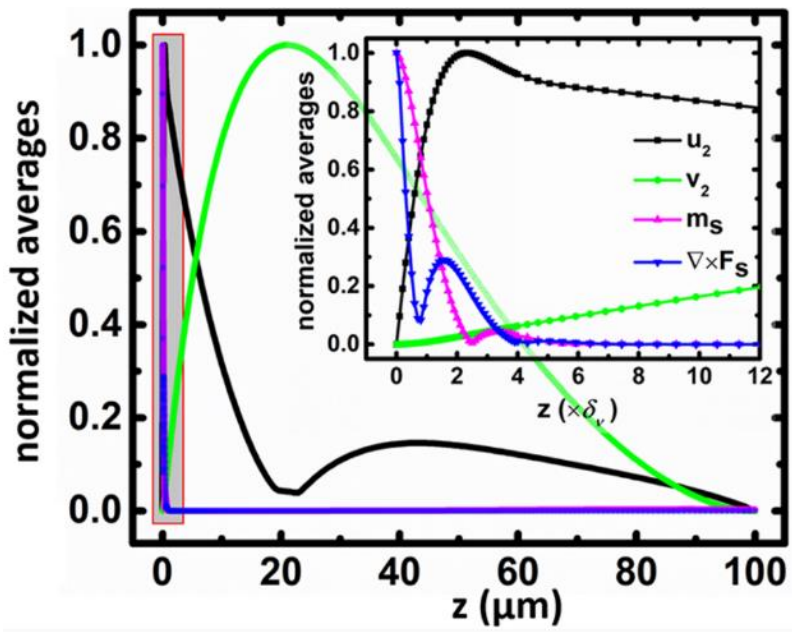

Figure 3.3: Change of the normalized line averages $\overline{g(z)}$ over z value. The normalized $\overline{g(z)}$ was measured for the variables including absolute value of $\boldsymbol{u_2}$ (horizontal component of streaming velocity), $\boldsymbol{v_2}$ (vertical component of streaming velocity), $\boldsymbol{m_s}$ (mass source term) and $\boldsymbol{\nabla \times F_s}$ (curl of the force source term).

3.1.2 Boundary driven streaming

As stated by Sadhal (Sadhal, 2012), acoustic streaming can be categorized into two main types—the Eckart streaming, which results from spatial attenuation of waves in free space, and boundary-driven streaming, which is due to the friction between a solid wall and a fluid medium and is mainly confined within the thin boundary layer. The theory of boundary-driven streaming, which is a major type of acoustic streaming found in the fluid environment of microfluidic devices, is the basic foundation for a solution to this problem (Sadhal, 2012). Based on the principle of boundary-driven streaming, the acoustic

streaming is generated because of the friction between a vibrating interface between the solid and the liquid domain. This effect mainly exists within a thin viscous layer adjacent to bottom boundary of the fluid domain. The thickness of this layer is close to the Stokes boundary layer. The thickness of the Stokes boundary layer in in the range of $\mathcal{O}\left(\sqrt{2\nu/\omega}\right)$, where ν is the kinematic viscosity of fluid and ω is the angular frequency of the acoustic wave (Manor, Yeo, & Friend, 2012). Because of the significant viscous dissipation lies in this viscous boundary layer, a steady fluid motion called inner streaming or Schlichting streaming is driven in the viscous boundary layer (Manor et al., 2012; Rayleigh, 1884; Sadhal, 2012; Wiklund et al., 2012). The velocity of the inner streaming at the top of the boundary layer is called "slip velocity". This "slip velocity" drives the fluid motion in the fluid upon the inner streaming domain, which is called outer streaming or Rayleigh streaming (Figure 3.4).

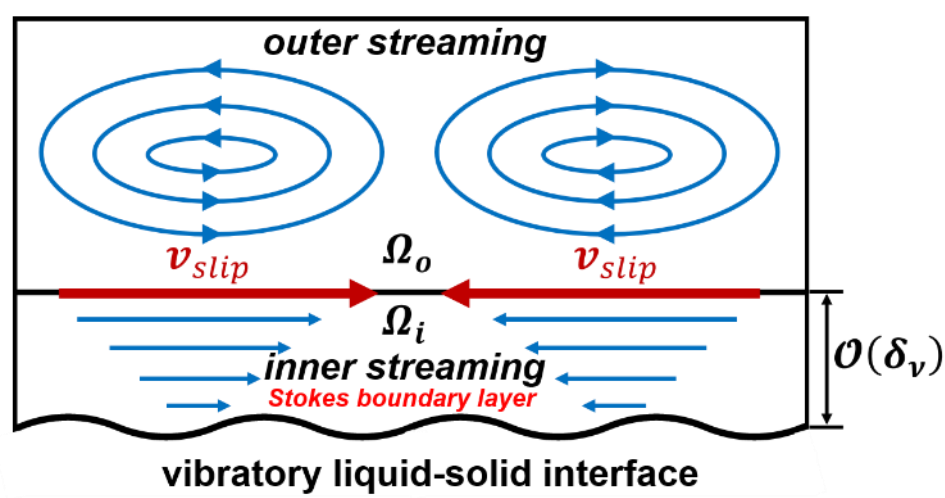

Figure 3.4: Boundary driven streaming.

3.1.3 Slip Velocity Method

Based on the above-mentioned boundary-driven streaming mechanism, we speculate that if one knows the profile and value of the "slip velocity", the outer streaming pattern can be solved as the fluid motion driven by the "slip velocity" at the bottom of the domain. In this way, there will be no need of solving the 1st-order and 2nd-order acoustic streaming governing equations (Guo, Mao, Chen, Xie, Lata, Li, Ren, Liu, Yang, Dao, et al., 2016; Nama et al., 2015) in the bulk fluid domain. In this regard, numerical simulations require large calculation amount can be performed efficiently. Here, we present a novel numerical simulation strategy – the "slip velocity method" – to analyze acoustic streaming based on the acoustic fields and inner streaming within the viscous boundary layer. We used the "slip velocity method" to solve the acoustic streaming in the SSAW device as shown in Figure 3.1. By comparing the solution from this method to the solution from the traditional method, we validated the feasibility of the "slip velocity method".

From the exploration in the previous subsection, the value of the mass source term and body force term and the resulting second order acoustic streaming velocity is much large in a thin layer near the bottom of the channel than elsewhere. The SSAW-induced acoustic streaming in the microfluidic channel in Figure 3.1 is considered as boundary-driven streaming. As a result, the Rayleigh streaming in Ω_o can be solved based on the original fluid governing equation with "slip velocity" as the boundary condition at the bottom.

Using the "slip velocity method", the outer streaming can be solved by following three steps. (1) Solve the acoustic field (Eqs. (2.16) and (2.17)) in Ω_i (inner streaming domain). (2) Solve the acoustic streaming pattern (based on 2nd-order Eqs. (2.20) and (2.21)) in Ω_i. Then, capture the value of the acoustic streaming velocity at the interface between Ω_i and Ω_o as $\boldsymbol{v}_{slip}$ (slip velocity). (3) Solve the original governing equations for the fluid motion (Eqs. (2.7) and (2.8)) in Ω_o (the outer streaming domain) and applied $\boldsymbol{v}_{slip}$ as the boundary condition at the bottom of Ω_o.

A COMSOL model was set up following this three-step procedure of the "slip velocity method". (1) Apply a "Thermoviscous Acoustics" interface solve the acoustic field governed by Eqs. (2.16) and (2.17) in Ω_i. Eqs. (2.5) and (2.6) (standing SAW vibration velocity) were applied at the bottom of the domain as the boundary condition. The "normal impedance" condition with the value of PDMS's impedance was applied to the channel walls. At the top of the Stokes boundary layer (Σ), the "normal impedance" condition with the value of water's impedance was applied. A "Frequency Domain" solver is applied to solve the problem at 13 MHz. (2) Appy a "Laminar Flow" interface to solve the inner acoustic streaming in Ω_i (Eqs. (2.20) and (2.21)). A "no slip wall" condition was applied to the bottom, left, and right boundaries. Apply an "outlet" condition to set the pressure at the top of the domain to zero. A "Stationary" solver to solve the steady inner acoustic streaming was applied. Last, the distribution of the streaming velocity at the top of the inner streaming domain ($\boldsymbol{v}_{slip}$) was extracted. (3) Another "Laminar Flow"

interface to solve the original continuity and Navier-Stokes equations (Eqs. (2.7) and (2.8)) in the outer streaming domain (Ω_o) was applied. The $\boldsymbol{v}_{slip}$ acquired in Step (2) to the bottom of the outer streaming domain was used as a "slip wall" condition. The boundary conditions at other boundaries of domain Ω_o to a "no slip wall" condition was set. A "Stationary" solver to solve the streaming pattern in Ω_o was applied. The domain is divided into mapped rectangular meshes. The height of the elements in the Stokes boundary layer was set to $\delta_v/10$. Height of elements in the bulk fluid were set to 0.2 μm. This mesh division reaches the requirement of the mesh convergence requirement (Nama et al., 2015). This mesh was reliable to acquire results which sufficient accuracy.

As the outer streaming is activated by $\boldsymbol{v}_{slip}$ in the slip velocity method, determining the thickness of the inner streaming domain (h) which provides the accurate $\boldsymbol{v}_{slip}$ is essential for the accuracy of the entire streaming pattern. As shown in Figure 3.3, the amplitude of u_2 varies sharply near the bottom of the inner streaming domain. Thus, slightly shifting the position of Σ will significantly vary the value of "slip velocity" and the resultant outer streaming pattern. Determining the position of Σ at where u_2 reaches the maximum is not proper because the value of u_2 has the fluctuant distribution in horizontal lines. Considering this, we explored the distribution of the mass source term (m_s) and the curl of the force source term ($\nabla \times \boldsymbol{F_s}$) as well. As shown in Figure 3.3, the averaged absolute mass source term decreases sharply from its maximum at z=0. In the area above the horizontal line z=5δ_v, the amplitude of m_s becomes much smaller than the

one below the line z=5δ_ν. This indicates that the mass source term mainly affects in the area within z=5δ_ν. For the distribution of the curl of the force source term ($\nabla \times \boldsymbol{F_s}$), which is the main factor of the streaming vortex, also affects mainly in this area (Figure 3.3). The mass source term and force source terms embody the effect of the acoustic field on the acoustic streaming. Thus, this effect mainly penetrates a fluid layer near the bottom (~5δ_ν) and induces the fluid motion. As a result, the thickness of the inner streaming layer was optimized to be ~5δ_ν for the "slip velocity method". To verify this conclusion, the "slip velocity method" is applied to solve the outer streaming with various thicknesses of Ω_i, and we compared the results of each setting with the corresponding streaming velocity solved by the traditional approach. The results are stated and discussed in the next subsection.

3.1.4 Validation of the slip Velocity Method

To evaluate the similarity between two solutions (one from the traditional method, and another one from the slip velocity method), we calculated a relative convergence function to evaluate the similarity of a solution $g(x,z)$ solved by the slip velocity method and a reference solution $g_{ref}(x,z)$ solved by the traditional approach in the entire computational domain. The convergence function is defined as

$$C(g) = \sqrt{\frac{\int (g - g_{ref})^2 dV}{\int {g_{ref}}^2 dV}}, \tag{3.2}$$

where V is area of a 2D computational domain or the volume of a 3D computational domain. Small values of the convergence function value indicates a good similarity comparing with the reference solution. We calculated the convergence function for the horizontal component (u_2) and vertical component (v_2) of the inner streaming velocity in Ω_i, the horizontal component (u_{slip}) and vertical component (v_{slip}) of the slip velocity at the interface Σ, and the horizontal component (u_{outer}) and vertical component (v_{outer}) of the outer streaming velocity in Ω_o.

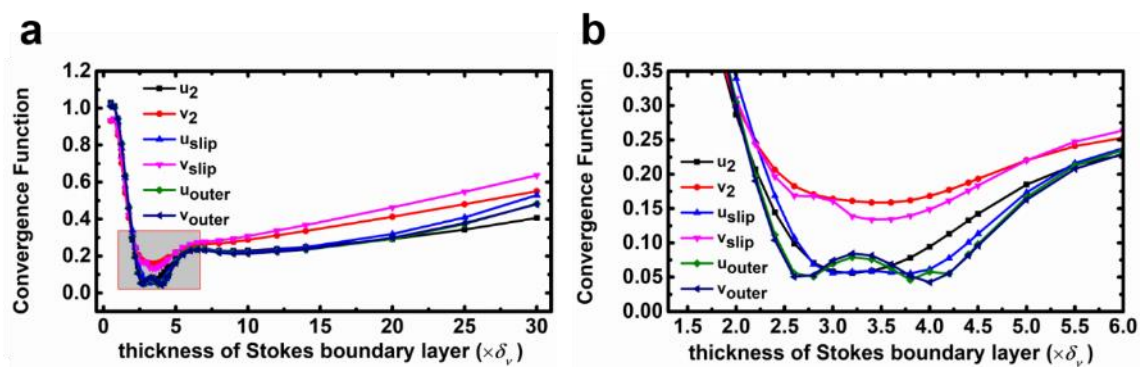

Figure 3.5: The change of the convergence functions the variables over the inner streaming domain thickness (h). The convergence functions were calculated for the following variables: (1) horizontal and vertical components of the inner streaming velocity ($\boldsymbol{u_2}$ and $\boldsymbol{v_2}$ in $\boldsymbol{\Omega_i}$), (2) horizontal and vertical components of the slip velocity ($\boldsymbol{u_{slip}}$ and $\boldsymbol{v_{slip}}$ on $\boldsymbol{\Sigma}$) , and (3) horizontal and vertical components of the outer streaming velocity ($\boldsymbol{u_{outer}}$ and $\boldsymbol{v_{outer}}$ in $\boldsymbol{\Omega_o}$). The horizontal axis is the value of $\boldsymbol{\Omega_i}$ thickness shown in the format of the times of the $\boldsymbol{\delta_v}$ (0.147 **μm** for 13 MHz frequency in the water). The convergence of the $\boldsymbol{u_{outer}}$ and $\boldsymbol{v_{outer}}$ reach their minimums of 0.04594 at h=3.8$\boldsymbol{\delta_v}$ and 0.04256 at h=4$\boldsymbol{\delta_v}$, respectively. This result implies that setting h=4$\boldsymbol{\delta_v}$ is optimal for slip velocity method to produce a solution with good similarity to the traditional approach.

The results of the convergence study are shown in Figure 3.5. The curves of the convergence functions are plotted as a function of thickness of inner streaming domain (h). For the six variable we studied for the convergence, the values of the functions exhibit

similarly that decreases to the minimum at the h range of [2.5δ_v, 4δ_v] and increases again. The optimal value of h lies in this area. As shown in Figure 3.5b, $C(u_2)$ has a minimum value of 0.05602 at h=3.2δ_v, $C(v_2)$ has a minimum value of 0.15873 at h=3.4δ_v, $C(u_{slip})$ reaches a minimum of 0.05547 at h=3.8δ_v, $C(v_{slip})$ reaches to the minimum of 0.13386 at h=3.4δ_v. As the goal of this study is to optimizing the accuracy of the outer streaming velocity, the minimum value of $C(u_{outer})$ appears at h=3.8 δ_v as 0.04594, and the minimum value of $C(v_{outer})$ appears at h=4δ_v as 0.04256. These data indicate that setting h value to ~4δ_v in the slip velocity method can yield the best approximation to traditional research. As shown in Figure 3.3, the amplitude of the mass source term and the curl of the force source term also vanish close to zero at ~4δ_v. Setting the inner streaming domain is thinner than ~4δ_v will reduce the effective mass source and force source terms. If the inner streaming domain is thicker than ~4δ_v, u_{slip} will greatly decrease from its maximum, and the v_{slip}will increase. This setting makes the amplitude of the outer streaming smaller than the solution of the traditional solution.

In summary, by setting the thickness of the inner streaming domain to h=4δ_v, the convergence function values of outer streaming components are in the 10^{-2} order, which indicates a good approximation (Nama et al., 2015). As a result, the optimal thickness of the inner streaming domain (Ω_i) is determined to 4δ_v and will be applied in future numerical simulation using the slip velocity method.

Setting h=4δ_v, the "slip velocity method" takes 1227 s to solve the 2D acoustic streaming shown in Figure 3.1. Using the traditional approach takes 2620 s to solve the same problem. Thus, we estimate that the "slip velocity method" saves the time of the computation by 53% compared to the traditional approach.

For further validation, we applied the "slip velocity method" to solve a small-scale problem that is the acoustic streaming in the λ/3-thick 3D PDMS channel shown as shown in as shown in Figure 3.6. The device parameters and design follow the ones reported in Guo's work (Guo, Mao, Chen, Xie, Lata, Li, Ren, Liu, Yang, Dao, et al., 2016).

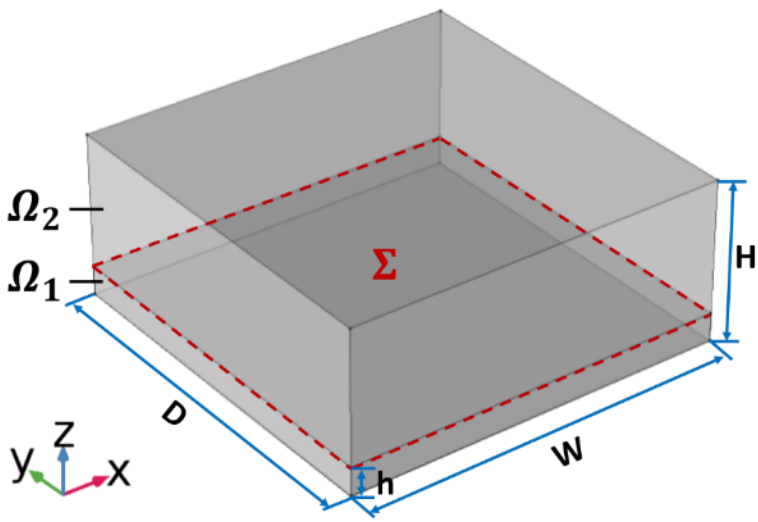

Figure 3.6: Simulation domain of the 3D numerical model.

The results for the device of one pair of IDTs (Figure 3.7) and the device with two pairs of IDTs (Figure 3.8), especially the streaming patterns on x-z planes and x-y-top plane accord well with the results reported in Guo's work (F. Guo, Proc. Natl. Acad. Sci., 2016, 113, 1522–1527.).

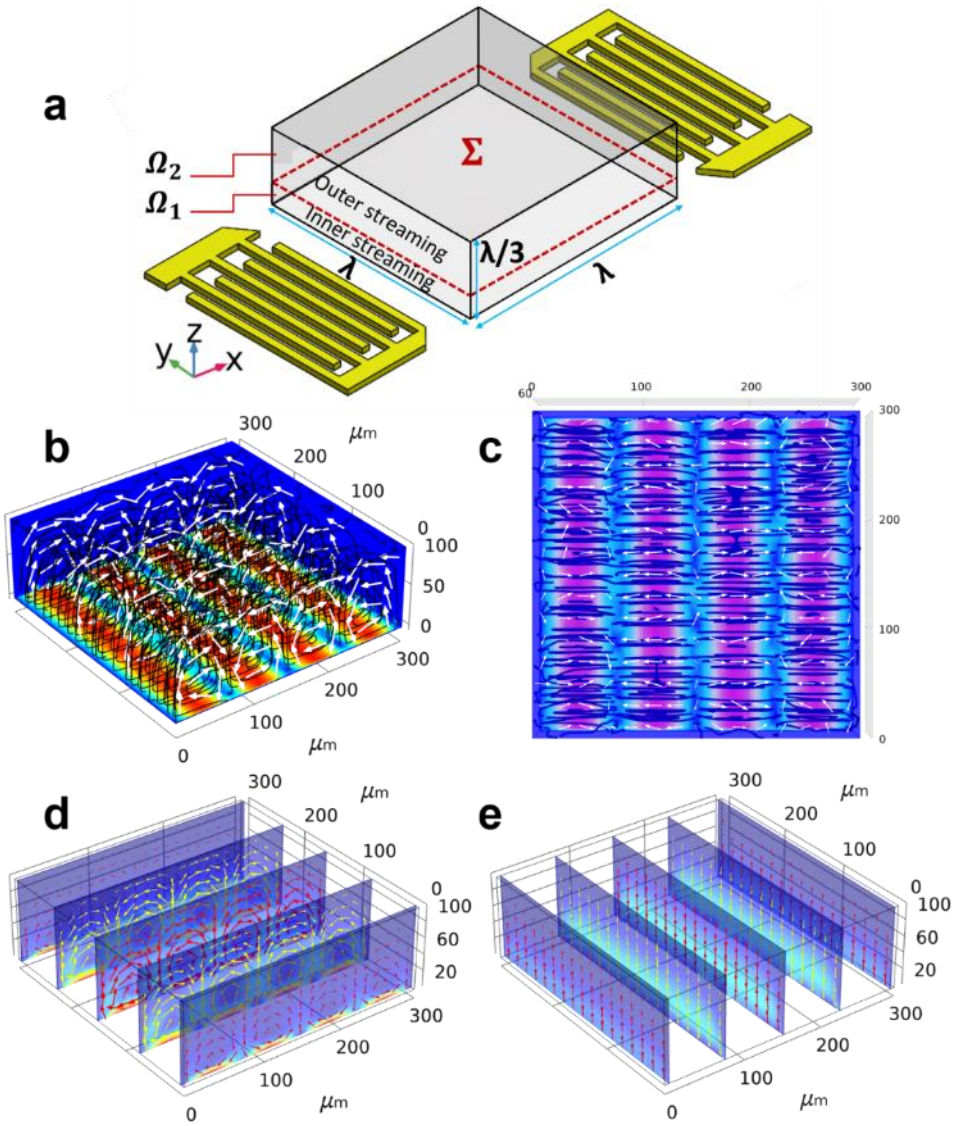

Figure 3.7: 3D streaming pattern in classic standing SAW device with one pair of IDTs. a, Schematics of the device. The square PDMS chamber is λ in width and λ/3 in thickness. b, Simulation result of acoustic pressure at bottom and 3D acoustic streaming pattern. c, Top-view of the streaming pattern. d, e, 2D acoustic streaming pattern on several x-z cross sections and y-z cross sections, respectively.

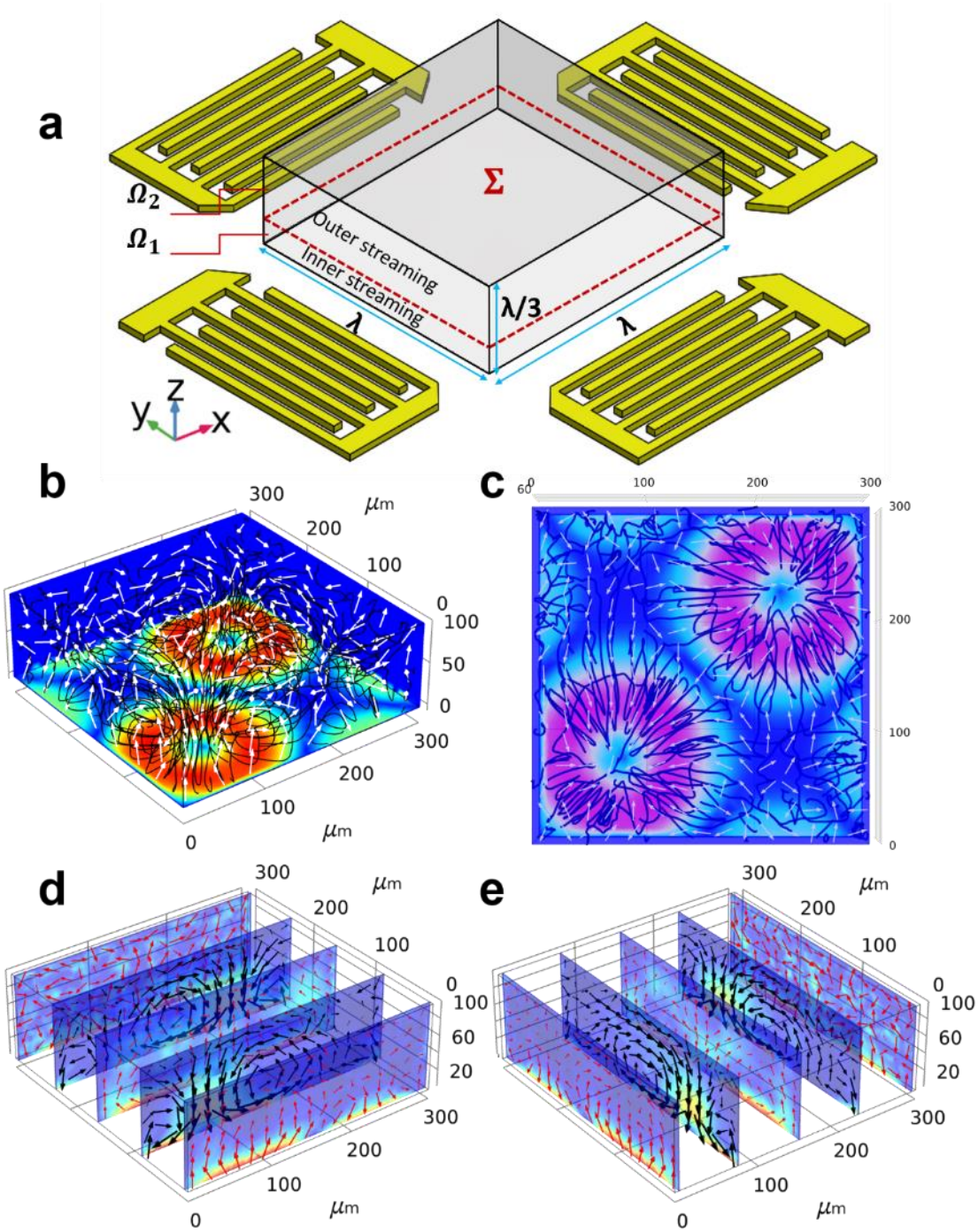

Figure 3.8: 3D streaming pattern in classic standing SAW device containing two pairs of IDTs. a, Schematics of the device. The square PDMS chamber is λ in width and $\lambda/3$ in thickness. b, Simulation result of acoustic pressure at bottom and 3D acoustic streaming

pattern. c, 2D streaming pattern from the top-view. d, e, 2D acoustic streaming pattern on several x-z cross sections and y-z cross sections, respectively.

3.2 Vortex streaming generated by IDTs merged in the oil

In this section, we explored the 3D vortex streaming pattern generated by an IDT merged in the viscous liquid and applied this streaming pattern for liquid droplet handling.

3.2.1 Motivation

Acoustic streaming, a steady flow induced by acoustic waves, has been applied for various microfluidic application, including particle manipulation (Gu et al., 2020; Guo et al., 2015), fluid pumping (Du et al., 2009), and fluid mixing (Huang et al., 2014; Nama, Huang, Huang, & Costanzo, 2014). Researchers have explored the acoustic streaming pattern in the devices from the two-dimensional perspective. In the acoustofluidic devices in which the acoustic wave propagation and the resulting streaming pattern is uniform along a certain direction, the 3D streaming pattern can be approximately reconstructed based on the 2D streaming pattern. 2D numerical simulations have been carried out to efficiently explore the acoustic streaming activated by bulk acoustic waves (BAWs) or surface acoustic waves (SAWs) in narrow fluid domains at the micrometer scale (M. Alghane, Fu, et al., 2012; Guo, Mao, Chen, Xie, Lata, Li, Ren, Liu, Yang, Dao, et al., 2016; Mao et al., 2017; Muller & Bruus, 2015; Nama et al., 2014; Shilton, Travagliati, Beltram, & Cecchini, 2014; Yeo & Friend, 2009). For the analysis of the acoustic streaming generated by BAWs or SAWs outside the transducer area (Huang et al., 2014; Mao et al., 2017; Muller

& Bruus, 2015; Nama et al., 2014), a common method is simplifying the 3D problem to a 2D simulation. This method is available for the fluid domain in which acoustic waves are approximately uniform along the direction perpendicular to the 2D plane of the simulation.

However, this 2D simplification is not proper for the analysis of acoustic streaming pattern that is not uniform in a certain direction, for example the acoustic streaming induced by an IDT immersed in the infinite bulk liquid as shown in Figure 3.9a. For this case, the transducer on the piezoelectric substrate generates travelling SAWs which propagate symmetrically away from the center of the IDT and perpendicularly to the IDT fingers. As the bulk liquid domain is directly loaded on the IDT area, the SAWs decay while they are generated. And the IDTs also generate transverse radiation components and oblique radiation components in the IDT area (Holmgren et al., 2007; Inoue et al., 2013; Koskela, Knuuttila, Makkonen, Plessky, & Salomaa, 2001; Salim, Hashim, & Arshad, 2016). The waves generated by the IDT propagate into the liquid on the substrate and generate acoustic streaming in a three dimensional butterfly pattern (Du et al., 2009). Hence, in this subsection we seek to explore the three-dimensional substrate vibration, propagation of IDT-generated acoustic waves, and the pattern of the resultant acoustic streaming.

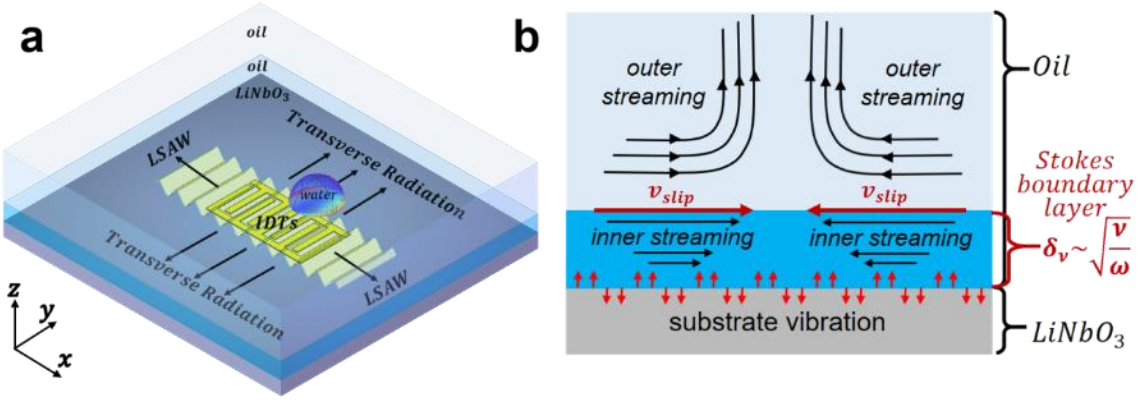

Figure 3.9: Schematic illustration of manipulating the droplet using the acoustic streaming generated by the IDT immersed in the oil. a, Device setup and working mechanism b, Schematic of boundary-driven streaming theory.

3.2.2 Numerical simulation

First, we performed the numerical simulation to analyze the pattern of acoustic streaming induced by an IDT immersed in the unconfined bulk liquid as shown in Figure 3.9a. In this setup, An IDT fabricated on a 128° Y-X cut $LiNbO_3$ piezoelectric substrate was immersed in the oil which is 2-mm in depth. The IDTs starts to generate vibration when AC signals are applied to it. The vibration propagates in the form of Rayleigh SAW (Holmgren et al., 2007; Inoue et al., 2013; Koskela et al., 2001)). When the SAWs propagate into the liquid loading on the substrate, the leaky SAWs will drive the acoustic streaming in the bulk oil domain. This subsection presents the theory and 3D numerical simulation to analyze the physics of IDT-activated acoustic streaming in the bulk liquid domain. The 3D computational domain of this multi-physical problem, which includes 3D substrate vibration, acoustic wave propagation, and IDT-activated acoustic streaming is sketched in Figure 3.10. We deduced the simulation domain to one fourth of the real problem

because the geometry and physics (*e.g.*, IDTs' vibration, SAWs propagation, and acoustic streaming pattern) in this setup is symmetrical in both the x- and y-directions. In this way, the computational effort can be reduced by 75%. Domains Ω_1, Ω_2, and Ω_3 are defined as the $LiNbO_3$ substrate, inner streaming fluid domain, and outer fluid streaming domain, respectively. The thickness Domains Ω_1, Ω_2, and Ω_3 are 500 μm, 1.62 μm ($4\delta_v$), and 2,000 μm, respectively. The solid-oil boundary (Σ_1) and inner-outer boundary (Σ_2), and oil-air boundary (Σ_3) are marked in the figure. The IDT fingers are set on the surface of the substrate (Σ_1).

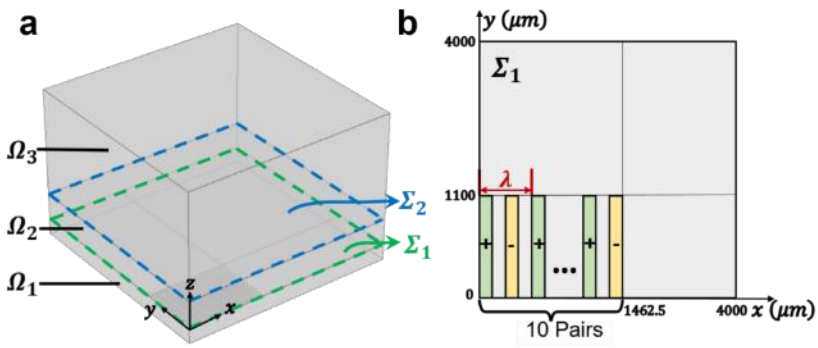

Figure 3.10: Computational domain. a, The 3D domain for the simulation of a quarter of IDT area. The depth of the domain was set to 0.5 mm, $\mathbf{4\delta_v}$, and 2 mm-$\mathbf{4\delta_v}$ for $\mathbf{\Omega_1}$, $\mathbf{\Omega_2}$, and $\mathbf{\Omega_3}$, respectively. The width of the domains is set to 4 mm. b, IDT fingers on $\mathbf{\Sigma_1}$. The IDT area is 1100×1462.5 μm^2.(C. Chen et al., 2018)

As shown in Figure 3.10, a quarter of the IDT, which is set on the top of the substrate (Σ_1), contains 10 pairs of fingers with the width of 37.5 μm. Thus, the driving frequency of the IDT is 23.9 MHz, which corresponds to SAWs with a wavelength in the substrate of 150 μm. If applying the perturbation-theory-based approach (Muller & Bruus, 2015) stated in Section 2.2.1, first-order equations (Eqs. (2.16) and (2.17)) need to be

solved in the whole fluid domain ($\Omega_2 \cup \Omega_3$) before solving the second-order equations (Eqs. (2.20) and (2.21)) for acoustic streaming pattern. The mesh division requirement for solving the acoustic field is at least 6 elements/wavelength in the direction of wave propagation (Łodygowski & Sumelka, 2006). To reach this requirement, at least ~1 million meshes will be need for solving the acoustic field in the fluid domain ($\Omega_2 \cup \Omega_3$, 4×4×2 mm^2). This mesh system requires an extremely large computational cost. Hence, some model simplification is required for solving the 3D acoustic streaming pattern in the bulk fluid domain.

Based on the boundary-driven streaming theory, and Manor *et al.* deduced formulas for the 2D "slip velocity" activated by the SAW outside the IDT area decomposed into two components perpendicular to IDT fingers and perpendicular to the substrate (Melde, Mark, Qiu, & Fischer, 2016). However, the SAW propagation in the area containing IDT area needs to account for wave reflection among electrodes and a third vibration component along the IDT fingers because of the transverse and oblique radiations (Holmgren et al., 2007; Inoue et al., 2013; Koskela et al., 2001; Salim et al., 2016). Due to this complicated substrate vibration mode in the area involving the IDT, deducing formulas for the "slip velocity" induced by the SAW propagating in and around the IDT in SAW microfluidics is not feasible.

As the IDT-induced acoustic streaming is dominated by boundary-driven streaming theory (Section 3.1.2 and Figure 3.9b), the "Slip Velocity Method" stated in the

Section 3.1.3 provides an approach to reduce the computational cost the abovementioned problem (Sadhal, 2012). In this subsection, we applied the "slip velocity method" to analyze the 3D acoustic streaming pattern activated by an IDT immersed in bulk liquid. By applying this method, the calculation amount of the numerical simulation for the acoustic filed in the whole fluid domain can be reduced to the solution in the thin boundary layer. And the 3D streaming pattern in the bulk fluid can be solved based on the "slip velocity" acquired on the top of the boundary layer.

In the 128° Y-X cut $LiNbO^3$, the substrate can be strained by applying an electric signal because of the piezoelectric effect. The mechanical vibration and the electrical behavior are governed by the momentum equations for solid mechanics and the charge conservation equation, respectively. The coupling relationship between stress, strain, electrical displacement field, and the electric field of a piezoelectric crystal is governed by the constructive equations in the stress-charge form as expressed in Eqs. (2.1) and (2.2). The substrate vibration problem was solved within the Domain Ω_1.

The perturbation approach (Muller & Bruus, 2015) stated in Section 2.2.1 is applied to separate the governing equations (Eqs. (2.7) and (2.8)) into first-order equations that govern the acoustic field (Eqs. (2.16) and (2.17)) and time-averaged second-order equations that acoustic streaming (Eqs. (2.20) and (2.21)). As shown in Fig. 1(b), the oil domain can be divided into two parts: a thin viscous boundary layer corresponding to the "Stokes boundary layer" (Ω_2), and the rest of the oil domain outside the thin layer (Ω_3).

The viscous boundary layer with a thickness several times that of $\delta_v = \sqrt{2\nu/\omega}$, which relates the ratio between the kinematic viscosity of the liquid (ν) and the angular frequency of the SAW (ω). This is a liquid domain where the viscous dissipation of the leaky SAWs is extremely high due to the non-slipping boundary of the vibrating surface. As given in the second-order equations, Eqs. (2.20) and (2.21), the viscous dissipation generates mass and force sources confined mainly within the thin layer and drives a flow called Schlichting streaming or inner streaming inside the layer (Manor et al., 2012; Sadhal, 2012). On the other hand, the streaming outside that thin layer in the rest of liquid domain, named Rayleigh streaming or outer streaming, can be considered as driven by the inner streaming because of the continuity of the streaming velocity from the boundary layer to the outside domain.

Using this approximation, the computation of this 3D model can be significantly reduced by solving the acoustic field (1st-order problem) and the inner streaming (2rd-order problem) within the viscous boundary layer. For the oil at 23.9 MHz, the value of δ_v is ~405 nm, which is 2.025×10^4 times thinner than that of the whole oil domain of thickness 2,000 μm. As discussed above, setting thickness of the inner streaming domain to be ~$4\delta_v$ in the slip velocity method yields the best approximation to traditional research. So for this case, the inner streaming domain thickness was set to 1.62 μm. The inner streaming velocity distribution on the top of the viscous boundary layer is captured as the "slip velocity", which has been conventionally defined in microfluidics as the relative

velocity between the fluid and the solid boundary (B. Li & Kwok, 2003; Lu, Duan, & Wang, 2015). The outer streaming can be obtained by solving the original continuity and Navier-Stokes equations, *i.e.*, Eqs. (2.7) and (2.8), in the outer streaming domain (Ω_3) and applying the "slip velocity" as the boundary condition at the bottom of this domain.

Based on the slip velocity method, the streaming pattern is numerically explored in the following three steps: (1) solving the coupled interaction between substrate vibration in Ω_1 and the acoustic field (1st-order problem) in Ω_2; (2) solving the 2nd-order problem in Ω_2 based on the 1st-order result from the former step and obtaining the "slip velocity"; and (3) solving the original governing equations in Ω_3 and applying the "slip velocity" at Σ_2 as the boundary condition to obtain the outer streaming. COMSOL 5.2a (the COMSOL Group) was employed for the calculation according to the above-mentioned steps. In step (1), the predefined "Solid Mechanics" and the "Electrostatics" physics were used to calculate the piezoelectric substrate's vibration governed by Eqs. (2.1) and (2.2) in Ω_1. The positive and negative electric potential boundary conditions were applied to, respectively, the green fingers and yellow fingers as shown in Figure 3.10b. The "Thermoviscous Acoustics" physics was used to solve the acoustic field (1st-order problem) governed by Eqs. (2.16) and (2.17) in the inner streaming domain Ω_2. A "Symmetry" boundary condition, which confines the normal component of the 1st-order velocity on the boundary to be zero, was applied to the x-0-z and 0-y-z planes. To eliminate wave reflection, other peripheral boundaries and Σ_2 (oil-oil interfaces) of Ω_2 were set as the "normal

impedance" equal to that of the fluid in Ω_2. A velocity continuity boundary condition was applied to Σ_1 to constrain the two-way coupled interaction between the physics of "Solid Mechanics" and "Thermoviscous Acoustics". Based on these settings, a "Frequency Domain" solver was used to solve all the above-mentioned physics together at the driving frequency (23.9 MHz). In step (2), the "Laminar Flow" physics was used to solve the 2nd-order problem governed by Eqs. (20) and (21) in Ω_2. The mass and force source terms were imposed by adding "weak contribution" and "volume force" conditions, respectively. Similarly, a "Symmetry" boundary condition confined the normal 2nd-order velocity at x-0-z and 0-y-z planes to be zero. And an "outlet" boundary condition, which indicates no pressure difference on the two sides of a boundary, was imposed to the oil-oil interfaces, *i.e.* Σ_2 and the other two peripheral boundaries. This physics is solved *via* a "Stationary" solver by using the 1st-order solution of the previously mentioned "Frequency Domain" solver. After acquiring the 2nd-order solution, the time-averaged 2nd-order velocity on Σ_2 was obtained as the "slip velocity". As the last step, the normal continuity and the Navier-Stokes equations (Eqs. (2.7) and (2.8)) were calculated in another "Laminar Flow" solver to simulate the outer streaming in Ω_3. The "slip velocity" found in the former step is applied as the motivation at the bottom of Ω_3. Meanwhile, a "slip wall" condition, where no normal velocity component exists, is applied to the top of Ω_3 (oil-air interface), and an "outlet" condition was applied to the periphery of Ω_3 (oil-oil interfaces). The last

step was to use another "Stationary" solver to solve the "Laminar Flow" physics, ultimately achieving the solution of outer streaming.

The substrate vibration in Ω_1, acoustic field, and inner streaming in the inner streaming domain (Ω_2) were solved together in Step (1). Figure 3.11a shows the numerical displacement of the substrate at the frequency of 23.9 MHz and input peak-to-peak voltage of 40 V. Under this condition, the peak value of displacement reached ~3.5 nm, and the vibration originating from the IDTs area propagated in the x and y directions. Figure 3.11b shows the distribution of displacement amplitude U and the three decomposed components u_0, v_0, and w_0 along the x, y, and z axes, respectively, along a cut line (y=100 μm) on the surface of the substrate. As displayed in these curves, the amplitude of v_0, the displacement component along the IDTs fingers which is typically ignored in 2D analysis, is comparable to u_0 and w_0. This suggests that its effect on the acoustic streaming motion in the y direction would be non-negligible in this problem.

At the substrate-oil interface, the velocity continuity boundary condition was provided to couple the physics in the substrate and oil. Together with this boundary condition, the 1st-order equations were solved within the viscous boundary layer to obtain the acoustic pressure. In Figure 3.11c, the acoustic pressure distribution on the substrate-oil interface shows that at the resonance frequency, the acoustic pressure amplitude in the IDT area reached ~0.4 MPa, which was much stronger than the waves propagating outward in the x and y directions. The vibrating fingers generated SAW that leaked into

the loading oil as leaky SAW that propagated upwards into the oil. Since each pair of IDT fingers generated SAW propagating in the +x and -x directions simultaneously, there were standing SAWs in the IDTs area and traveling SAWs outside the IDT area that decayed exponentially with the propagation distance. Additionally, the up-and-down vibration of the IDT fingers could also produce a component of BAW directly into the loading oil. Thus, the BAW and standing leaky SAW in the oil upon the IDT area and the traveling leaky SAW in the oil outside the IDT area collectively resulted in a higher acoustic pressure inside the IDTs area than outside the IDTs.

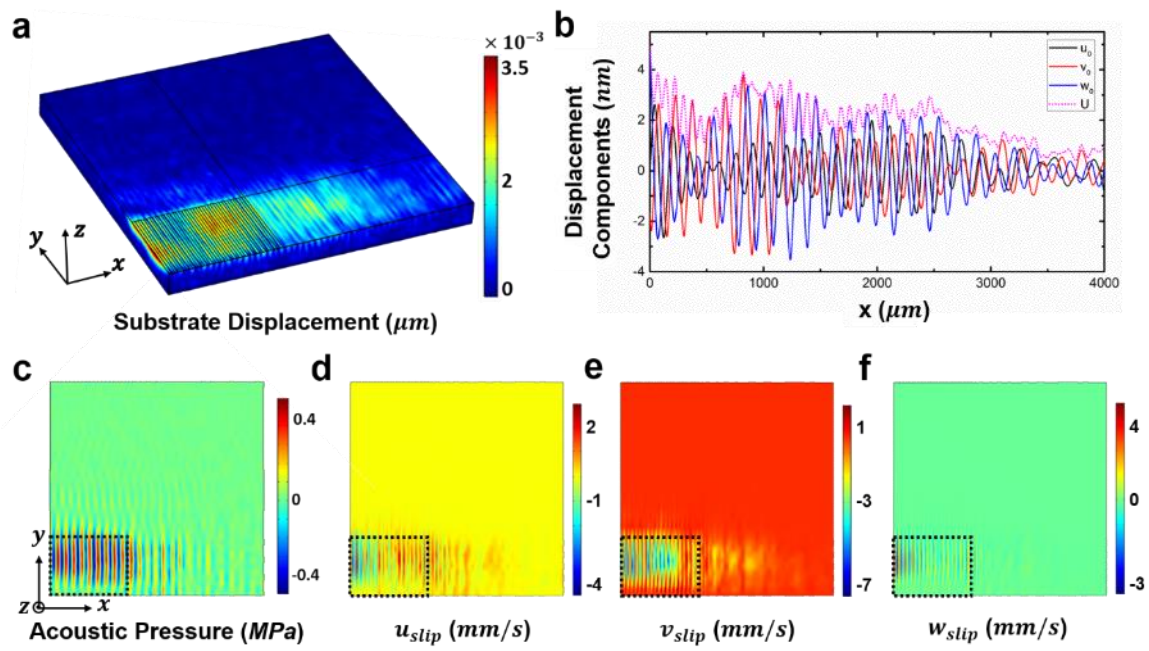

Figure 3.11: Simulation results in the substrate (Ω_1) and inner streaming domain (Ω_2) when the IDT was activated at the frequency of 23.9 MHz and the voltage of 40 V_{PP}. The calculation area is quarter of the IDT area using the symmetry boundary condition. a, The amplitude of substrate displacement. b, Distribution of displacement components on a line (y=100 μm) on the floor of the substrate ($\boldsymbol{\Sigma_1}$). $\boldsymbol{U}$, $\boldsymbol{u_0}$, $\boldsymbol{v_0}$, and $\boldsymbol{w_0}$ are the amplitude, x component, y component, and z component of displacement, respectively. The value of y

displacement component along the fingers ($\boldsymbol{v_0}$) is comparable to other components. c, Acoustic pressure distribution on the floor of substrate. The acoustic energy is mainly concentrated in the IDT area and propagates along both x and y directions. d-f, The decomposed "slip velocity" in x, y, and z directions on the top of the inner streaming domain ($\boldsymbol{\Sigma_2}$). The dotted boxes in (c)-(f) indicate the IDT area.

Based on the 1st-order results, the 2nd-order equations were solved in the viscous boundary layer. The 2nd-order velocity on the top of the viscous boundary layer (Σ_1) was the "slip velocity". Figure 3.11d-f show the decomposed "slip velocity" in which u_{slip}, v_{slip} , and w_{slip} represent the velocity components in the x, y, and z directions, respectively. Similar to the acoustic pressure distribution, the "slip velocity" in the area above the IDTs was faster than elsewhere. As shown in Figure 3.11d, u_{slip} near the right boundary of the IDTs area was almost positive, while it is mostly negative on the left side of this area. Because of the symmetric boundary condition on the left boundary ($u_{slip}\big|_{x=0} = 0$), the oil in the outer streaming domain (Ω_2) could be pumped towards +x. As shown in Figure 3.11e, the magnitude of the negative v_{slip} appeared in the IDTs area periodically and reached about -7 mm/s, which was much larger than its maximum positive value (~1 mm/s). As v_{slip} dominated the y component of the outer streaming, the oil in the outer streaming domain was attracted in the -y direction toward the IDT. This phenomenon could be the key to the formation of the counter vortex in the outer streaming domain.

By setting the velocity at the bottom of the outer streaming domain (Σ_2) to be the "slip velocity", the outer streaming in the oil domain (Ω_3) was obtained by solving Eqs.

(2.7) and (2.8). Figure 3.12a, shows the numerical result of the 3D outer streaming field. Red streamlines and black arrows indicate streaming velocity distribution and direction, respectively. The streaming patterns in the x-y-2000 μm, 0-y-z, x-0-z and planes are plotted to illustrate the intuitive formation of 3D outer acoustic streaming as shown in Figure 3.12b.

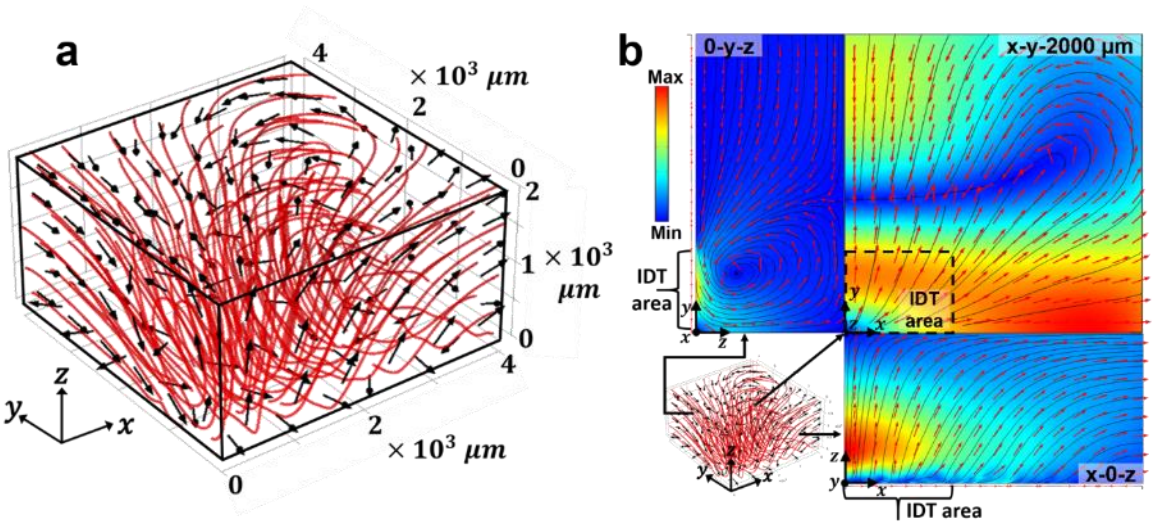

Figure 3.12: Numerical and experimental results of acoustic streaming in an outer oil domain (Ω_3) in our SAW microfluidic device. a, Numerical results showing outer streaming pattern in the 3D domain. b, The streaming patterns on three typical planes, *i.e.*, x-y-2000 μm, 0-y-z, and x-0-z planes, are plotted for illustration.

Figure 3.13 compares the numerical and experimental streaming pattern on 2D planes. The streaming patterns were measured by recording trajectories of the beads (1.9 g/cm^3, 30 μm in diameter) on the corresponding planes, and stacking a series of frames of the recorded video. The outer streaming on x-0-z (Figure 3.13i and j) was drawn to flow in the +x direction by the u_{slip}. The mechanism is that the IDT-activated SAW propagating in x direction leaked into the oil and pumped out the loading oil upon it. As can be seen

in Figure 3.13j, the numerical streamline (yellow) was captured from the streaming patterns in Figure 3.13i. These overlapped with the experimentally measured flow directions from a side view (the trajectories of the white beads). Both the experimental and simulated results indicate that the flow direction of the pumped-out oil flow had a 34° angle with the z direction. This angle is much larger than the Rayleigh angle (10° for incidence from $LiNbO_3$ to oil), which is the angle of the leaky wave propagation and initial streaming direction when the SAW first met liquid outside the IDT area (Frommelt et al., 2008). Considering that the SAW begins to leak into the liquid at its initial position, each IDT actually serves as a line source that keeps generating the cylindrical waves. These waves interfere with the leaky waves based on the Huygens-Fresnel principle (Devendran, Collins, Ai, & Neild, 2017). Thus, the interferential waves have a larger angle compared to the individual leaky waves on the edge of IDTs area. On the 0-y-z plane (Figure 3.13g and h), the oil was drawn in the -y direction towards the IDTs area by v_{slip}. Due to the symmetric motion of the IDT, the oil was ejected to the oil-air surface near the x=0 boundary and flowed to the +y direction. On the oil-air boundary, the flow in the +y direction inside the IDT area blocked the flow in the opposite direction outside the IDT area and surged towards the substrate together. As a result, a "counter flow" formed, and this result matched well with the measured streamline shown in Figure 3.13h. As seen from the x-y-2000 μm plane, the counter flow obstructed the backflow in the -y direction, thereby forming a "stagnation point", *i.e.*, the hydrodynamic trap for floating objects at

the side of the IDTs. The stacked image of particle trajectories on the oil-air surface confirmed that the streamlines on the oil-air interface ended at the "stagnation point" on the sides of the IDTs, and this experimental observation agrees with the simulated streamlines (Figure 3.13e and f). In addition, streamlines at 100 μm and 1,000 μm oil depth further confirm the consistency between simulation and experiment (Figure 3.13a-d).

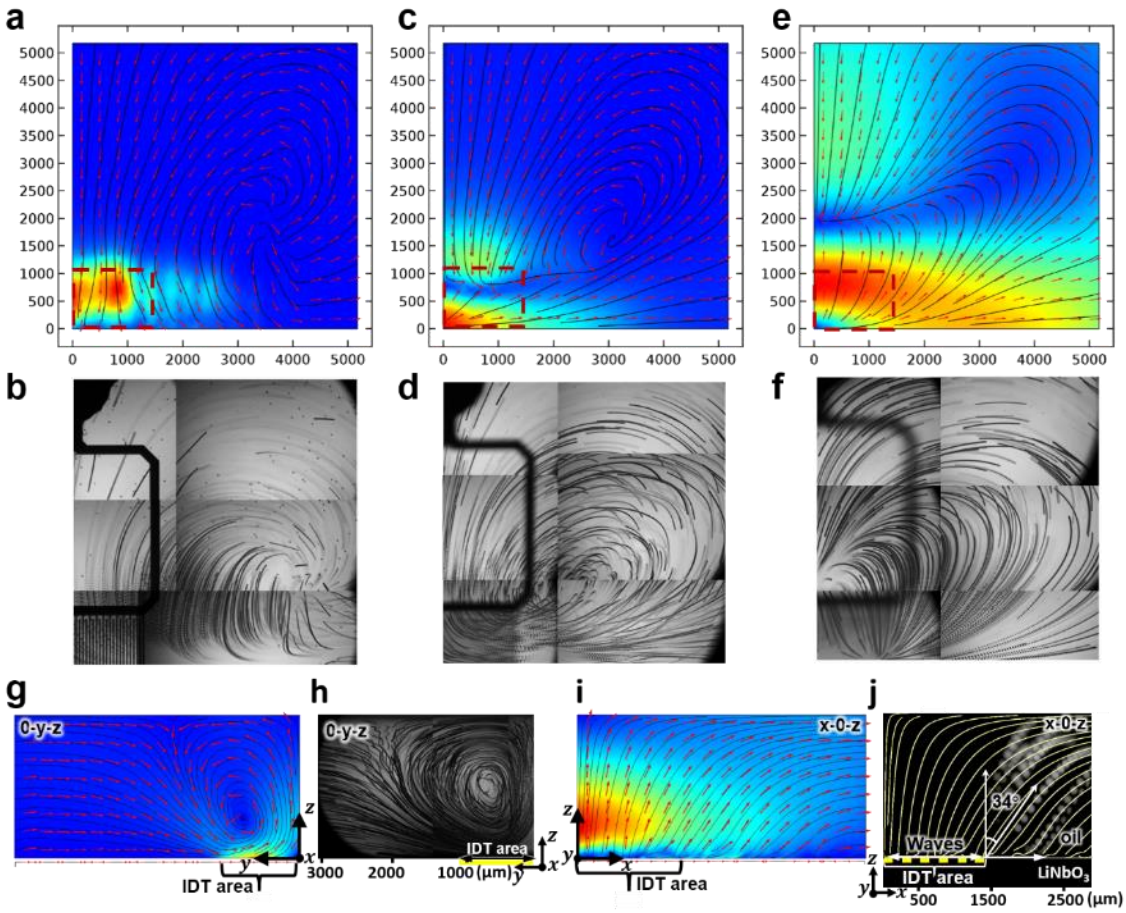

Figure 3.13: Comparison of the numerical and experimental streaming pattern on 2D planes. a-c, Numerical results of the acoustic streaming patterns in the x-y planes at the depths of z=100 μm, z=1000 μm, and z= 2000 μm, respectively. b-f, experimental results of the acoustic streaming patterns in the corresponding x-y planes in (a)-(c). g, h, Numerical and experimental streaming pattern on the 0-y-z plane. A counter flow agrees with the numerical results. i, j, Numerical and experimental streaming pattern on the x-0-z plane.

Experimental streamlines in (j) was visualized using 105-μm fluorescent particles (white dotted lines), which matches with the corresponding numerical streamlines (yellow solid lines). The result shows that the direction of the pumped flow is at an angle of 34° to z-axis.

From the streamlines in the four quadrants, we found that the streamlines were distributed almost symmetrically about both the x-axis and y-axis. The main reason for not having strict symmetric distribution may be the uneven distribution of the tracking beads in the oil. As shown in Figure 3.13a and b, the IDTs pumped the loading oil in the +x and –x directions and created two counter flows in the +y and –y planes, and thereby generated two symmetric stagnation points. With these two points, the object afloat on the oil may have been trapped on either side of the IDTs depending on its initial position. Experiments were carried out to confirm the prediction.

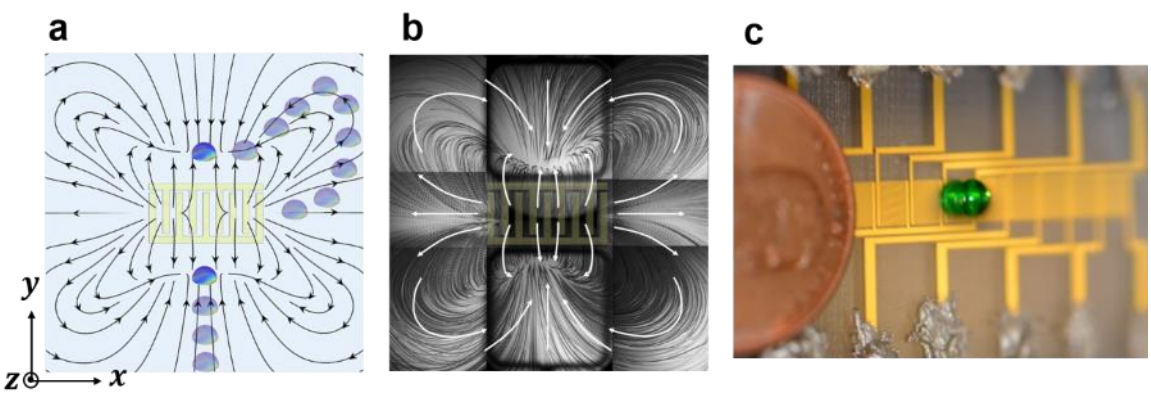

Figure 3.14: Droplet manipulation using the streaming pattern generated by the IDTs merged in the oil. a, Simulated acoustic streaming pattern on the oil-air interface showing two symmetric stagnation points on the two sides of the IDT, where objects floating on the oil would be trapped. Because of the induced acoustic streaming, randomly distributed objects gradually move towards the stagnation points. b, Stacked image showing the streaming pattern on the oil-air interface. The streaming pattern forms the two stagnation points as indicated by two water droplets. The result shows that the streaming in this domain is roughly axial symmetric about both x-axis and y-axis. As such,

a numerical model for this case can be simplified to simulate the area, as depicted by red dashed lines. c, Image of a device with a 1×10 IDT array for contactless droplet manipulation. The green sphere is a drop of dyed water floating on the loading oil.

Device as shown in Figure 3.14c was fabricated for the droplet manipulation based on the streaming pattern in the oil. The IDTs were fabricated using standard lithography. Five nm chromium and 50 nm gold were deposited on a 128° Y-X cut lithium niobate wafer (Precision Micro-Optics, USA) using Semicore (Kurt J. Lesker Co., PA, USA). The IDT fingers had a 45° intersection angle with the X-axis of the material's coordinate system to ensure equal wave speed in two orthogonal directions. Silver epoxy was used to connect the wires with fingers on the wafer. The operation frequency was chosen to be 23.9 MHz, which was the resonant frequency of the IDTs with both finger width and finger interval 37.5 μm. The IDT section was 2,925 μm long and 2,200 μm wide. For the integrated SAW microfluidic device shown in Fig. 1(e), the distance between each IDT was 2.8 mm. A 23.9 MHz sinusoidal AC signal was generated (DG 3012C, Teletronics Technology Corporation, PA, USA), amplified (25A250A, Amplifier Research, USA), and then applied to the IDTs. A relay array (USB24Mx, EasyDAQ, UK) was used to control the power input for individual IDTs. The controlling program was written in Visual C++ (Microsoft Corp., USA). The wafer with IDTs was immersed in a carrier oil of thickness 2,000 μm. Fluorinert FC-70 oil (Hampton Research Corp., CA, USA) was chosen to be the carrier oil due to its inertness and high viscosity (24×10^{-3} Pa·s). Additionally, the density and the speed of sound in the oil were set as 1,940 kg/m^3 and 640 m/s in this work,

respectively. Teflon AF1600 (Dupont Co., DE, USA) was dissolved in the carrier oil to enhance the stability of the droplet trapped in FC-70. The device was mounted on the stage of an inverted microscope (Eclipse TiU, Nikon, Japan). To visualize the streaming pattern, tracking beads of 30 μm were added into the oil. The motion of the tracking beads was recorded by a high-speed camera at a frame rate of 500 frames per second (fps). The trajectories of the tracking beads, which were considered as the streaming lines of the oil domain, were presented by stacking frames of the recorded videos using ImageJ.

3.2.3 Droplet manipulation by the streaming pattern

On the basis of the acoustic streaming velocity distribution on the oil-air surface, we numerically estimated the trajectories of droplets floating on this 2D plane. If considering a tiny particle immersed in the liquid, the drag force, which is proportional to the relative velocity between the particle velocity and streaming velocity, can be simply modeled as Eq. (2.30).

Since the physics behind the relative movement between the droplets and the incompatible liquid is complicated and is not the main target of this work, Eq. (2.30) was used to approximate the drag force of the droplet floating on the loading liquid. In this way, the droplet trajectory was approximated by the COMSOL interface "Particle tracing for fluid flow" and solved by a "Time Dependent" study. 100 water droplets with 5 μL in volume were released from initial positions in a 4×4 mm^2 2D area, as shown in Figure 3.15a. The simulation results show that all of the droplets floating on the oil gradually

concentrated to the trap (Figure 3.15a). From the droplets' trajectories, we found that the droplets at the left side of the domain moved faster towards the trap positions because the drag force at this area was greater.

In an experiment, we measured the trajectories of two droplets (5 μL) released initially at two different positions. One droplet was first released at an initial position as shown in Figure 3.15b; in the presence of the acoustic streaming, it was gradually pushed away from the IDT in the +x direction, then drawn back to the side of IDTs by the backflow, and finally blocked by the counter flow to stop at the "stagnation point." In this case, the device took 3.6 seconds to move the droplet from the initial position to the "stagnation point." Afterwards, the droplet stabilized as shown in the rightmost panel of Figure 3.15b. The results indicate that the droplet stabilized at the "stagnation point" even when the IDTs kept generating streaming in the loading oil. As a comparison, the other droplet was released on the side of the IDT as shown in Figure 3.15c. Since the x-coordinate of the initial droplet position was close to the coordinate at the trap, this droplet was drawn immediately towards the "stagnation point" and only took 0.8 s to stabilize.

Compared with the droplets at the other initial positions, the droplet released at the lateral side of the IDT (the case in Figure 3.15c) had moved less than that released far away from the IDT. Therefore, we chose the lateral side of the IDT, as the initial position for multi-step, contactless droplet manipulation. To optimize the device's design for

subsequent droplet manipulation, we quantitatively characterized the trapping behavior of the device. Figure 3.15d shows the change of trapping positions as a function of oil thickness. The trapping position was defined as the y-coordinate of the trapped droplet center, according to the coordinate system shown in Figure 3.14c. As the oil thickness was increased from 1,000 μm to 3,500 μm, the "stagnation point" for hydrodynamically trapping of droplets moved further from the IDTs, which suggests that the oil thickness should be as thin as possible if the trap is intended to be closer to the IDTs. However, if the oil thickness is too thin, the droplet might attach to and be stuck at the substrate since the droplet immerses partly in the oil. Through the experimental characterization, 2,000 μm was found to be the optimal oil thickness for the device used in this work.

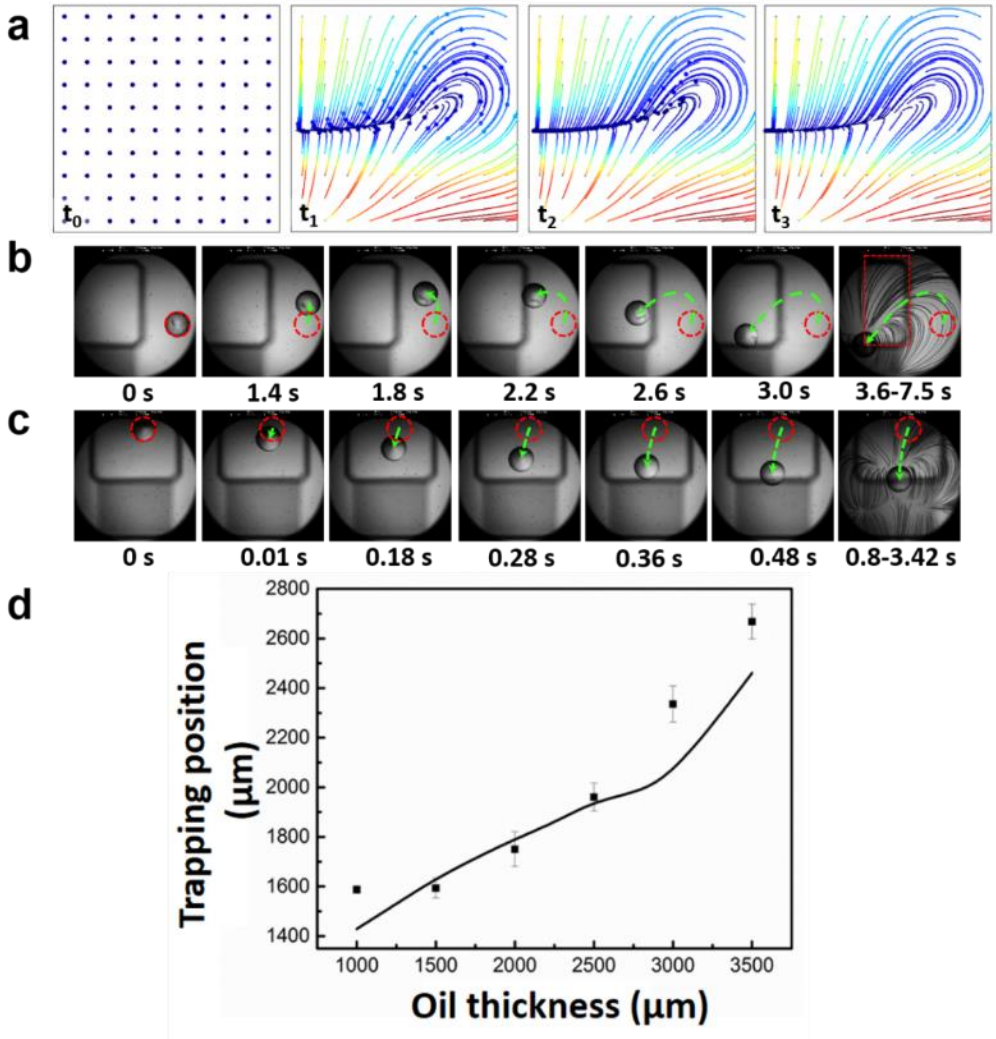

Figure 3.15: Droplet tracing in our SAW microfluidic device. a, Numerical results showing droplets' trajectories over time driven by the 2D streaming pattern in the x-y-2000 µm plane shown in Figure 3.12b. Each dot represents the center of a droplet, and their initial positions are indicated as shown in Figure 3.15a-t_0. The results show that all the droplets moved towards the trap in the presence of the streaming. Experimental images show the trajectory of a droplet released (b) at the right side of the IDT and (c) at the top side of the IDT. The red dashed circles indicate the initial positions in each case and the green lines indicate the trajectories of the droplet from the initial position to the position shown on each figure. d, Plot showing the dependence of the trapping position (stagnation point) on the oil thickness measured by experiment (spots and error bars) and simulation (line). The position is defined by the distance from the droplet center to the IDT center.

Since each IDT can create two symmetric "stagnation points" as hydrodynamic traps for droplet manipulation, a well-designed IDT array could contain multiple traps. As shown in Figure 3.14c, we designed a device where the IDTs were arranged as a 1×10 array on a 128°Y-X cut $LiNbO_3$ wafer. The IDT fingers were inclined at 45° relative to the X-axis of the material's coordinates. The red arrows in Figure 3.16 indicate that the IDTs were being activated in every step. By activating the IDT following the order as shown in Figure 3.16, we moved the green droplet up and down on the oil surface, which demonstrates on-demand droplet manipulation. The result shows that our device moves droplets on the oil surface in a controllable manner by alternating the IDTs in an array in a given order. This movement will enable various biological and biomedical applications where on-demand liquid handling is necessary.

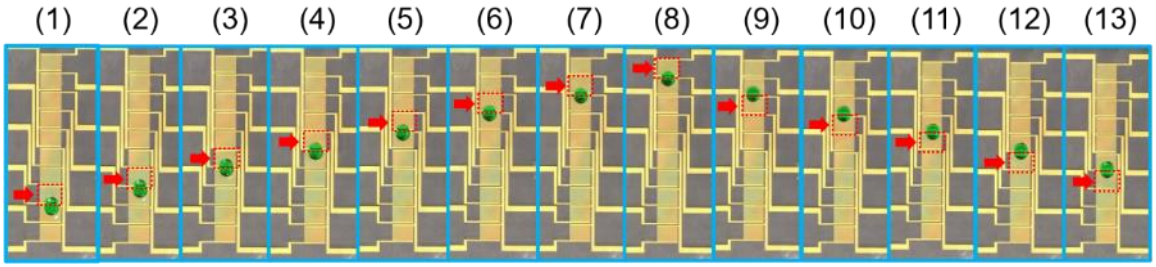

Figure 3.16: Droplet manipulation achieved using a SAW microfluidic device with 1×10 IDT arrays. The red arrows and dotted boxes point out the single IDT that is being activated to manipulate the green droplet in every step. Depending on its initial position, the green droplet will be trapped at either side of the activated IDT closer to the droplet.

3.2.4 Discussion and conclusion

In this section, we developed a "slip velocity method" which performs 3D analysis in SAW microfluidics and significantly reduces the computation time of the 3D acoustic

field solution. In particular, we solved the 1st-order and 2nd-order equations in the viscous boundary layer with the substrate displacement solved together as the actuation at the solid-liquid boundary. The 2nd-order velocity on the top of the boundary layer was captured as the "slip velocity" which was used as an actuation to calculate the outer streaming. Experiments showed acoustic streaming on several typical planes to verify the simulation results. It was found that the prediction of the simulation agreed with the experimental results. Further, we discussed the effects of some parameters on the trapping velocity and trap position based on the simulation and experimental results. On the strength of these findings, we fabricated a SAW microfluidic device with integrated IDT arrays to demonstrate stable, contactless droplet manipulation.

Besides the acoustic streaming in the oil, we also discovered streaming motion inside the droplet due to the relative movement of the loading oil and droplet. This discovery indicates that this non-contact droplet handling system has potential for on-chip sample handling. After reaching the "stagnation point," the droplet stops moving but the oil still streams. The oil flows below the droplet and drives the streaming inside the droplet. The shape and immersion depth of the droplet depends on many factors, such as the surface tension at the droplet interface, the size of the droplet, and the original vertical distance between the position of the droplet to the oil-air interface.

3.3 Vortex streaming generated in spinning droplet

3.3.1 Motivation

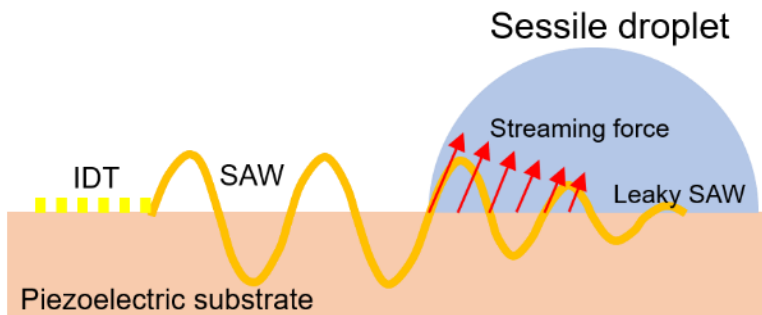

Figure 3.17: Schematic illustration of acoustic streaming in sessile droplet generated by SAW. The SAW propagates on the piezoelectric substrate and leaks into the liquid droplet. The propagation of the leaky SAW generates a streaming force and induces acoustic streaming in the sessile droplet.

The SAW-driven fluid motion in the sessile droplet has been explored for various biological applications. Figure 3.17 shows a classic setup of a SAW-driven droplet device. The SAW propagates into the liquid droplet and produces a streaming force that induces fluid motion in the medium. By increasing the applied RF power to the IDT, the fluid motion of acoustic streaming (Strobl, Schneider, Wixforth, Sritharan, & Guttenberg, 2006; Tseng, Lin, Sung, Chen, & Lee, 2006), droplet movement (Sano, Matsui, & Shiokawa, 1998), fluid jetting, and atomization (Chono, Shimizu, Matsui, Kondoh, & Shiokawa, 2004; Murochi, Sugimoto, Matsui, & Kondoh, 2007) could be induced (Friend & Yeo, 2011).

The vortex streaming pattern can be applied to liquid mixing and particle concentration applications. As shown in Figure 3.18, the SAW beams that enter the droplet from its flanks can generate acoustic vortex streaming pattern in the droplet. The

simulation was performed based on the theoretical model stated in Section 2.2.2. As the width of the SAW beam increases, the center of the vortex moves to the geometric center of the droplet on the x-y planes. By applying two SAW beams into the droplet at the two flanks from the opposite view, the streaming velocity becomes more uniform radially.

In this section, we developed a droplet acoustofluidic device with a PDMS ring that can confine the location of the droplet and a pair of slanted IDTs that can generate two SAW beams at the two flanks of the droplets. Compared with the traditional setup of droplet acoustofluidic device, the ring confinement increases the RF power threshold between the acoustic streaming and droplet movement motion. In this way, higher streaming velocity can be generated in the droplet while the droplet stays in its original location. Moreover, droplet spinning motion was also observed in the SAW-driven droplet confined by the PDMS ring. Combing the acoustic streaming and the spinning motion, the nanoparticles in the droplet can be efficiently concentrated to the middle of the droplet. Based on this mechanism, we developed an acoustofluidic centrifuge (AFC) system for nanoparticle separation and transport.

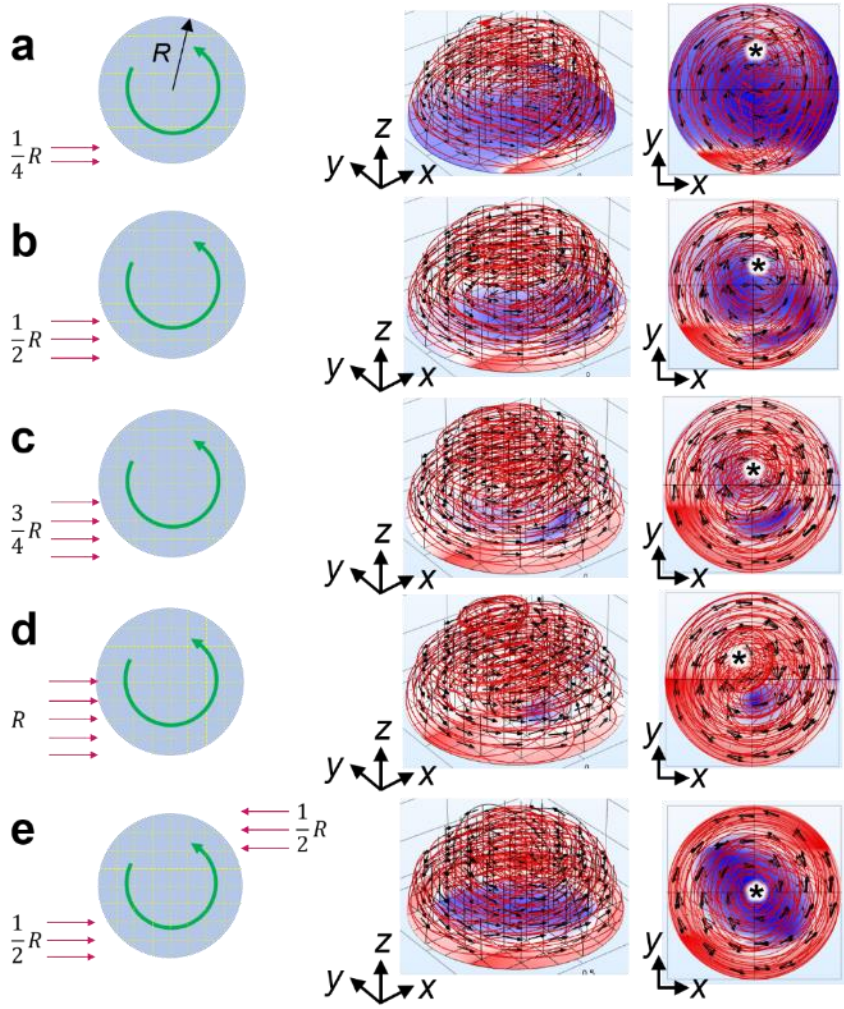

Figure 3.18: Simulation results of the acoustic streaming pattern in the sessile droplet (radius: R) activated by SAW beams with different width. a-d, Acoustic streaming pattern activated by a SAW beam with the width of $\frac{1}{4}$R, $\frac{1}{2}$R, $\frac{3}{4}$R, and R, respectively. e, Acoustic pattern activated by two SAW beams propagating from opposite directions into the two flanks of the droplet. The width of the beams is $\frac{1}{2}$R.

3.3.2 SAW-induced fluid motion in the spinning droplet

The device configuration is shown in Figure 3.19. The AFC system contains a pair of IDTs and a PDMS ring placed in the middle in between the IDTs. A droplet was loaded in the PDMS ring. Originally, the bottom of the droplet was confined by the ring, and the

water-air interface of the droplet was in an equilibrium hemispherical shape which was determined by the combing effect of gravity, surface tension, and boundary alignment. When applied AC signals to the IDTs, two travelling SAW beams propagate in +y and -y directions are generated at the two symmetric flanks of the droplet. When the SAW beams were first generated, the droplet slightly oscillated and the acoustic streaming was detected in the droplet. Then, the angular momentum accumulated in the liquid medium, and the droplet started to spin. Observed from the side-view, the SAWs propagated into the liquid droplet, and the droplet was deformed into a half-ellipsoid-like shape that starts to spin (Figure 3.20).

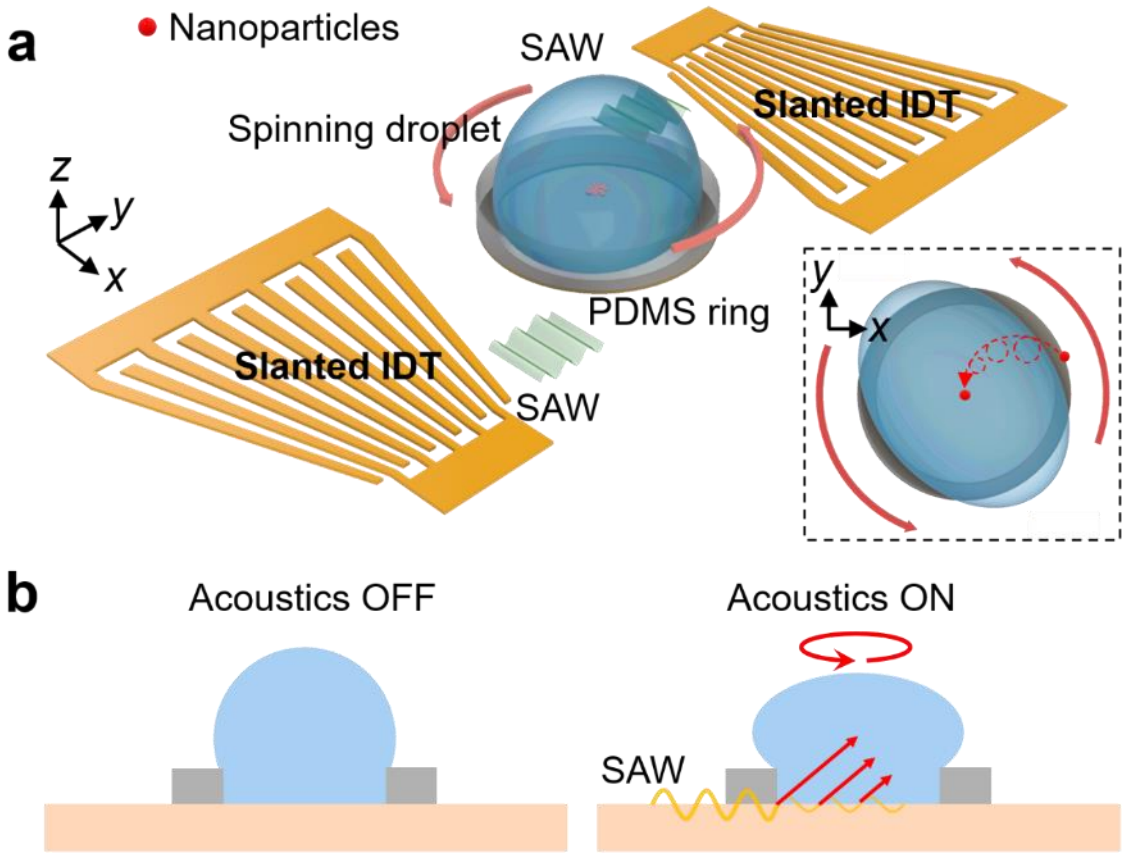

Figure 3.19: Schematic illustration of the acoustofluidic centrifuge (AFC) system. a, The setup of the AFC system contains two slanted IDT and a droplet located in the middle of the two IDTs and confined by a thin PDMS ring. The IDTs generate two SAW beams at the two flanks of the droplet. When the SAW beams leak into the droplet, the reflection of the leaky SAWs deforms the liquid-air interface of the droplet, and induces a periodic deformation in the droplet, which performs as the motion of droplet spinning. The particles in the droplet can be concentrated to the middle of the droplet efficiently. b, Side-view illustration of the droplet status when acoustics is off and on. When the acoustics is off, the droplet stays in its equilibrium status. When the SAWs propagates into the liquid droplet, the droplet deformed into a half-ellipsoid-like shape and starts spinning.

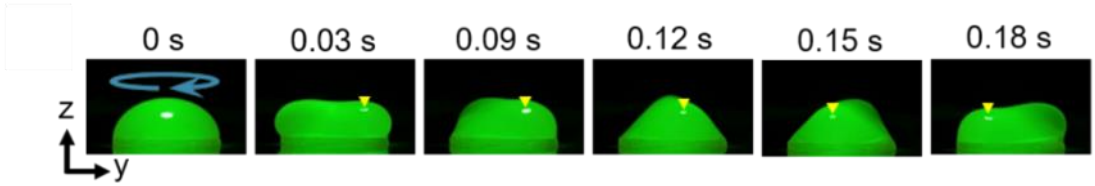

Figure 3.20: Image sequence of the droplet spinning motion taken from the side view. The AC signal was applied at 0s to activate the droplet spin motion. During the spin, the droplet was stretched to a half-ellipsoid-like shape from its original hemispheroid-like shape. The yellow arrow heads indicate a reference observation point that moves together with the spinning droplet. (Gu et al., 2021)

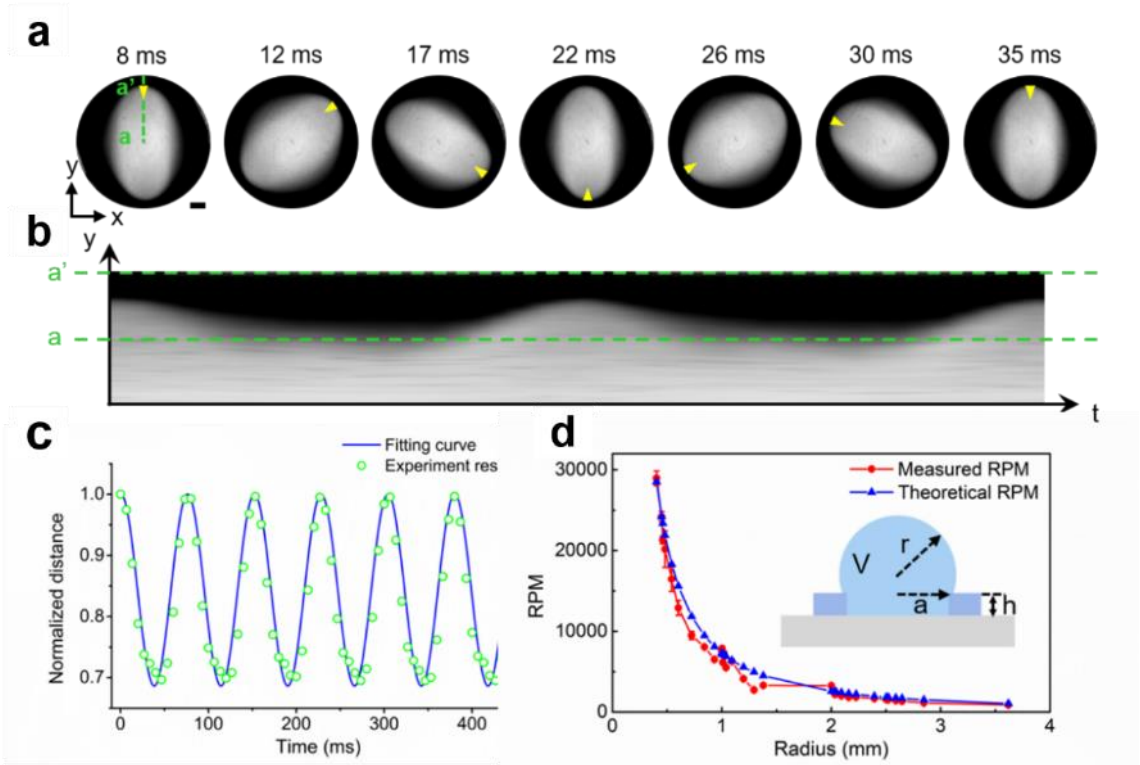

Figure 3.21: Measurement of the period of the droplet spinning motion. a, Image sequence showing a period of droplet spinning. The images were taken under the microscope from the top view. b, Stack of the image sections at the a-a' lines along the time to measure the period of the spinning motion. c, The variation of the length of the light area in the a-a' lines extracted from (b) reflects the period of the droplet spinning motion. d, The variation of the spinning period (RPM: rotation per minute) with the increase of the droplet radius. The variation was calculated theoretically and measured experimentally. (V: the volume of the liquid within the region upon the PDMS ring; r: the radius of the droplet; a: the radius of the PDMS ring.) (Gu et al., 2021)

Unlike the rotation of a solid body, the droplet spinning motion is essentially a periodic deformation of the fluid domain. The speed and period of the spinning motion

was measured as shown in Figure 3.21. First, the image sequence taken from the top view shows the droplet shape at each time step. Then, the image sections at the a-a' lines in each figure were stacked along the time. The variation of the length of the light area in the a-a' lines extracted from Figure 3.21b reveals the period of the droplet spinning motion as shown in Figure 3.21c. The spinning speed can be acquired and further transformed to the value of RPM by compiling the Fourier transform of the wavefront. We also measured the RPM for droplet with various radius and compared the experimental results with the classic droplet oscillation model:

$$\omega_n{}^2 = n(n+1)(n-1)(n+2)\frac{\sigma}{r^3\left[(n+1)\rho_{liquid} + n\rho_{air}\right]} \tag{3.3}$$

in which r is the radius of the droplet, σ and ρ_{liquid} are the surface tension and density of the liquid, and ρ_{air} is the density of the air. The "n" indicates the spherical harmonic degree which corresponds to the lobe number during the droplet spin. The radius of the droplet can be acquired based on the equation,

$$V - \pi a^2 h = \frac{\pi}{3}\left(r + \sqrt{r^2 - a^2}\right)^2 \left[3r - \left(r + \sqrt{r^2 - a^2}\right)\right] \tag{3.4}$$

where a is the radius of the PDMS ring, h is the height of the PDMS ring, and V is the total volume of the droplet. Although this equation was originally generated to describe the free oscillation of the spherical mutation, this fitting may be due to the similarity between the droplet rotation and the standard oscillatory motion: the confinement of the surface tension.

3.3.3 Particle concentration in the spinning droplet

Understanding the spinning motion of the ring-confined droplet, in this subsection, we explored the particle movement (1-μm in diameter) within the spinning droplet. The particle trajectories were acquired by stacking the image sequence of the recorded video of the particle movement. Figure 3.22 compares the particle trajectories in the same droplet with and without spinning motion. Within a SAW-driven droplet without spinning motion (low power applied), the particles were directed to the center of the droplet following the trajectory of a convergent vortex. The particles were driven mainly by the drag force, acoustic radiation force, and shear induced migration in the fluid system. When the droplet spinning was activated by SAW beams, the particles were efficiently directed to the middle of the droplet following helical-shaped trajectories, while the overall moving tendency is similar to the one in the non-spinning droplet. This particle trajectory is similar to the Stoke drift effect on the moving water-air interface. Besides the 1-μm particles, the spinning droplet can also concentrate particles with the size down to 28 nm.

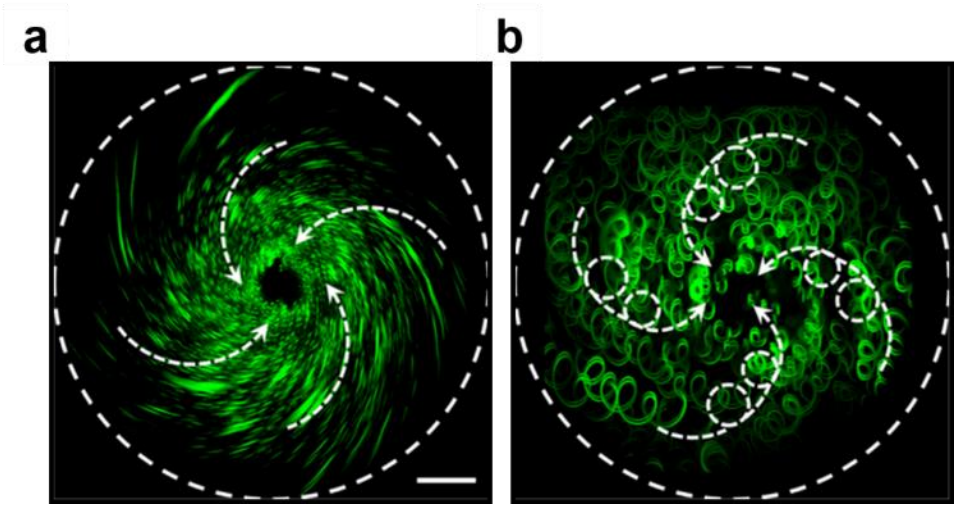

Figure 3.22: Stacked particle trajectories showing the flow pattern in (a) a droplet without spin motion and (b) a droplet with spinning motion. (Gu et al., 2021)

We performed numerical simulation to analyze the mechanism of particle concentration in the spinning droplet. In the spinning droplet, the total force on the particle can be separated into a tangential and a radial component. The acoustic radiation force and the shear induced migration contribute partially to the radial force component and can direct the particles to the middle of the droplet. These forces dominant the movement of the particles in the micrometer scale. However, for the particles in the nanometer scale, the drag force induced by the fluid flow is much larger than the acoustic radiation force and the shear induced immigration (Table 3.2). Thus, the role of the acoustic waves in the AFC for nanoparticle concentration lies more in driving the acoustic streaming and spinning motion of the droplet, instead of particle movement. The concentration of the nanoparticles in the spinning droplet is dominated by the drag force.

Figure 3.23a shows the droplet at a certain time-point during the spinning. The droplet was compressed from ±i directions and stretched from ±j directions which is near perpendicular to the i direction. The spatial location of this compress-stretch deformation shifts rotationally and for the spin of the droplet. Here, we simulated the particle movement in a rectangular fluid section in the center of the droplet. The velocity profile was applied to the two sides of the droplet to simulate the continuous fluid compressing and stretching during the droplet spinning. Specifically, the velocity profile was set to $\pm Acos(4\pi ft)$ using the "velocity" boundary condition (A: amplitude of the periodic velocity profile; f: the frequency of the spin motion). The top and bottom of the fluid domain was set to the boundary condition of "no pressure". As shown in Figure 3.23 c and d, although the particles move back and forth with respect to the center of the domain, the accumulating effect generated by the periodic fluid compressing and stretching directed the particles to the center of the droplet. The results of this numerical studies indicate that the flow velocity component generated by the continuous compressing-stretching fluid motion in the droplet contributes to the radial force that drive nanoparticle concentration in the spinning droplet.

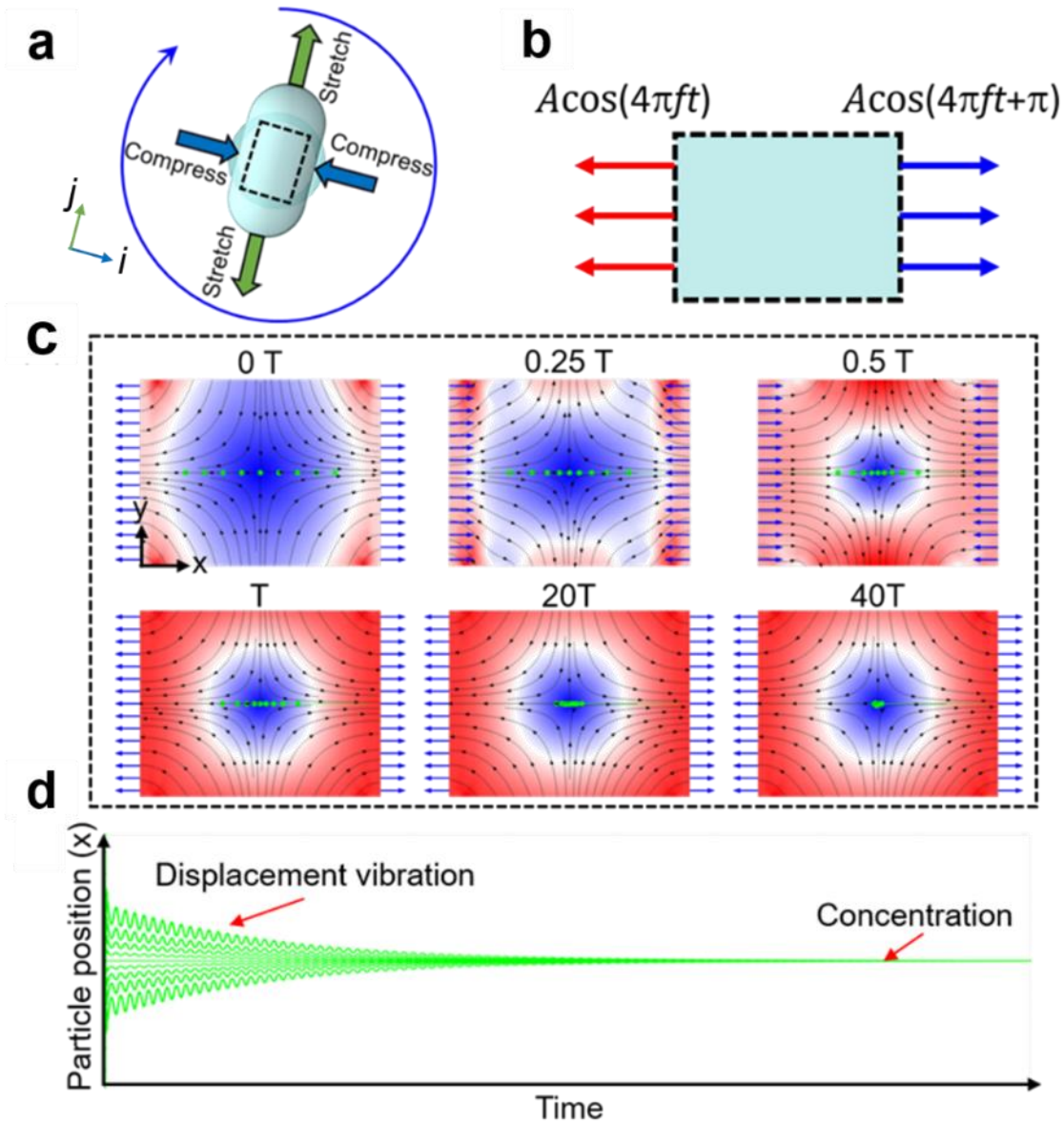

Figure 3.23: Numerical simulation results analyzing the mechanism of the particle concentration in the AFC system. a, Schematic illustration of the deformation in the spinning droplet. The droplet was compressed from ±i directions and stretched from ±j directions which is near perpendicular to the i direction. b, The simulation domain, which is a small area in the middle of the droplet, and the boundary conditions. c, The movement of the particles in a spinning period. The particles were gradually moved to the center of the droplet. d, The variation with time of the distance between the particle location and

the droplet center. The distance fluctuates and gradually reduces to zero. This indicates that the particle moves to the center of the droplet. (Gu et al., 2021)

Table 3.2: Essential forces in the spinning droplet that effect the particle movement. (Gu et al., 2021)

Force	**Force magnitude (N)***	**Force direction**	**Formula** (Gor'kov, n.d.; Karimi & Akdogan, 2012; Martel & Toner, 2014; Yilmaz & Gundogdu, 2009)
Drag force (vortex streaming)	~0-10^{-10}	Tangential	$\boldsymbol{F}_H = \frac{3\mu C_D Re_r m_p}{4\rho_p {d_p}^2}\boldsymbol{v_T}$
Secondary-flow drag force (droplet deformation)	~0-10^{-11}	Radial	$\boldsymbol{F}_H = \frac{3\mu C_D Re_r m_p}{4\rho_p {d_p}^2}\boldsymbol{v}_R$ $\boldsymbol{v}_R = \frac{\boldsymbol{dR}_{droplet}}{\boldsymbol{dt}}$ $\boldsymbol{R}_{droplet} = (R_{max} - R_{min})\sin(2\pi(2f_{spin})t) + R_{min}$
Pressure gradient force (tangential)	~0-10^{-17}	Tangential	$\boldsymbol{F}_p = \frac{1}{6}\pi d_p^3 \rho \frac{D\boldsymbol{u_T}}{Dt}$
Pressure gradient force (radial)	~0-10^{-17}	Radial	$\boldsymbol{F}_p = \frac{1}{6}\pi d_p^3 \rho \frac{D\boldsymbol{u_R}}{Dt}$
Acoustic radiation force	~0-10^{-15}	Partially radial	$\boldsymbol{F}_{rad} = -\nabla\{V_p[\frac{f_1}{2\rho_0 {c_0}^2} < {p_1}^2 > - \frac{3\rho_0 f_2}{4} < \boldsymbol{v_1} \cdot \boldsymbol{v_1} >]\}$

* The forces calculated for the case with a droplet volume of 10 μL (1.29 mm in radius); droplet spinning with the speed of 55 fps; particles with 100 nm in diameter; acoustic waves with the frequency of 21.7 MHz and pressure amplitude of 300~800 kPa.

Understanding this working mechanism, we performed another numerical study to analyze the particle trajectories in the spinning droplet using COMSOL Multiphysics 5.4 (the COMSOL group). A 2D numerical models (on the horizontal cross-section) were set up to solve the particle tracing in the droplet domain with pre-defined deformation as

shown in Figure 3.24b. The shape of the domain was set to a quasi-ellipse with major semiaxis of R_a and minor semiaxis of R_b. First, a "Laminar Flow" interface was applied to solve the streaming velocity activated by the streaming force shown in Eq. (3.6) based on governing equation Eqs. (2.22) and (2.23):

$$F_x = 0 \tag{3.6a}$$

$$F_y = -(1+\alpha_1^2)A_m^2\omega^2 k_i e^{[2(k_i y+\alpha_1 k_i z)]} \tag{3.6b}$$

$$F_z = -(1+\alpha_1^2)A_m^2\omega^2 k_i \alpha_1 e^{[2(k_i y+\alpha_1 k_i z)]} \tag{3.6c}$$

where A_m is the amplitude of substrate vibration, k_L is the wave number of the leaky SAW, and $\alpha = i\alpha_1$ is the attenuation coefficient, respectively. The spinning motion of the droplet was modelled by applying a "Rotating Domain" condition in the "Moving Mesh" interface. The rotation speed of the domain was set to f_r revolutions per second. The value of f_r within the range of 0-55 rps were applied based on the experimental measured value for the droplet with the same volume. The "Laminar Flow" and the "Rotating Domain" interfaces were solved together using a time-dependent solver to simulate the flow field activated by two leaky-SAWs beams. A "particle tracing for fluid flow" interface was applied to analyze particle motion in the spinning droplet driven by the forces discussed above. A "Particle properties" condition was used to set the density and diameter of each species of the particles. Here, we studied the trajectories of the polystyrene (PS) particles (density: 1,050 kg/m^3) with the diameter of 28 nm, 100 nm, or 1 μm. The particles were randomly released at t=0 s using a "Release" condition, or regularly released at the determined positions at t=0 s using a "Release from Grid" condition. The movement of

the particle is governed by Eq. (2.31). We mainly considered two external forces ($\boldsymbol{F_t}$), which are the acoustic radiation force and secondary-flow drag force. A "Drag Force" condition was added to apply the component of drag force induced by the flow velocity induced by the leaky-SAW beam propagation and droplet spinning motion ($\boldsymbol{u}$). A "Force" condition was used to add the total radial force components, which contains acoustic radiation force and another component of drag force induced by the periodic compressing-stretching of the liquid. The value of this radial force was adjusted in the ranged from 0 N to 10^{-10} N for different cases. These physical systems were solved using a time-dependent solver simultaneously with a step of 0.0001 s for 1 μm particles, and 0.000005 s for 28 nm and 100 nm particles. The simulation results in Figure 3.24 and Figure 3.25 shows that the 100-nm particles can be directed into the bottom center of the droplet while the 2-28-nm particles staying in the periphery. Thus, the AFC can be applied to separate nanoparticles based on the difference in their size.

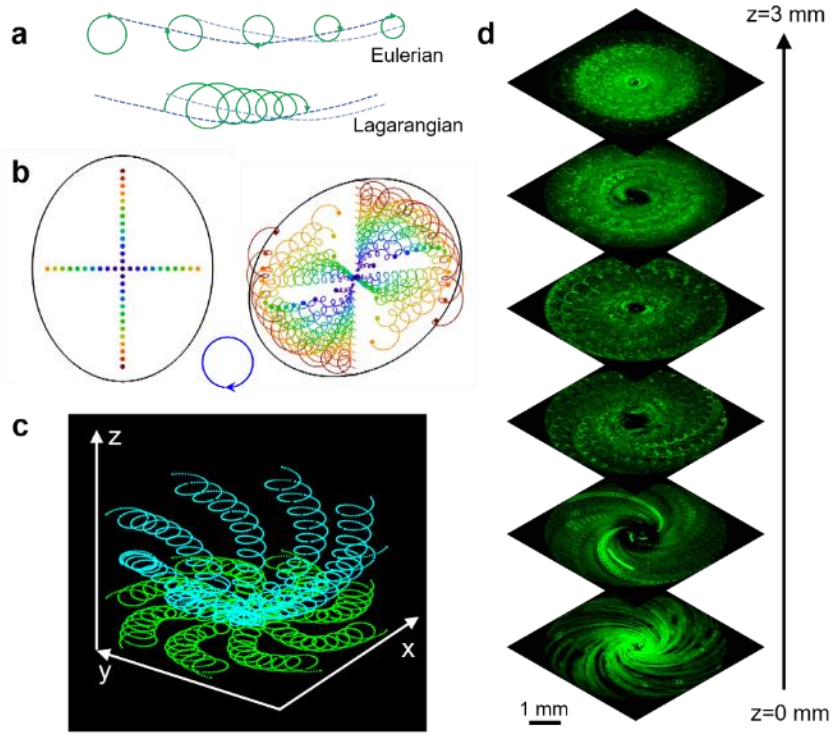

Figure 3.24: Particle movement in the spinning droplet. a, Schematic illustration of the Eulerian and Lagarangian description of particle movement. b, Simulation results of the 2D particle trajectories. c, Simulation results of the 3D particle trajectories. d, Stacked particle trajectories in the horizontal planes at different depth.

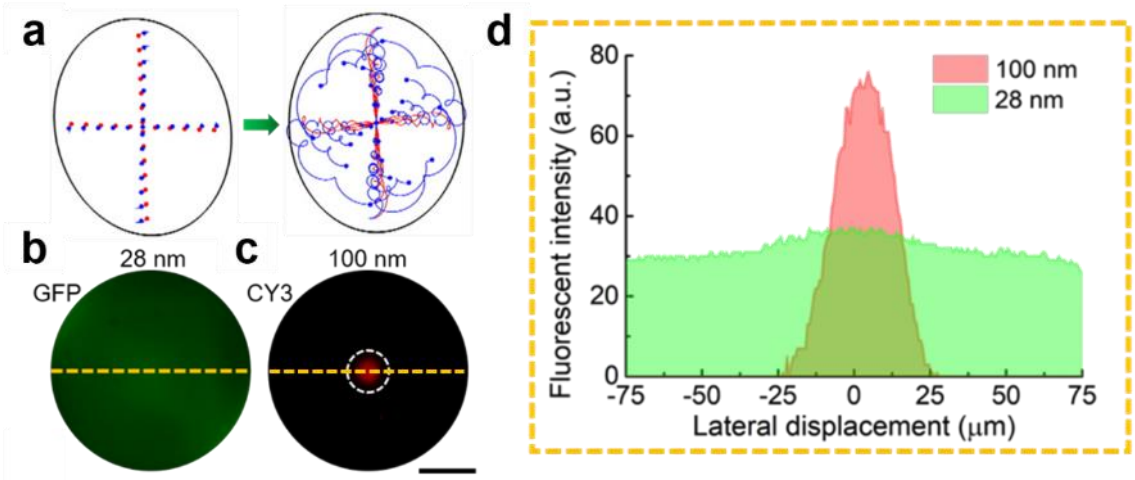

Figure 3.25: Separation of the 28-nm particles and 100-nm particles using the AFC system. a, Numerically simulated trajectories of the 28-nm (blue) and 100-nm (red)

particles. The 100-nm particles concentrated to the center of the droplet. b, Fluorescent microscopic images of the experimentally measured distribution of the 28-nm particles (GFP) and 100-nm particles (CY3) after using the AFC. Scale bar: 100 μm. c, The intensity of the GFP and CY3 fluorescence along the orange dashed lines in (b), which indicates the concentration of the 28-nm and 100-nm particles, respectively. (Gu et al., 2021)

3.3.4 Nanoparticle isolation using the ARC

The studies in the previous sections proved that the larger particles will be concentrated to the center of the spinning droplet efficiently, while the smaller droplets keep random distribution in the periphery. To benefit the research that requires downstream analysis of sample containing certain species of particles, we developed the dual-droplet ARC to isolate different nanoparticle species into different droplets. As shown in Figure 3.26a, we designed a microfluidic channel in which two top-opened PDMS rings are connected by a microfluidic channel. Theoretically, the two droplets confined by the two rings simultaneously by two sets of SAW beams propagate in opposite directions at the flanks of the droplets. Here, we used a frequency shift keying function to excited four SAW beams with frequencies of 21.7MHz (f_1), 20.3 MHz (f_2), 15.7 MHz (f_3), and 15.3 MHz (f_4), respectively. Two sets of function generators and amplifiers were used to generate SAW beams with f_2 and f_4 for the spinning of the right droplet, and to generate SAW beams with f_1 and f_3 for the spinning of the left droplet. In each set of the equipment, the two frequencies were shifting between the two values to alternately activate the two SAW beams. Noting that the response of the fluid motion has a relaxation time to the SAW beam excitation, the shifting rate of the two frequencies should be

sufficiently high to keep the desired flow motion in both of the droplets. The shifting rate was set to 100kHz in this study. As shown in Figure 3.26b, the right droplet (volume: 4 μL, spinning speed: 6867 ± 160 rpm) originally contains 28-nm and 100-nm particles which evenly distributed in the droplet. The left droplet was originally a PBS droplet with the volume of 5 μL and calculated to be spinning with the speed of 5674 ± 98 rpm. By activating the four SAW beams, the 28-nm nano particles can be transported from the right droplet to the left droplet due to the rotation speed difference in the two droplets. Finally, the 100-nm and 28-nm particles were concentrated in the right and left droplets, respectively. Samples can be collected by inserting capillaries into the two droplets solely.

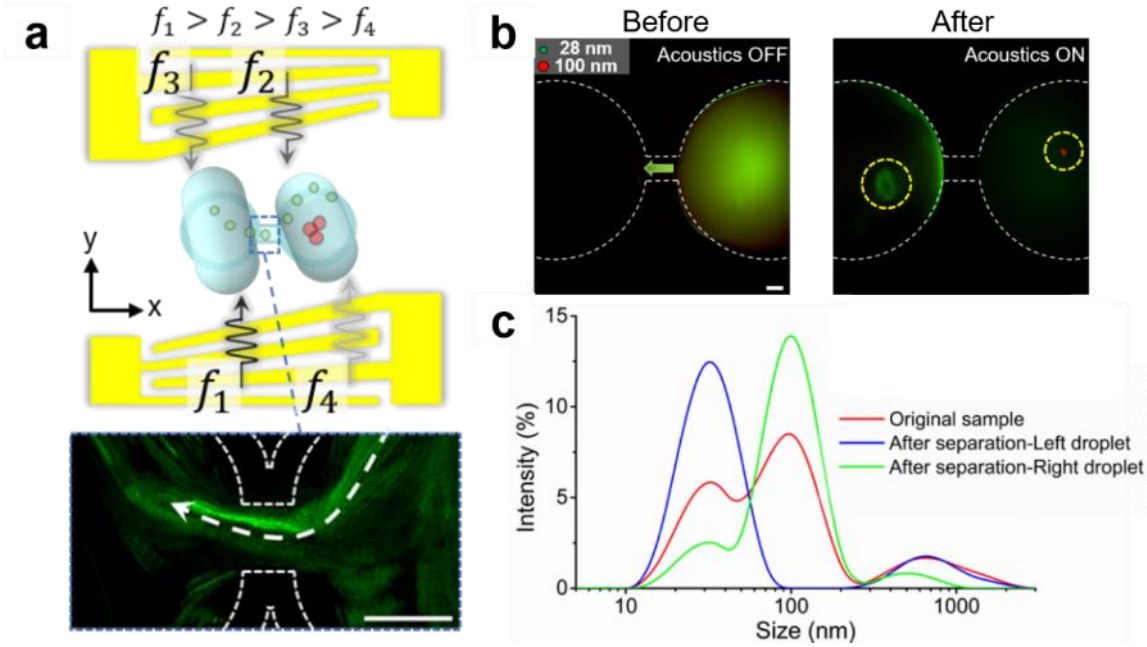

Figure 3.26: Nanoparticle separation and transportation using the AFC system with two ring-confined droplets connected by a microchannel. a, Schematic illustration of the dual-droplet AFC system, which contains two slanted IDTs and a microfluidic channel connecting the two ring-confined droplets. The four SAWs beams were activated with AC signals with the frequencies of 21.7MHz (f_1), 20.3 MHz (f_2), 15.7 MHz (f_3), and 15.3 MHz

(f_4). The spinning motion were activated in the two droplets simultaneously. The particles are loaded in the right droplet at the beginning. The larger particles are concentrated in the center of the right droplet while the smaller particles are transported to the left droplet through the microchannel. b, Fluorescent microscopic images before and after turning on the acoustic signals. c, Distribution of the particle size in the original liquid sample, processed in the left droplet, and processed liquid in the right droplet. The two peaks around 28-nm and 100-nm in the curve of the original sample indicated that the original sample contains these two species of particles. After the transportation, the curves of the left droplet and the right droplet shows only peak at 28-nm and 100-nm, respectively. This indicates that the 28-nm particles are transported to the left droplet. Scale bar: 200 μm. (Gu et al., 2021)

We performed the simulation using COMSOL Multiphysics 5.4 (the COMSOL group) to verify the streaming pattern in the fluid system. The simulation was performed based on the theoretical model in Section 2.2.2. A predefined "laminar flow" interface was used to solve the governing equations (Eqs. (2.22) and (2.23). The body force in Eqs. (3.27) was applied by adding a "volume force" condition. The boundary conditions on the water-solid interfaces were set to "no slip" ($\boldsymbol{u} = \boldsymbol{0}$), which confines the velocity on the PDMS wall and substrate to be zero. And the boundary condition on the droplet-air interface was set to "slip" ($\boldsymbol{u} \cdot \boldsymbol{n} = 0$; $\boldsymbol{K_n} - (\boldsymbol{K_n} \cdot \boldsymbol{n})\boldsymbol{n} = \boldsymbol{0}$, where $\boldsymbol{K_n} = \mu(\nabla \boldsymbol{v} + (\nabla \boldsymbol{v})^T)\boldsymbol{n}$), which prescribes a no-penetration condition and assumes no viscous effects at the slip wall. The physics was solved *via* the COMSOL "stationary" solver.

As shown in Figure 3.27, the streaming velocity in the right droplet is smaller than that in the left droplet. The solvent in the periphery of the right droplet can be transported from the microchannel to the left droplet and be further concentrated in the left droplet.

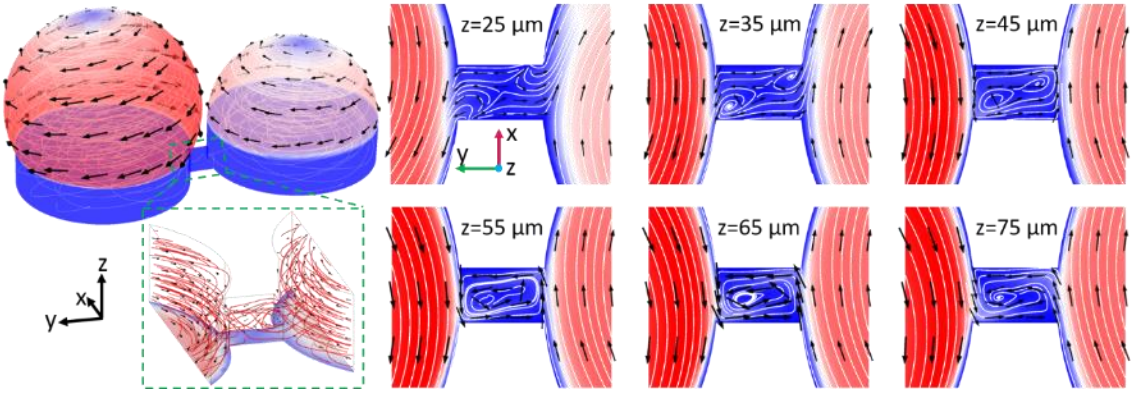

Figure 3.27: Numerical simulation to explore the flow pattern in the microchannel.

Exosomes are well-knowing nano vesicles produced by cells with molecular cargos, which carries information for disease diagnosis and health evaluation. It has been reported that exosomes have three subpopulations distinguished based on their size: (1) large exosomes with the size of 90-150 nm, (2) small exosomes the size of 60-80 nm, and (3) exomeres with the size of about 35 nm. The exomeres are nanoparticles without membrane. This smallest subpopulation of exosome carries distinctive cargos that do not exist in other two subpopulations. Thus, obtaining the exomeres is meaningful for biomedical researches.

With the dual-droplet ARC (Figure 3.26a), we can isolate the exomeres with other subpopulations of exosomes. The components in the original and processed samples were analyzed by (nanoparticle tracking analysis) NTA and TEM imaging. As shown in Figure 3.28a, large exosomes, small exosomes, and exomeres were detected in the original sample loaded to the right droplet. After the process of the AFC, only large exosomes and small exosomes were detected in the processed sample in the right

droplet (Figure 3.28b). Meanwhile, after the AFC process, the left droplet which is pure PBS originally, was detected to contain particles with diameters below 50 nm (Figure 3.28c). These results indicate that the exomeres were transported from the right droplet to the left droplet while other subpopulations of exosome stayed in the right droplet. Thus, the ARC can be applied for biomedical researches that require the extraction of exomeres.

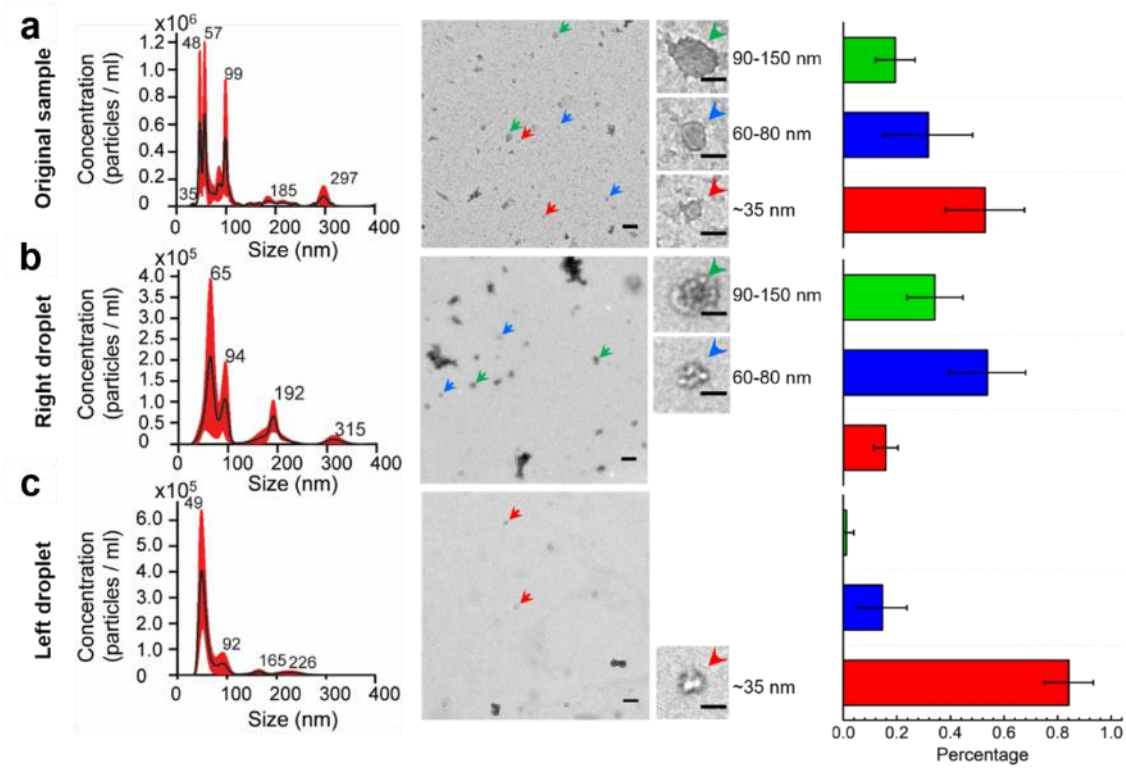

Figure 3.28: Separation and transport of the exosome subpopulations using the AFC. The first, second, and third columns of figure components are the particle size distribution analyzed using NTA, the TEM images of the sample (Scale bar: TEM image: 200 nm. Insets: 50 nm.), and particle size distribution measured based on the TEM images, respectively. a-c, Data of the original sample, processed sample in the right droplet, and processed sample in the left droplet, respectively. (Gu et al., 2021)

3.3.5 Discussion and conclusion

In summary, we analyzed the SAW-induced fluid motion in a ring-confined droplet in this section. Then we developed an acoustofluidic centrifuge (AFC) system which can achieve nanoparticle concentration, separation, and transportation. The system consists of a pair of slanted IDTs which can generate SAW beam inserts to the droplets from opposite directions at their flanks. The spinning motion of the droplet exerts additional radial force to accelerate the particle concentration effects. We applied AFC to separate the exomeres from the exosome samples. Thus, the AFC can be applied to multiple biomedical applications in which the analysis on exomeres is required.

In future research, droplet arrays with specific configurations and connections can be developed to hande samples with more complex components.

3.4 Summary

In this Chapter, we analyzed the acoustic vortex streaming pattern generated by SAWs in two unique acoustofluidic devices. The acoustic vortex streaming generated by the IDTs merged in the oil can be applied to handling liquid droplets floating on the oil. Also, the spinning droplet can achieve isolation of nanoparticles based on the difference on their size. All these devices can perform versatile manipulation for liquid/particle processing in biotechnological applications.

4. Zebrafish Phenotyping Using Acoustofluidic Rotational Tweezing Platform

In this chapter, we present an acoustofluidic rotational tweezing (ART) device which uses surface acoustic waves to generate polarized acoustic streaming with a single vortex tube pattern. The dimension of this single vortex tube is scalable by designing the IDT and channel configuration. And the single vortex tube enables the stable rotational manipulation of a zebrafish larvae in the microfluidic channel. This function allows imaging zebrafish samples from multiple viewpoints, 3D models reconstruction based on the multi-view image sequence, and morphological properties quantification for the phenotyping studies in a various of fields (*e.g.*, drug development and chemical screening). Sections 4.1 introduces the motivation of the development of this platform. Section 4.2 presents the device design and working principle of generating polarized acoustic streaming with a single vortex tube pattern. Section 4.3 describe the fabrication of the device. Section 4.4 and Section 4.5 describe the experimental validation of single vortex streaming pattern and device performance on zebrafish rotation. Lastly, a conclusion of this chapter is given in Section 4.6. The work presented in this chapter has been published on *Nature Communications* (C. Chen et al., 2021).

4.1 Motivation

Owing to their high reproduction rate and genetic and functional similarity to humans, zebrafish (Danio rerio) has been widely used as a model organism for biological, medical, and pathology research, especially human disease modeling and drug

development (Adamson, Sheridan, & Grierson, 2018; Howe et al., 2017; Kari, Rodeck, & Dicker, 2007; MacRae & Peterson, 2015; J. L. Tan & Zon, 2011; Ward & Lieschke, 2002). In these studies, the visualization of the zebrafish and morphological analysis of the zebrafish phenotypes of interests are significant and widespread approaches for exploring the resulting effects of the disease or drugs. Visualizing and analyzing the zebrafish phenotypes in a high-throughput manner for a large number of samples requires an equally efficient manipulation and analysis platform.

The most widely adopted, and readily available method for analyzing zebrafish larvae is through the use of traditional 2D benchtop microscope; numerous enhancements in optical precision and manufacturing have made optical microscopes commonplace in biological labs, making them an accessible and intelligent choice for many analyses. However, during the imaging process for organisms, the target objects to be observe could be block by nearby tissues. In zebrafish, the 2D visualization of target organs of interest is usually obstructed by organs such as the eyes or the yolk sac, or obscured by skin pigmentations (F. Yang, Gao, Wang, Zhang, & Chen, 2016), as shown in Figure 4.1. As a result, some manipulation techniques have been developed to precisely orientate the zebrafish, such that the visualization of obstructed features can be observed after the angular alignment.

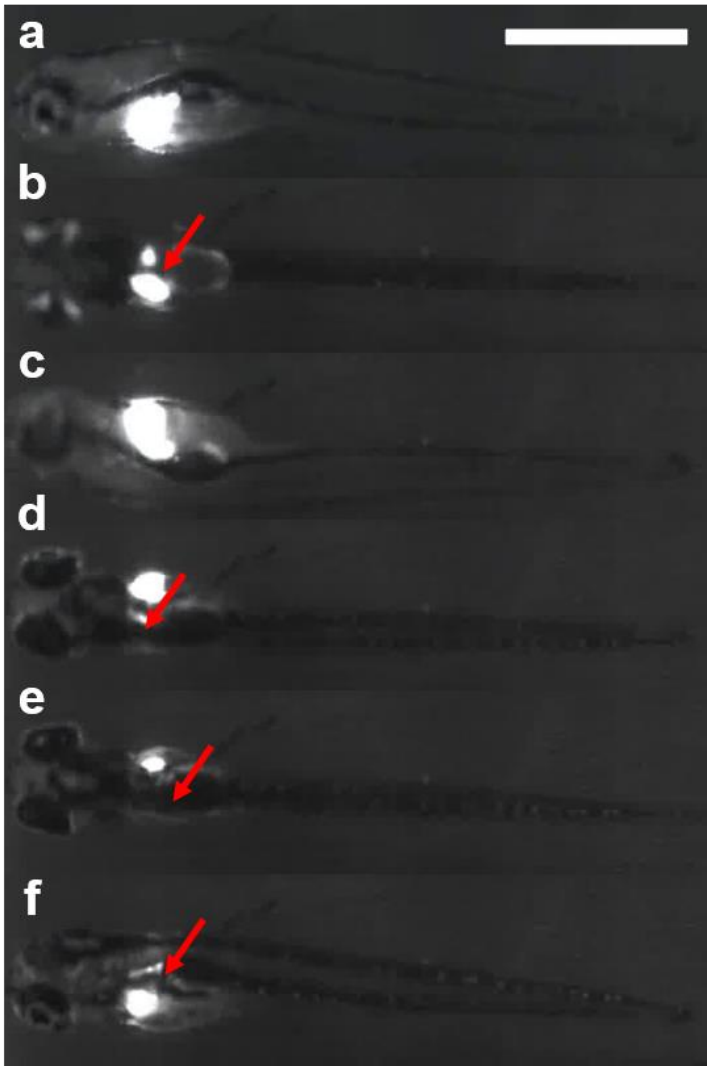

Figure 4.1: A 5 dpf zebrafish larva. The pigmentation (red arrows) obstructs the fluorescent imaging of the zebrafish liver. The liver can be only be clearly imaged from the two lateral sides as shown in a and c. Scale bar: 1 mm.

Due to the ubiquitous nature of 2D optical microscopes, most of the manipulation approaches for zebrafish larvae have focused on ensuring compatibility with research labs' optical equipment. For example, the widely adopted zebrafish immobilization and orientation method of agarose/gel-based confinement either fixes an anesthetized

zebrafish or partially fixes an awake zebrafish for optimal observation at the desired viewing angles; however, this method relies on a tedious fixture process, wherein the gelation process may induce external effects on the zebrafish's natural physiological characters (Gehrig et al., 2009; Mitchell & Wimpenny, 1997) confounding the results. To avoid undesirable impact and the tedious process of chemical based immobilization, researchers developed an automated zebrafish manipulation strategy for fixing the zebrafish position. In the specialized zebrafish handling system (i.e., vertebrate automated screening technology, VAST), small capillary is utilized for immobilization and orientation manipulation of zebrafish larvae; that is, the fish is injected into a small capillary, where it is confined against the walls of the system and oriented using a motorized control platform. This integrated system enables automatic sample loading, rotation, imaging, and other functions necessary for screening (e.g., neuronal regeneration assays) of superficial and deep organs of zebrafish (Pardo-Martin et al., 2013). Although the VAST is a powerful system appropriate for most zebrafish research, the contact-based sample confinement working manner may limit its application on the studies of screening zebrafish morphological abnormities or the studies that involve samples with large size variations (Pulak, 2016; Yanik, Rohde, & Pardo-Martin, 2011).

As a result, researcher have sought to employ non-contact based immobilization strategies which external force fields, such as magnetic or acoustic levitation forces, to provide strong confinement and orientation control while minimizing the external

physical contact. These methods allow for a remarkable level of control over the larvae fixation and reconfiguration. However, while these systems may reduce contact based influence on testing results, certain factors limit their real world application. For example, magnetic based manipulation suffers from low throughputs and a reliance on external reagents to achieve magnetic effects. Similarly, current acoustic manipulation techniques suffer from low throughputs, and may also require the zebrafish to be outside of their native environment which can affect their physiological characterization.

Traditional acoustofluidic techniques have achieved translational and rotational manipulation of small object in a non-contact manner. For example, (Ahmed, Ozcelik, Bojanala, Nama, Upadhyay, Chen, Hanna-rose, et al., 2016) developed an acoustofluidic rotational manipulation technique that achieves trapping and rotational manipulation of cells and *C. elegans* using acoustic streaming generated by microbubble oscillation; (J. Zhang et al., 2019) developed an acoustofluidic chip which is capable to trap the *C. elegans* using standing surface acoustic waves and rotate the *C. elegans* using acoustic streaming; (Collins, Khoo, et al., 2017) leveraged the vortex acoustic streaming generated by narrow-beam focused surface acoustic waves in the horizontal plane to trave cells. To achieve orientation control of the zebrafish larvae for the imaging purpose, the stability of the rotational manipulation is essential. Considering this, the acoustic streaming with a single vortex tube pattern can be an ideal candidate to provide stable and non-contact rotational manipulation for zebrafish rotational imaging. Although the acoustofluidic techniques

achieves non-contact manipulation in the liquid environment, scaling up the dimension of the single vortex for the rotation of organisms in the millimeter scale (*e.g.*, zebrafish larvae) has proven challenging using the acoustofluidic devices with the existing working mechanism. In most of the reported acoustofluidic devices for rotational manipulation, the dimension and speed of the single vortex highly related to the wavelength of the acoustic waves in the system. The dimension of the diameter of the single vortex pattern is usually limited to 0.5-2 times of the wavelength depending on the working mechanism of the device (Guo, Mao, Chen, Xie, Lata, Li, Ren, Liu, Yang, Dao, et al., 2016; Mao et al., 2017; Pulak, 2016). Thus, using the existing mechanism to generate a vortex streaming with ~1mm in diameter for zebrafish rotational manipulation would require acoustic waves with a frequency below ~1 MHz. Based on the fact that the streaming velocity decreases as the acoustic frequency reduces (M. Alghane et al., 2011; Gu et al., 2020; Guo, Mao, Chen, Xie, Lata, Li, Ren, Liu, Yang, Dao, et al., 2016; Lighthill, 1978), the velocity of the single vortex streaming activated by these low-frequency acoustic waves in the existing acoustofluidic platforms will be insufficient to rotate zebrafish larvae which are in the millimeter scale. As a result, when considering the downsides associated with current zebrafish manipulation and imaging techniques, there is still an urgent demand for developing a novel acoustofluidic platform that can perform large-scale zebrafish phenotyping studies in a high-throughput, cost-efficient, and non-contact manner.

In this chapter, we present a novel designing scheme which can generate polarized acoustic streaming with a pattern of single vortex tube. Following this designing scheme, the dimension of the vortex tube streaming can be scaled up and down to enable the acoustofluidic rotational manipulation of different vertebrates based on their size. Then, based on this scheme, we demonstrated an acoustofluidic rotational tweezing (ART) device with a novel working mechanism that enables efficient, stable, and non-contact rotational manipulation of zebrafish. Using the polarized single vortex acoustic streaming activated by surface acoustic waves, zebrafish larvae with different morphologies in a wide size range can be rotated stably with the speed of ~1 second/fish. With this function, this device can be applied to multi-angle imaging of the zebrafish larvae.

4.2 Generation of single vortex streaming

In this section, we introduce the designing principal of the acoustofluidic device which can generate single vortex streaming with a dimension in the millimeter scale. We numerically verified the designing principal and performed parametric study in numerical simulation to optimize the device design. And we explain the working mechanism of using this device for zebrafish rotational manipulation.

4.2.1 Designing principle

To develop a device that is able to generate single vortex acoustic streaming tube with suitable dimension and sufficient speed for the rotational manipulation of zebrafish larva, we established a device which leverages the interaction of the body force generated

by the leaky SAWs propagation and the fluid channel geometry. As shown in Figure 4.2, the device consists of an interdigital transducer (IDT) fabricated on the piezoelectric substrate and a fluid channel. The fluid channel is parallelly aligned to the lateral side of the IDT and it partially overlaps with the effective area of the IDT. By activating the IDT by AC signals, surface acoustic waves (SAWs) are generated on the surface of the substrate. The SAWs propagate symmetrically in the ±x direction with respect to the IDT center. The propagation direction of the SAWs is parallel to the lateral side of the fluidic channel. When the SAWs obliquely leak in the liquid loading on the substrate, it creates a body force which generates acoustic streaming in the liquid. As the channel partially overlaps with the effective IDT area, the body force in the fluid above the IDT (red area) pushed the fluid upwards. Owing to the confined nature of the channel, the fluid subsequently recirculates along the top of the channel before traveling down the opposite wall and generates the single vortex streaming. With this principle, while the SAWs propagate in the ±x directions, the resulting fluid motion, that is the acoustic streaming with a single vortex pattern, is distributed on the y-z planes, with its center near the middle of the channel, which can be characterized as "polarized" acoustic streaming.

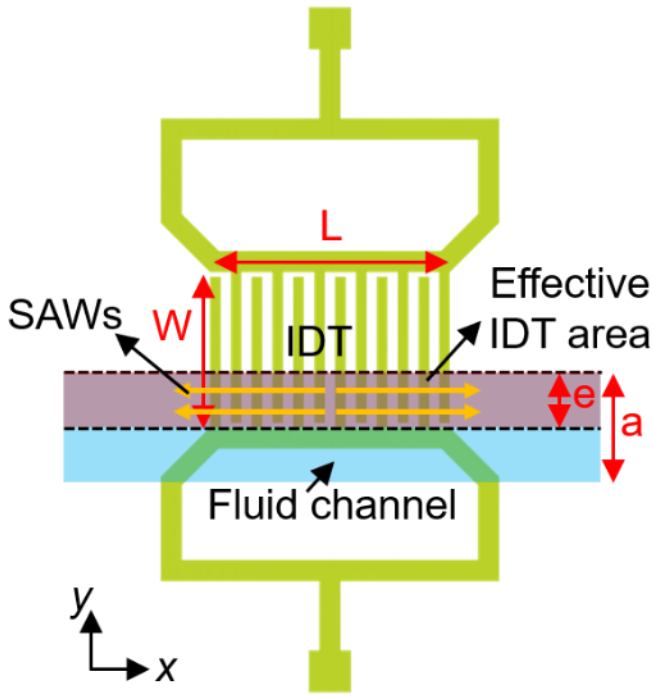

Figure 4.2: Designing principle of the acoustofluidic chip and the geometric variables relative to device design. The fluid channel is aligned parallel to one flank of the IDT. The fluid channel partially covers the effective area of the IDT. The orange arrows indicate the propagation of the surface acoustic waves (SAWs). L: the length of the lateral side of the IDT. W: the width of the IDT aperture. a: the width of the fluid channel. e: the width of the effective area of the IDT covered by the fluid channel.

4.2.1 Numerical simulation

We developed a numerical model to verify this designing principle, investigate the working mechanism, and optimize the acoustic streaming pattern that is generated in the device.

The governing equations of the fluid motion are the continuity equation and Navier-Stokes equation (M. Alghane et al., 2011; Lighthill, 1978):

$$\rho_0 \nabla \cdot \boldsymbol{v}_{dc} = 0 \tag{4.1}$$

$$\rho_0(\boldsymbol{v}_{dc} \cdot \nabla)\boldsymbol{v}_{dc} = -\nabla p_{dc} + \mu\nabla^2\boldsymbol{v}_{dc} + \left(\mu_b + \frac{1}{3}\mu\right)\nabla(\nabla \cdot \boldsymbol{v}_{dc}) - \boldsymbol{F} \tag{4.2}$$

where ρ_0 is the fluid density, μ_b is the bulk viscosity, μ is the shear viscosity, $\boldsymbol{v_{dc}}$ is the steady streaming velocity, and $\boldsymbol{F}$ is the body force as a source term to activate the acoustic streaming. For acoustic streaming activated by SAW propagates in the +x direction, $\boldsymbol{F}$ decays as it propagates from the center of the IDT, and can be expressed as (x):

$$F_x = -(1 + \alpha_1^2)A_m^2\omega^2 k_i e^{[2(k_i x + \alpha_1 k_i z)]} \tag{4.3}$$

$$F_y = 0 \tag{4.4}$$

$$F_z = -(1 + \alpha_1^2)A_m^2\omega^2 k_i \alpha_1 e^{[2(k_i x + \alpha_1 k_i z)]} \tag{4.5}$$

where $\alpha = i\alpha_1$.

We performed the numerical simulations using the finite element method (FEM)-based software package, Comsol Multiphysics 5.4 (COMSOL AB, Sweden) based on the aforementioned theoretical model. The pre-defined "Laminar Flow" interface with FEM formulations of the governing equations presented in (4.1) and (4.2) was applied to the 3D solution domain (Figure 4.3). This domain is a section of fluid in the channel above the IDT area (domain length: 3.4 mm, IDT length: 3.15 mm). The body force in equation (4.3) - (4.5) was applied to the portion of fluid domain which lies above the IDT (as marked by the white dashed frame in Figure 4.3) because the SAWs and thus the body force in this area is much stronger in this region. An "outlet" condition was applied to the two ends of

the channel. The boundary conditions at the bottom and sides of the channel were set to "no slip" ($\mathbf{v}_{\mathrm{dc}} = \mathbf{0}$). A "stationary" solver was applied to solve the steady acoustic streaming pattern in the fluid domain.

In the following subsections, first, we leverage this numerical model to verify the streaming pattern generated within the fluid domain based on the abovementioned designing principle. Then, we explore streaming patterns for different values of variables (e.g., effective IDT area overlapped with the channel bottom and channel width) and provide reference for the optimization of chip design. Last, we numerically verified the feasibility of using this "polarized" acoustic streaming generated based on our designing principle to rotate a zebrafish larva.

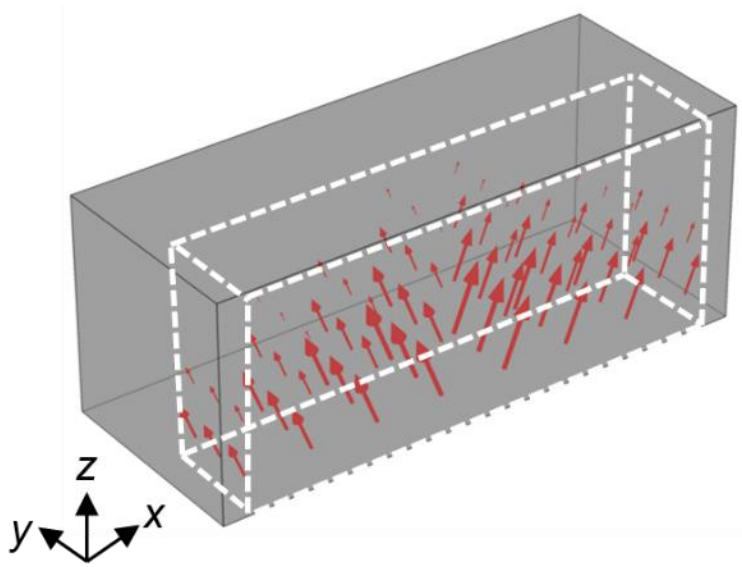

Figure 4.3: 3D domain of the numerical simulation. The white dashed frame indicates the portion of fluid domain which lies above the IDT. The red arrows indicate the distribution of the body force that activates acoustic streaming.

4.2.2 Effect of width of the effective IDT area (e) to the streaming pattern

In the abovementioned designing principle (Figure 4.2), we proposed that the single vortex pattern can be generated by aligning the channel parallel to the lateral side of the IDT (y axis) with half of its width overlapping with the IDT area. Here, we fix the channel width (a) to 1.34 mm, IDT length (L) to 3.15 mm, and the acoustic frequency (f) to 23.9 MHz. Then, we numerically explored the effect of the width of the effective IDT area (e) to the streaming pattern in the fluid domain.

Figure 4.4 shows the streaming pattern in 3D fluid field and the streaming pattern on the yz-plane at the middle of the simulation domain for different value of e. As shown in Figure 4.4, a single vortex pattern can be generated based on our designing principle. If the channel partially overlaps with the IDT (Figure 4.4a-g), the single vortex pattern is formed on the y-z planes and the pattern extends along the length of the channel for the distance of the IDT length (L). And if the whole channel is placed on the IDT (Figure 4.4h), the vortex streaming pattern will not be formed. Thus, the single vortex pattern can be generated when only a fraction of the channel overlaps with the IDT.

In addition, the width of effective IDT area (e) affects the location of the center of the vortex pattern (indicated by the red asterisks). When much less or much more than a half of the channel is placed on the IDT, the center of the single vortex is far away from the center of the channel in the y axis. When an object is in the vortex streaming, it will be trapped at the center of the vortex and start to rotate. Thus, the value of “e” not only affects

the location of the vortex center, but also stable rotation position of a zebrafish larva. In the cases that the vortex center offsets from the center of the channel, the rotation of the zebrafish larvae was predicted to be unstable because of the asymmetric streaming pattern and the possible resistance from the channel wall. By placing about half of the channel upon the IDT ($0.45a \leqslant e \leqslant 0.55a$, Figure 4.4c-e), the center of the vortex streaming closely overlaps with the center of the channel in the y axis, where we predict the stable rotation axis of the zebrafish larvae will be. In this range, the distance of the 600-μm-wide larva to the channel wall will be about 350 μm, which allows the zebrafish larvae within the size range (<~850 μm for 5 dpf larvae) to be rotated with a low chance of contacting the channel wall. Thus, based on the parameter sweep of the value of "e", setting the ratio of the overlapping widths of the IDT area (e) to the channel cross sectional width (a) to e=0.5a, which means that if half of the channel width was located upon the IDT the system can provide optimal performance for zebrafish larvae rotational manipulation.

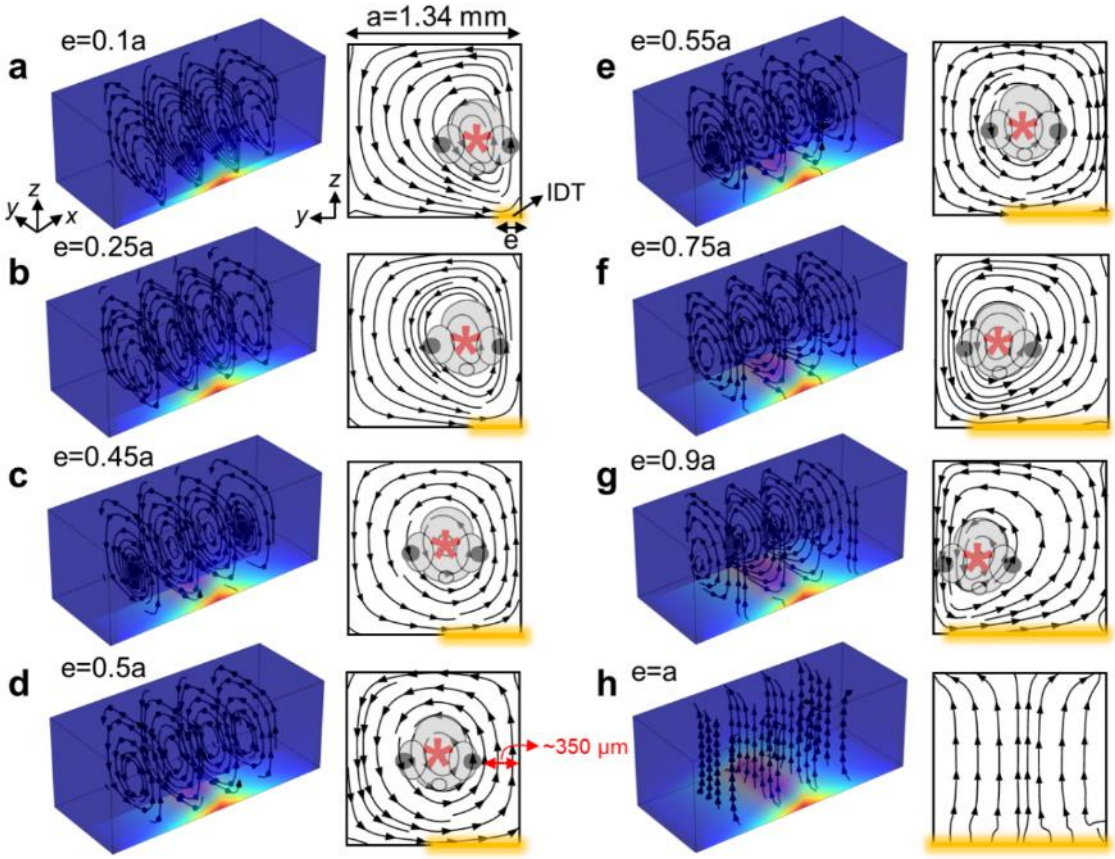

Figure 4.4: Simulation results showing the effect of width of the effective IDT area (e) to the streaming pattern. a-h, Streaming pattern in 3D field and a streaming pattern on the yz-plane at the middle of the simulation domain for the corresponding value of e, respectively. The color shows the amplitude of the body force with red for large values and blue for small values. The red asterisks indicate the centers of the vortex streaming fields, which predict the location of the rotation axis. The zebrafish schematics indicate the predicted positions of stable rotation of a larva with maximum width of 600-μm (the dimension of typical 5 dpf larvae) in the corresponding cases. a,b,f,g, When much less or much more than a half of the channel is placed on the IDT, the center of the single vortex is far away from the center of the channel in the y axis. In these cases, the rotation of the zebrafish larvae was predicted to be unstable because of the asymmetric streaming pattern and the possible resistance from the channel wall. c-e, If about half of the channel is placed upon the IDT (0.45a⩽e⩽0.55a), the center of the vortex streaming closely overlaps with the center of the channel in the y axis, where we predict the stable rotation axis of the zebrafish larvae will be. In this range, the distance of the 600-μm larvae to the channel wall will be about 350 μm which allows the zebrafish larvae which fall within the size range (<~850 μm for 5 dpf larvae) to be rotated with a low chance of contacting the channel

wall. Thus, the device fabrication of the acoustofluidic zebrafish larvae rotation device was designed to be e=0.5a, which means a half of the channel width was located upon the IDT. h, Vortex streaming pattern will not be formed if the whole channel is placed on the IDT.

4.2.3 Effect of channel width

Through our numerical investigation, we found that this single vortex pattern can be generated for any size channel, as long as the "e=0.5a" condition is satisfied. Hence, the size of the vortex can be adjusted by scaling "e" and "a" proportionally. Moreover, the length of the vortex tube structure along the channel length is determined by the lateral side length of the IDT (L). These results imply that larger or smaller channels could be designed to handle organisms of various sizes, and the single vortex streaming pattern can be scaled to enable the acoustofluidic rotational manipulation of different vertebrates.

Considering that the length of the 5 dpf zebrafish larvae is about 3.5 mm, in this work, we designed an IDT containing 21 pairs of IDT fingers which are 37.5 μm in width. The overall geometry of the IDT is L=3.15 mm and W=2.24 mm. This IDT was activated by 23.9-MHz AC signals.

As a proof that vortex tubes with adjustable sizes can be generated based on the "e = 0.5a" rule, we numerically validated the formation of single vortex streaming within two channels with different sizes as shown in Figure 4.5 (a=0.8 mm and a=1.34 mm).

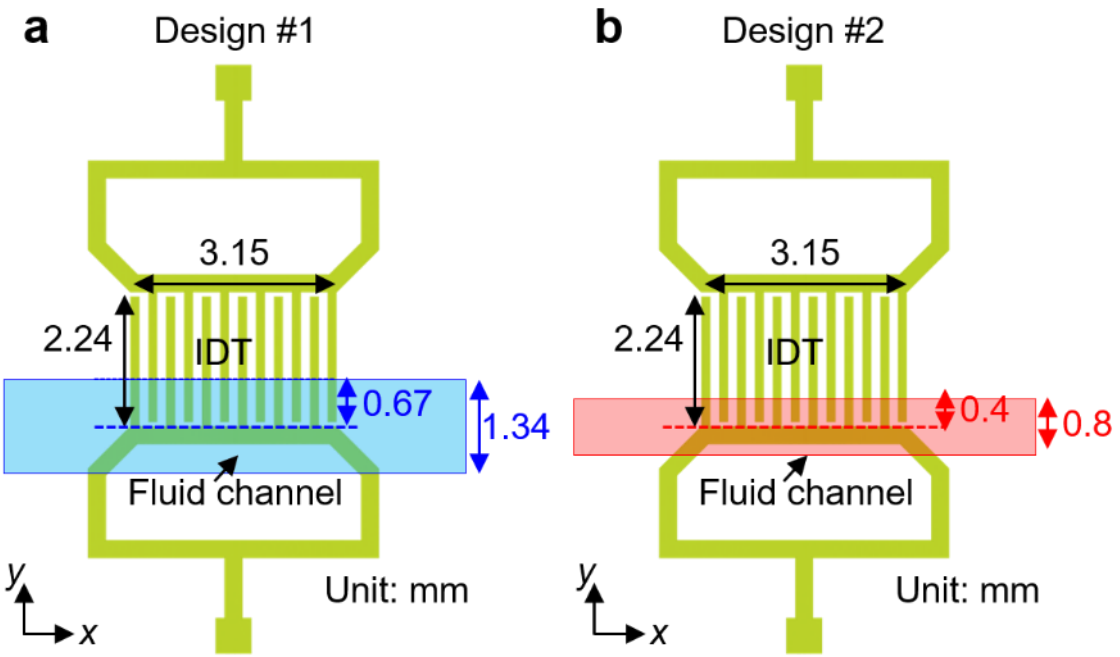

Figure 4.5: Labeled schematic and geometric variables of the acoustofluidic rotational manipulation device. a, b, Values of the key variables explored in this work. The two designs of channels assembled with this IDT following the "e=0.5a" rule. The width of the fluid channel was set to a=1.34 mm and a=0.8 mm as marked by the blue and red shaded rectangles. The dashed lines indicate the middle of the channel.

The results for the 1.34-mm and 0.8-mm channels are shown in Figure 4.6. Both channels were placed over the IDT mentioned above and aligned following the "e=0.5a" rule. The simulation results validate that using this "e=0.5a" design rule, millimeter-scale single vortex patterns with centers aligned along the middle of the channel can be generated without changing the IDT configuration or applied actuation signals. And, the size of the vortex tube can be adjusted by scaling "e" and "a" proportionally for its width, and by scaling the IDT length "L" for its length.

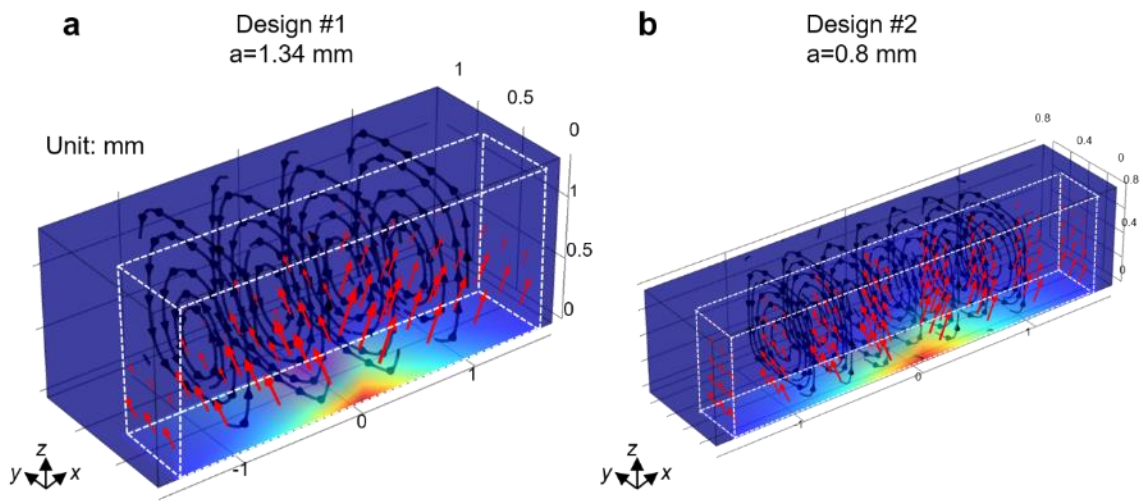

Figure 4.6: The distribution of the body force (red arrows) and the streaming pattern (black streamlines) in the devices with a=1.34 mm (a) and a=0.8 mm (b). The body force was applied to the domain upon the IDT area marked by the white dashed frame, which covers half of the channel in width. The color shows the amplitude of the body force with red for large values and blue for small values. Single vortex acoustic streaming pattern on the yz-planes extends along the channel in the x direction and enables the acoustofluidic rotational manipulation of objects that lie in this area.

4.2.4 Feasibility of zebrafish rotation

To further confirm that the single vortex generated based on our designing principle can achieve rotational manipulation to zebrafish larvae, we performed a numerical simulation on the streaming pattern when a larva is loaded to the channel and analyzed the total stress on the zebrafish surface at the beginning of the rotation. To simplify this simulation, we assumed that the zebrafish is not rotated by the streaming. The zebrafish model was confined to a domain deducted from the fluid domain and the simulation was performed in the fluid domain. The surface of the zebrafish (which is supposed to be a fluid-solid interface in the real case) was set to the boundary condition "no slip (**u**=0)". As shown in Figure 4.7, the single vortex streaming can still be generated

in the fluid surrounding the zebrafish. Thus, we numerically confirmed that our design can be applied to zebrafish rotational manipulation. Assuming that the larva does not move, the maximum amplitude of the total stress ($\left[-p\boldsymbol{I} + \mu(\nabla \boldsymbol{v}_{fluid} + (\nabla \boldsymbol{v}_{fluid})^T)\right] \cdot \boldsymbol{n}$) on the zebrafish surface is 0.45 Pa in a single vortex with a maximum velocity of 2 mm/s, which approximately fits with the experimentally measured maximum streaming velocity at the 12.75 V_{PP} applied voltage. The integral of this total stress tensor on the zebrafish surface acquires a hydrodynamic force with an amplitude of 4.48×10^{-8} N. Since this total stress and the hydrodynamic force is relatively mild and in the actual situation the zebrafish is freely suspended in the fluid without any constraint, our design can provide gentle and bio-compatible manipulation to zebrafish.

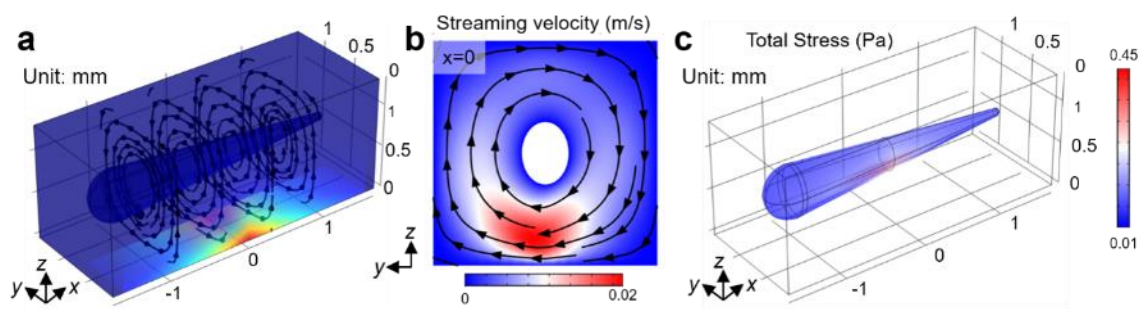

Figure 4.7: Numerical Simulation results showing the streaming pattern with a zebrafish larva in the channel (a=1.34 mm). a, Streaming pattern in 3D fluid domain can be formed with a zebrafish larva in the channel. b, The resulting streaming velocity and streaming pattern on a 2D cross-sectional plane at x=0. The streamlines with arrows indicate the pattern of acoustic streaming. c, The total stress distribution on the surface of zebrafish larva.

4.2.4 Conclusion

With the above exploration, we proposed an acoustofluidic chip as shown in Figure 4.8 for the rotational manipulation of zebrafish larva. The acoustofluidic chip consists of an interdigitated transducer (IDT) fabricated on a lithium niobate ($LiNbO_3$) piezoelectric substrate. When applying an AC signal, the IDT generates acoustic waves (SAWs) which propagates in the ±x directions on the surface of the substrate. A patterned fluidic channel with a square cross-section is aligned parallel to the lateral side of the IDT (y axis) with half of its width on the IDT. The SAWs obliquely leak into the liquid confined in the fluid channel and induce a body force that generates acoustic streaming. Due to the confined nature of the channel, the fluid above the IDT is jetted upwards by this body force, where it subsequently recirculates along the top of the channel before traveling down the opposite wall and forms a single unidirectional vortex pattern on the y-z planes. A zebrafish loaded to the channel can be stably rotated by the "polarized" acoustic streaming vortex.

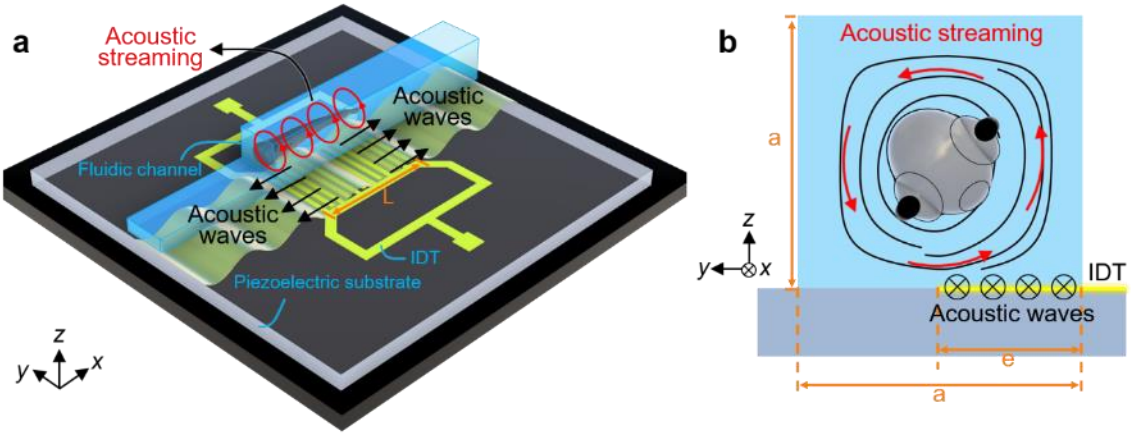

Figure 4.8: Schematic illustration of the acoustofluidic rotational manipulation device. a, The 3D experimental configuration of the acoustofluidic chip for rotational manipulation of zebrafish larvae. b, The 2D schematic on the yz-plane.

4.3 Device fabrication

To fabricate acoustofluidic chip, we chose 128° Y-cut lithium niobate wafer ($LiNbO_3$, Precision Micro-Optics, USA, double-side polished, 500 μm thick) as the piezoelectric substrate for the generation of surface acoustic waves. The fabrication process is shown in Figure 4.9. First, the interdigital transducer (IDT) was patterned on the piezoelectric substrate by e-beam evaporation of 5 nm Cr and 50 nm Au followed by standard photolithography and lift-off process. In the second step, we spin-coated an 8-μm photoresist (SU-8 10, MicroChem Inc., USA) on the top of the IDT area. This layer insulates the electrical signal generated within the piezoelectric substrate. Next, we use e-beam evaporation to deposit an Au layer with 100 nm in thickness over the IDT area. This layer obstructs the IDT and enhance the sample observation. The fluid channel consists of two parts: a PDMS channel and glass capillaries with a square cross-section (1×1 mm^2). The mold was designed using Fusion 360 (Figure 4.10) and fabricated on aluminum block

using CNC machining. The PDMS channel was made through standard soft-lithography procedure using this mode. The PDMS channel was bonded to the coated substrate via an oxygen plasma surface treatment. The glass capillaries with a 1×1 mm^2 cross-section (VitroCom, USA) were connected to the open ends of the PMDS channel using silicone adhesive. Last, silicone tubing (EW-06411-62, Masterflex, USA, inner diameter: 1.59 mm) were connected with the ends of the capillaries. External wires were connected to the electrodes of the IDT using silver epoxy (MG Chemicals, USA) to provide the activation signals.

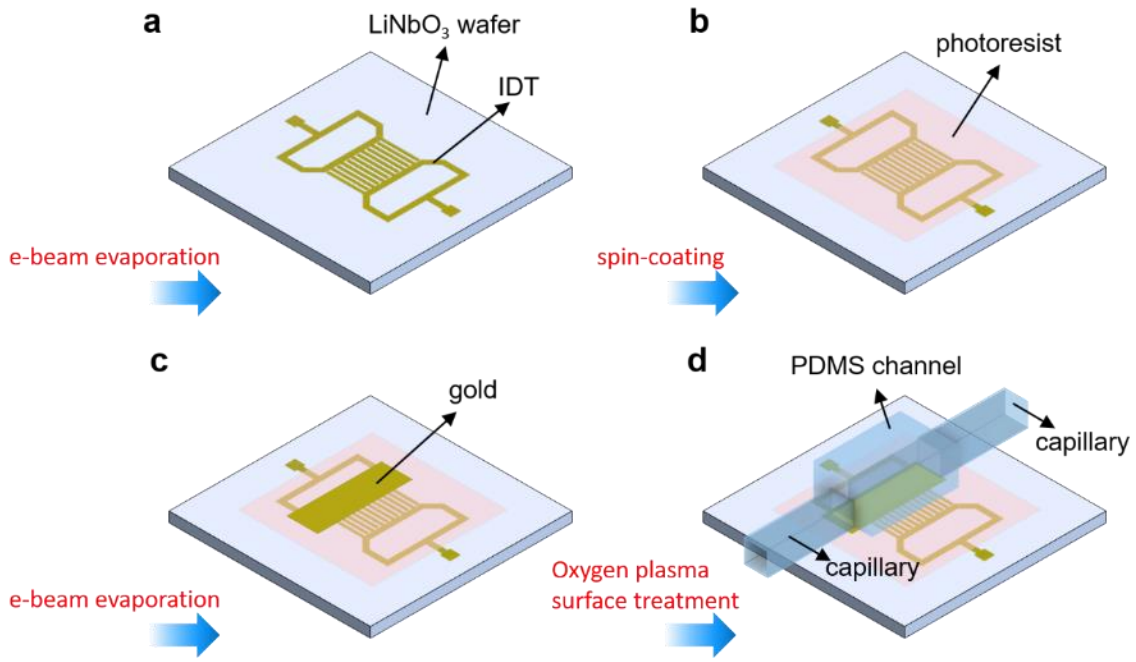

Figure 4.9: Schematic illustration of the fabrication of the acoustic device. a, Fabrication of the IDT on the $LiNbO_3$ substrate using e-beam evaporation. b, A photoresist layer was spin-coated on the IDT as an insulation layer. c, A gold layer was deposited on upon the photoresist layer to obscure the IDT during zebrafish imaging. d, A fluid channel composed of PDMS channel and capillaries was bonded to the substrate.

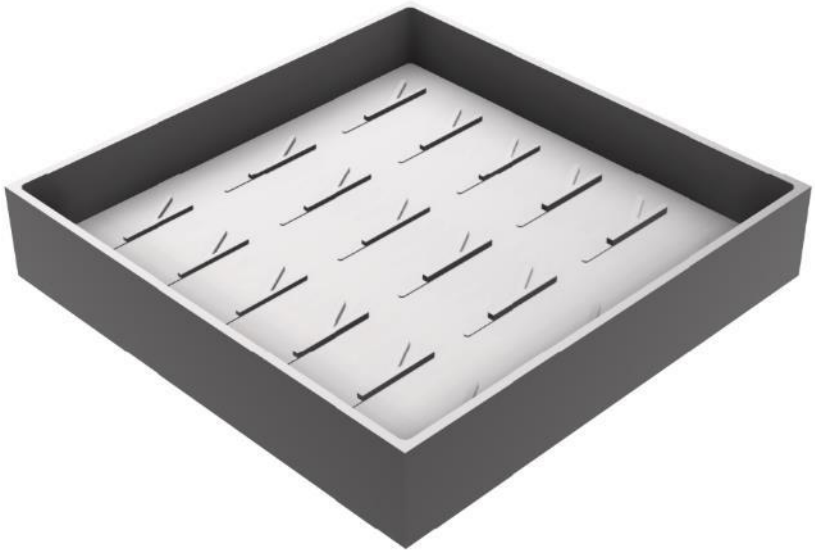

Figure 4.10: Design of the mold for PDMS channel fabrication.

4.4 Experimental validation of single vortex streaming pattern

In this subsection, we introduce the methods of the device operation and experimentally measure the streaming patterns in the acoustofluidic chips with channel width of a=1.34mm and a=0.8 mm as shown in Figure 4.6.

4.4.1 Methods

The AC voltage signals to activate the chip were generated by a waveform generator (AFG3102C, Tektronics Technology Corporation, PA, USA) and amplified by an amplifier (25A250A, Amplifier Research, USA). For most cases of zebrafish larvae rotation, the AC signals were set to 12.75 Vpp in voltage and 23.9 MHz in frequency. The chip is mounted to an upright microscope (BX51WI, Olympus) with a CCD camera (CoolSNAP HQ2, Photometrics) for the measurement of the streaming pattern.

4.4.2 Measurement of acoustic streaming

As an example, we numerically and experimentally explored the single vortex streaming patterns generated within two different channels with sizes of 1.34×1.34-mm^2 and 0.8×0.8-mm^2; both channels were placed over the same IDT and aligned following the "e=0.5a" rule. The IDT has an aperture width of W=2.24 mm, a lateral side length of L=3.15 mm, and were composed of 21 pairs of 37.5-μm fingers. Figure 4.11a shows the simulated and experimental streaming pattern for the 1.34×1.34-mm^2 channel with an input frequency of 23.9 MHz. 1-μm fluorescent particles were used to experimentally visualize the flow field of the top and bottom plane. From this experiment we observed that the fluid was pulled toward the IDT along the bottom of the channel and pushed in the opposite direction along the top of the channel. This experimental fluid motion closely mimicked the numerical streaming patterns on the corresponding planes of the simulated channel. A similar phenomenon can be found in the 0.8×0.8-mm^2 case as shown in Figure 4.11b. Thus, with our design, millimeter scale single vortex patterns with centers in the

middle of the channel can be generated without changing the IDT design or actuation signals.

4.5 Rotational manipulation of zebrafish larvae

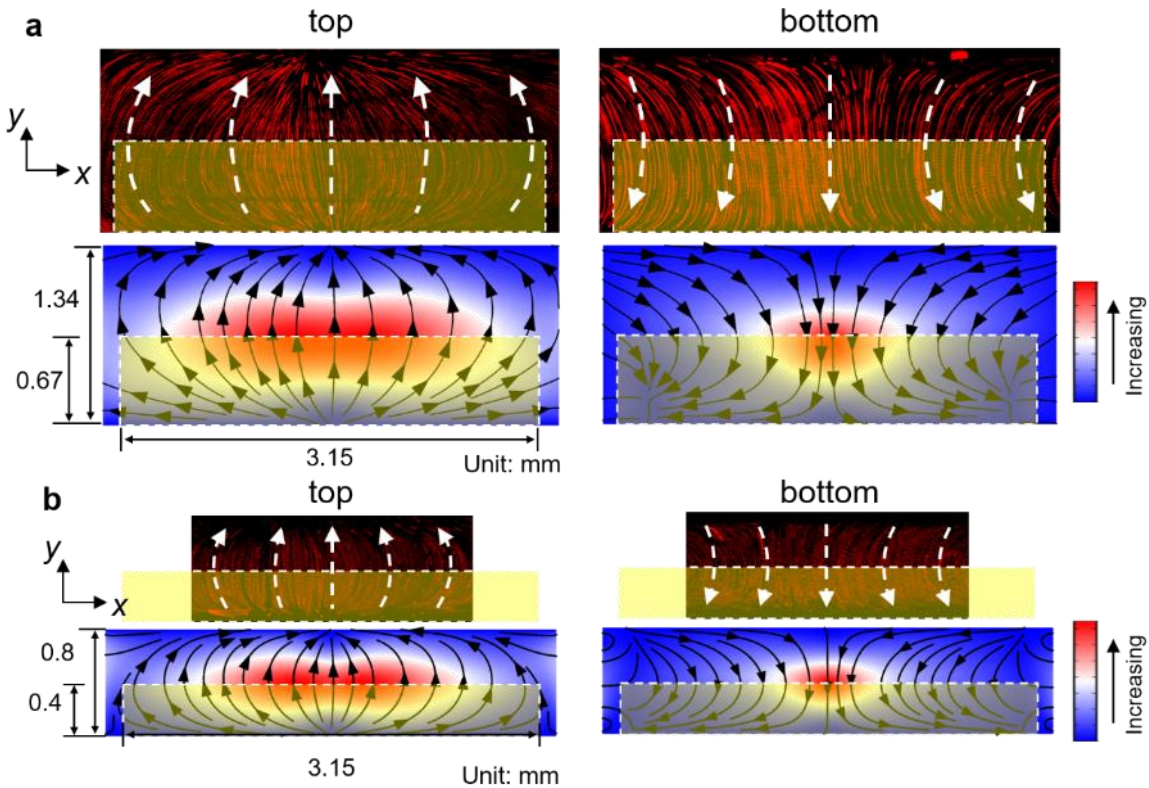

Figure 4.11: Experimental and numerical demonstration of acoustic streaming in the channel with a width of 1.34 mm (a) and 0.8 mm (b). The streaming pattern were measured on the xy-planes close to the channel top and bottom. The yellow shadowing box indicates the IDT area with a length of 3.15-mm and a width of a half of the channel width.

In this subsection, we applied two acoustofluidic chips with channel width of a=1.34mm and a=0.8 mm to rotate zebrafish larvae (Figure 4.6). We explored the devices' performance on the rotational manipulation of zebrafish larvae for AC signals with different amplitudes.

4.5.1 Zebrafish larvae preparation

The zebrafish (Danio rerio) studies were approved by the Institutional Animal Care & Use Committee at Duke University (protocol # A154-18-06). Zebrafish embryos/larvae were cultured in egg water at 28 °C and 14-hour light/10-hour dark conditions. All the experiments were performed on zebrafish up to 5 days post fertilization (dpf). The zebrafish larvae were anesthetized with 1× Tricaine (~0.2 mg/ml; Sigma, USA) to prevent active movement during rotational manipulation. 1% Pluronic® F-127 surfactant (Sigma, USA) was added to the solution to improve the smoothness of the rotational motion.

4.5.2 Rotational manipulation of zebrafish larvae

Having numerically and experimentally verified the single vortex streaming patterns in the channel, we sought to exploit the contactless acousofluidic manipulation to rotate zebrafish. Here, we focused on zebrafish larvae that had an age of 5 days post fertilization (dpf). The dimension of the zebrafish larvae in this stage are usually around 3.2-mm in length and 0.7-mm in width. We investigate the performance of the acoustofluidic chip with a channel whose cross sections is 0.8×0.8-mm^2.

As shown in Figure 4.12a, a 5 dpf zebrafish larva anesthesized with Tricaine to prevent active movement was delivered to the rotational manipulation area. During the acoustic excitation of the vortex streaming pattern in the liquid surrounding the zebrafish, the larvae was trapped at the center of the vortex, and stably rotated by the fluid-induced

drag force anticlockwise from the view of yz-plane. Figure 4.12b shows the image sequence of a rotation cycle of a 5 dpf zebrafish larva in the microfluidic channel. The experimental results demonstrated that the rotational manipulation of the zebrafish larvae allows for observation from multiple axial views. Next, we explore the speed of the zebrafish rotational motion. Due to the complex nature of the fluid motion within the channel, the size variation of the features of the fish (e.g., body shape, size, and mass distribution) may slightly affect the rotation speed. Here, we charactered the rotation period using four randomly selected 5 dpf zebrafish larvae (Figure 4.12c). Their size varies from 3.38 to 3.60 mm in length and 0.60 to 0.63 mm in width. Figure 4.12c, by adjusting the peak-to-peak voltage of the AC signals from 10 V to 16 V, the period of a 360° continuous rotation for the 5 dpf zebrafish larvae decreased from ~6 s to ~1.5 s.

These experimental results verified that the zebrafish larva with a common dimension of about 0.6 mm in width can be rotated using the device with a 0.8-mm fluid channel. However, for some phenotyping research, the diseases or the chemical studied could induce the morphological abnormalities (e.g., edema and body curvature) within the zebrafish. For these zebrafish, their geometry could be different from the common zebrafish and their size could be larger than the regular ones. Considering this, we tested the performance of an acoustofluidic device with the channel with a 1.34×1.34-mm^2 cross section.

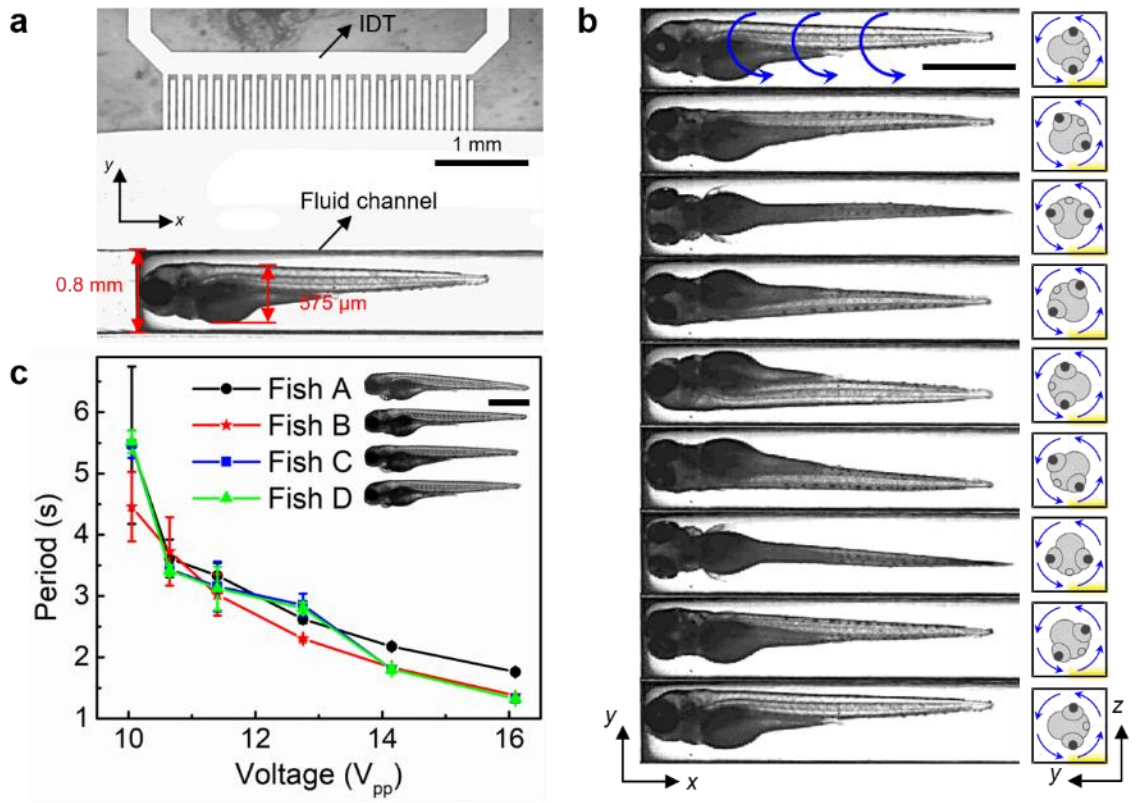

Figure 4.12: Zebrafish larvae rotational motion evaluation in a channel with 0.8×0.8 mm² in the cross section. Scale bar: 500 μm.In Figure 4.13a, the image sequence shows a cycle of the rotational motion of a 5 dpf anesthetized zebrafish larva in the acoustofluidic device with a 1.34-mm-channel. The larva was stably rotated counterclockwise with respect to the yz-plane by the fluid-induced drag force. The rotation period was characterized using four randomly selected 5 dpf larvae (length: 3.43~3.6 mm, width: 0.63~0.71 mm). As shown in Figure 4.13b,c, by adjusting the peak-to-peak voltage of the AC signals from 10 V to 16 V, the period of a 360° continuous rotation for the 5 dpf zebrafish larvae decreased from ~2 s to ~0.5 s.

The rotation speed of the zebrafish larvae in the 1.34-mm channel was approximately 65% faster than that in the 0.8-mm-channel. This is because the wider channel results in more liquid between the zebrafish larvae's body and the channel wall, and more acoustic energy can be loaded into the larger liquid volume for generating sufficient acoustic streaming. Additionally, the increased distance between the larvae and

the channel wall decreases the chance that the zebrafish will contact the wall and increases the stability of the rotation. And this larger device also broads the range of larvae size that can be manipulated within the channel. Considering the efficiency of energy transfer and the possible shape/size variation across different zebrafish larvae, the 1.34×1.34 mm^2 cross section was chosen for the rotational experiments in the remainder of this work.

As shown in Figure 4.13b and c, the rotation period could be slightly different for different sample. This is induced by the variation in the feature sizes of zebrafish samples (e.g., body shape, body size, and mass distribution). This variance in the resulting rotation velocity depends on the streaming velocity at which the fluid motion reaches a stable state when interacting with the zebrafish. However, it is important to note that, while the rotation period may vary for different sized zebrafish, a large enough drag force can quickly bring the zebrafish into a stable and consistent rotation mode with a constant angular velocity. This is achieved by applying a high input voltage to generate vortex streaming. As such, in considering a balance between stable performance and the excess power consumption, the optimized input voltage was set at 12.75 V_{PP} for future manipulations. This voltage yields rapid and stable rotational manipulation since the drag force generated by the fluid streaming is sufficiently large to overcome the inertia of the zebrafish.

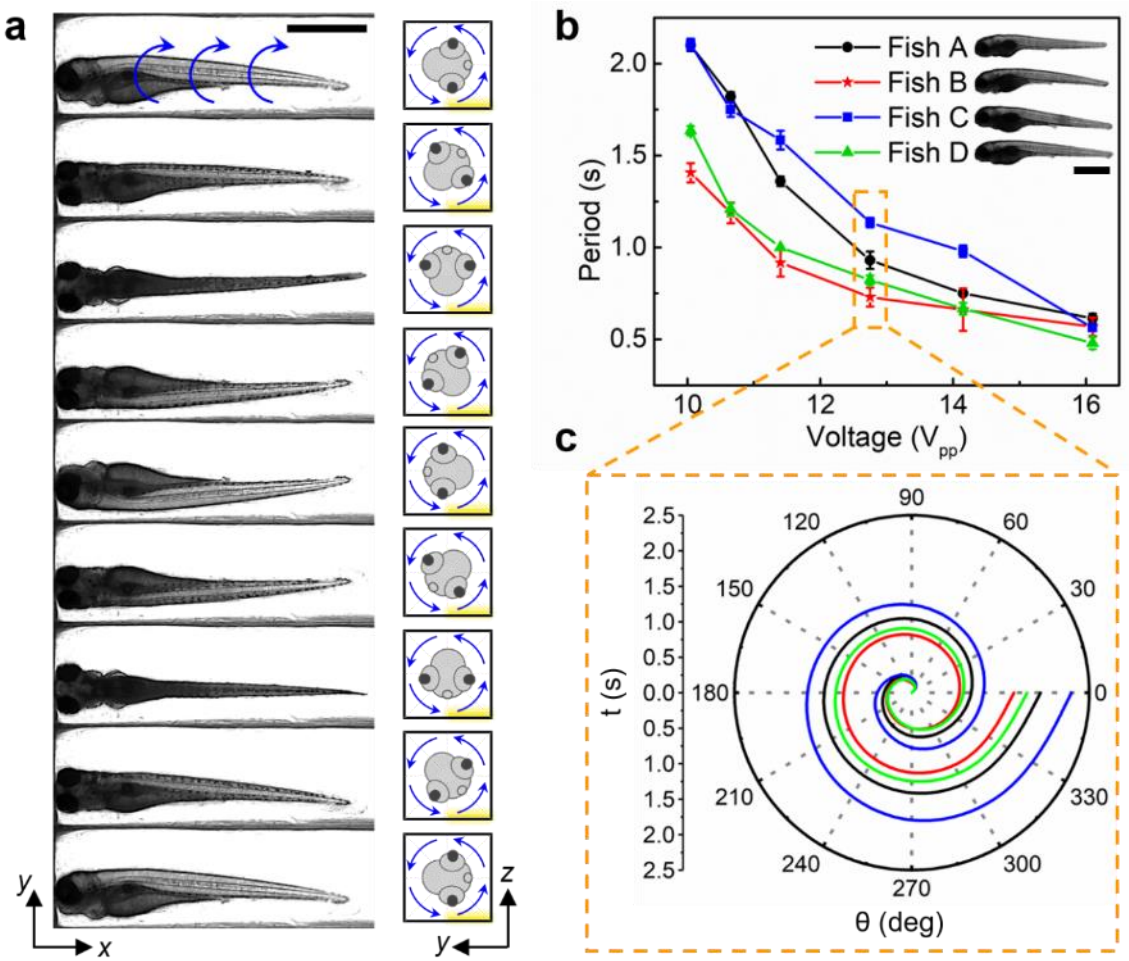

Figure 4.13: The performance of the acoustofluidic chip for high-speed, rotational manipulation of 5 dpf zebrafish larvae. a, Image sequence showing a cycle of the rotational motion of a 5 dpf anesthetized zebrafish larva in the acoustofluidic device. The larva was stably rotated counterclockwise with respect to the yz-plane by the fluid-induced drag force. Scale bar: 1 mm. b, The rotation periods of four typical 5 dpf zebrafish larvae (length: 3.43~3.6 mm, width: 0.63~0.71 mm) as a function of the driving voltage (Vpp). Overall, the rotational speed of the zebrafish larvae increases as the driving voltage increases. Data are graphed as the mean ± SD (n=6). Scale bar: 1 mm. c, The rotation angle over a single rotational cycle with respect to time for four typical zebrafish larvae at 12.75 V_{pp}.

With the above exploration, we determined the optimized parameters for the acoustofluidic device for zebrafish rotational manipulation. Next, we applied this device

to rotate the zebrafish larvae with morphological abnormalities to further confirm that the device can perform the contactless rotational manipulation without changing the innate morphological characteristics of the sample.

Figure 4.14a-c shows a 5 dpf zebrafish larva without morphological abnormalities, a 5 dpf zebrafish larva with moderate edema and tail curling, and a 5 dpf zebrafish larva with severe edema and tail curling, respectively. They were loaded to the device before the fluid streaming was activated. The first row of the Figure 4.14 shows their initial shape at equilibrium states before rotation. Then we turned on the AC signals (12.75-V_{PP}) and the zebrafish larvae started to rotate. The second to fourth rows of the Figure 4.14 show the shape of the zebrafish during three cycles of rotation when they reached to the same angle of their initial equilibrium states. The last row of Figure 4.14 shows the shape of the zebrafish when they stopped the rotation and reached to the equilibrium states again. We compared the shape of the zebrafish at equilibrium states before rotation, during rotation by streaming activated at 12.75-V_{PP} voltage, and after rotation back to its equilibrium position by observing the contours of the fish in Figure 4.14. No obvious differences were observed due to the presence of the single vortex streaming. We also compared the angles of the tail curvature before, during, and after rotation by vortex streaming, and detected no change in the degree of tail curling.

Thus, we confirm that the proposed device can perform the rotational manipulation without changing the innate morphological characteristics of the sample for zebrafish larvae within a broad size/shape range.

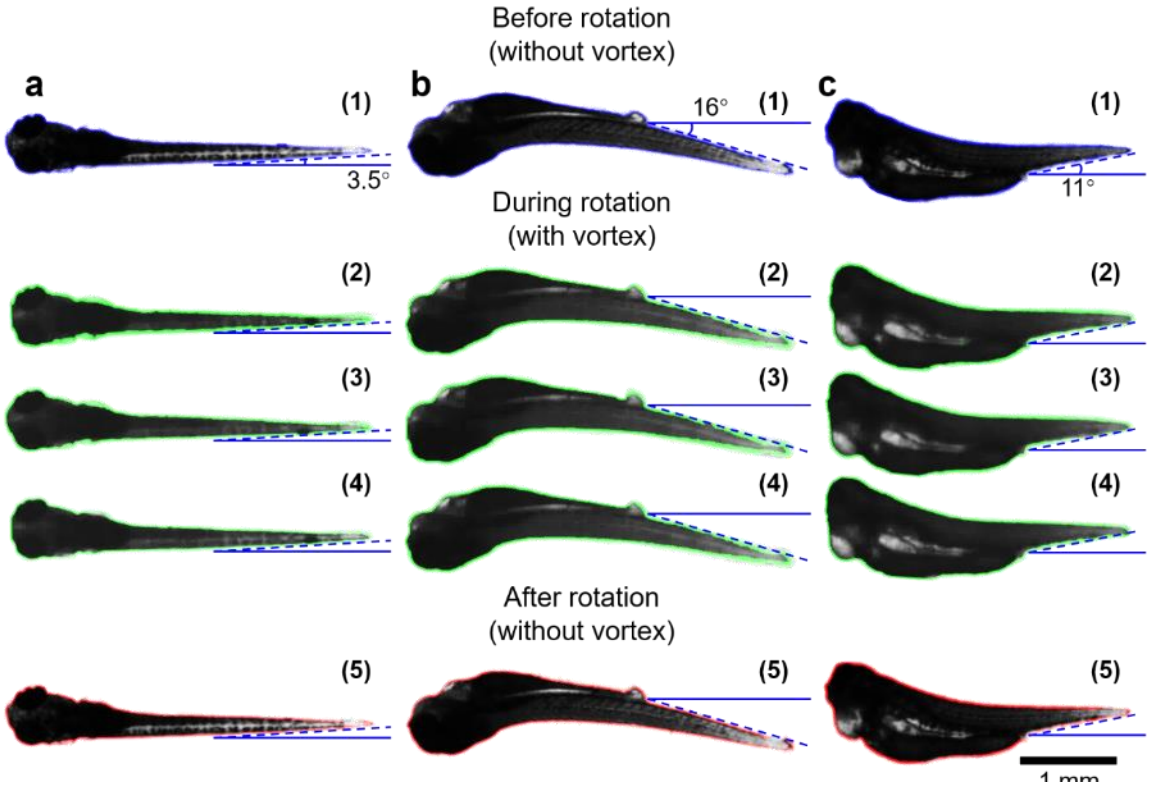

Figure 4.14: Comparison of zebrafish tail curling before (no vortex streaming), during (with vortex streaming), and after rotation (no vortex streaming). a, A 5 dpf zebrafish larva without edema or tail curling. b, A 5 dpf zebrafish larva exposed to 1.5% EtOH shows moderate edema and tail curling. c, A 5 dpf zebrafish larva exposed to 1.5% EtOH shows severe edema and tail curling. Scale bar: 1 mm. Figures (1) show the equilibrium status of the zebrafish outside of the vortex, figures (2)-(4) show the zebrafish during different rotation cycles at same corresponding viewing angles as figure (1) with respect to each group, and figures (5) were taken after the vortex vanished and the zebrafish reached equilibrium again. The angle gauges of figures (1) which indicate the original tail curling degree of each group were duplicated to other figures in the corresponding group to compare the angles of tail curling. By comparing angles of the tail curvature before, during, and after rotation by vortex streaming, no change in the degree of tail curling or body shape was detected.

4.5.3 Discussion

Besides rotational manipulation of 5 dpf zebrafish larvae, our acoustofluidic rotational tweezing device is also compatible with the manipulation of zebrafish at different stages of development, which have different morphologies. One interesting finding is that our device achieves the rotation of zebrafish yolk without tearing the chorion. As shown in Figure 4.15a, when a zebrafish embryo (0 dpf, prior to tail extension) is loaded into the device, the leaky SAW penetrates the chorion of the embryo and generates the single vortex streaming in the perivitelline fluid within the chorion. Thus, the yolk can be rotated by the streaming in the chorion. This observation has an implication for acoustofluidic-enabled, non-contact rotation, wherein the yolk, which is the internal structures of the embryo, can be rotationally manipulated without removing the external membrane. With this function, the need for an additional dechorionation step (i.e., mechanical dechorionation by manually removing the chorion using forceps under a microscope and enzyme-supported dechorionation using 1% Pronase solution) which is required for contact-based manipulations can be eliminated. Furthermore, Our contactless rotational manipulations and be used to many protocols for chemical/drug screening studies that require the existence of the chorion, as well as testing of a large number of embryo samples for improving statistical confidence in the results (Henn & Braunbeck, 2011; Martinez-Sales, García-Ximénez, & Espinós, 2014; Teixidó et al., 2019).

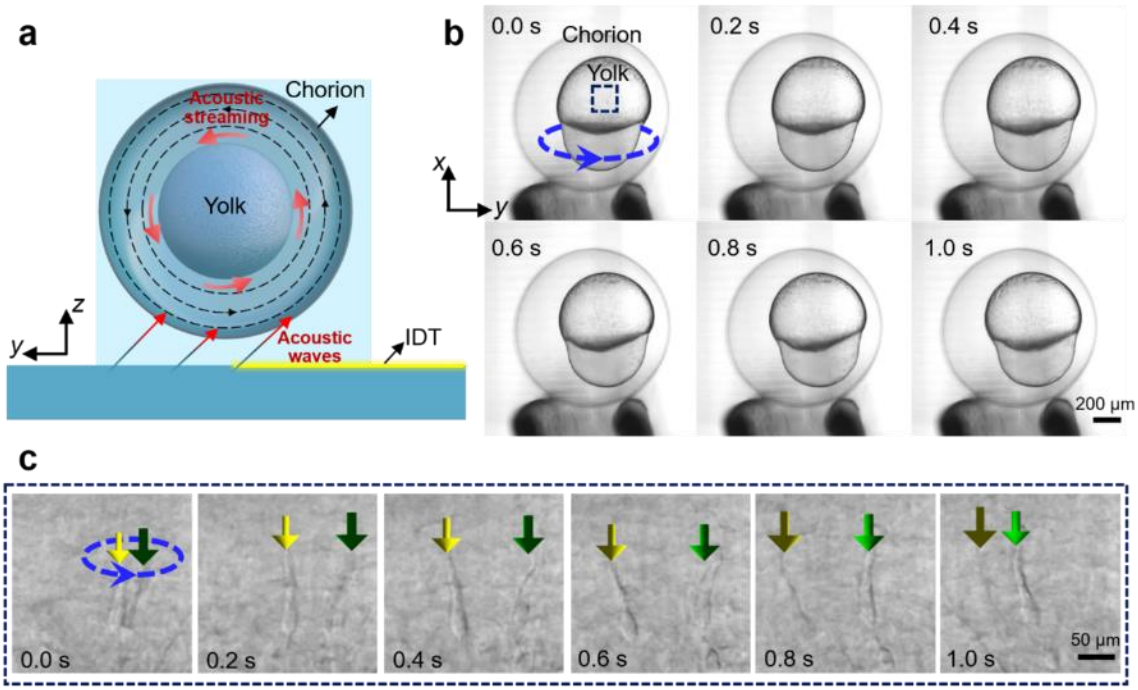

Figure 4.15: Rotation and imaging of a zebrafish embryo (0 dpf, prior to tail extension). a, Schematic showing the rotation of the yolk in the chorion achieved by leveraging acoustic streaming within the perivitelline fluid of the embryo. The acoustic leaky waves are transmitted through the chorion and generate acoustic vortex streaming in the perivitelline fluid within the chorion which rotates the yolk. b, A sequence of images capturing the rotation of the yolk of a ~0.2 hpf zebrafish embryo caused by the acoustic streaming in the chorion. c, Magnified images of the region within the black-dashed frame in (b), at each respective time step. The yellow and green arrows indicate and follow the movement of the end of two lines of the texture of the developing organism within the yolk, respectively. Five independent embryo rotation experiments (n=5) were used for rotation analysis. Representative embryo images from different angles were chosen to indicate the rotation motion. Scale bar: (b): 200 μm, (c): 50 μm.

4.6 Conclusion

In this chapter, we presented a unique design scheme which can generate single vortex acoustic streaming to rotationally manipulate zebrafish. This mechanism can create a strong single vortex acoustic streaming tube in millimeter-scale with high frequency (over 20 MHz) and low input voltage (~10 Vpp), which would be challenging for the

existing acoustofluidic platforms. In the existing acoustofluidic devices to generate single vortex streaming, the dimension of the single vortex would be difficulty to scale up due to the balance between the frequency and voltage (Collins, Ma, et al., 2017; Mao et al., 2017; Ozcelik et al., 2018) and the strong correlation between the vortex dimension and wavelength (Dentry, Yeo, & Friend, 2014). Our device designing scheme overcomes these difficulties of generating on-demand vortex streaming with previous acoustofluidic methods.

Notably, in our design scheme, a single vortex pattern with its center aligned in the middle of the channel cross-section can be generated for any size channel, as long as the "e = 0.5a" condition is satisfied (e: width of the effective IDT area, a: width of the channel; Figure 4.2). The vortex pattern extends along the channel for the distance of L (L: IDT length; Figure 4.2) and form a single vortex tube. In other words, following the "e = 0.5a" rule, the width and length of the single vortex tube can be adjusted by tuning the channel width (a) and the IDT length (L), respectively. Through numerical modeling, we validated that our acoustofluidic device can generate a "polarized" acoustic streaming single vortex with controllable parameters. Our results imply that larger or smaller channels could be designed to handle various types of organisms based on their sizes, and the single vortex acoustic streaming tube can be scaled accordingly to enable the acoustofluidic rotational manipulation of different model organisms (e.g., *Xenopus* embryo, *C. elegans*, mouse embryo, or shrimp).

Based on this design scheme, we fabricated the acoustofluidic rotational tweezing (ART) device and validated the streaming pattern generated in the device numerically and experimentally. In addition, we investigated the performance of the device on zebrafish rotation and optimized the actuation signals to achieve stable rotational manipulation of zebrafish larvae. This stable rotational manipulation function enables the observation of zebrafish larvae from multiple viewing perspective.

In the next two chapters, we demonstrated an ART platform with the functions of 3D rotational imaging, 3D model reconstruction, and quantification of morphological properties in zebrafish larvae on the basis of the rotational manipulation. In addition, we presented a proof-of-concept demonstration of using the ART system to phenotype the effects of acute alcohol exposure on zebrafish larvae.

5. ART System with 3D Multispectral Imaging and 3D Reconstruction

As demonstrated in the previous chapter, we developed the acoustofluidic rotational tweezing (ART) device which can achieve efficient, stable, and non-contact rotational manipulation to zebrafish larva. With this function, zebrafish larvae can be imaged from different view-points if mounting this device to the optical microscope platform. The morphology of the external body can be imaged by using the bright-field light source, and the internal systems (e.g., skeleton, organs, nerves) with fluorescent markers can be imaged by applying the appropriate fluorescent light source. In this way, the ART device enables 3D multispectral imaging of the zebrafish body and internal systems of interests from different perspectives of view. Furthermore, by leveraging the Silhouettes-based 3D reconstruction algorithms, 3D models of zebrafish larvae can be reconstructed based on the multi-view image sequence. Based on the 3D models, morphological properties in the zebrafish and the internal systems can be quantified for the phenotyping studies in a various of fields (e.g., chemical screening and drug development).

In this Chapter, we (1) present using the ART device for 3D multispectral imaging of zebrafish larva and (2) reconstructing 3D model of the zebrafish larval external body and internal organs. This chapter is organized as follows. Sections 5.1 introduces the motivation of the 3D multispectral imaging and 3D model reconstruction. Section 5.2 describes principle of utilizing the ART device for 3D multispectral imaging. Section 5.3

introduces the Shape-from-Silhouettes-based algorithm for 3D model reconstruction. Section 5.4 validates the accuracy of the 3D models reconstructed using the ART system and the customized algorithm. Lastly, a discussion and conclusion was given in Section 5.5. The work presented in this chapter has been published on *Nature Communications* (C. Chen et al., 2021).

5.1 Motivation

Zebrafish (Danio rerio) has been widely used as a model organism in human disease modeling and drug development studies (Adamson et al., 2018; Howe et al., 2017; Kari et al., 2007; MacRae & Peterson, 2015; J. L. Tan & Zon, 2011; Ward & Lieschke, 2002). In these studies, in which visualization and morphological analysis of the zebrafish phenotypes of interests are significant. To achieve these goals, 3D rotational manipulation technique is required to precisely orientate the zebrafish such that the zebrafish can be imaged more comprehensively.

With the development of modern genetic engineering technologies, zebrafish transgenic lines, which express fluorescent protein in specific classes of cells, tissues, or internal organs, are developed for research targeting at specific area in the zebrafish samples. The spectrally distinct fluorescent proteins expressed in the zebrafish tissues highlight and distinguish the targeted objects from the in neighboring tissues. Thus, by applying a bright-field light, the external morphology of the larval body can be visualized. And with the multispectral imaging, by applying appropriate fluorescent light sources,

the morphology of the internal systems (e.g., organs, skeletons, nerves) which have been tagged with fluorescent markers or genetically engineered to express fluorescent proteins can be visualized in vivo by using. With the rotational manipulation function, the ART system can be applied to 3D multispectral imaging of the zebrafish samples, in which the entire zebrafish and multiple fluorescently highlighted portions of the zebrafish can be observed from multiple viewing angles.

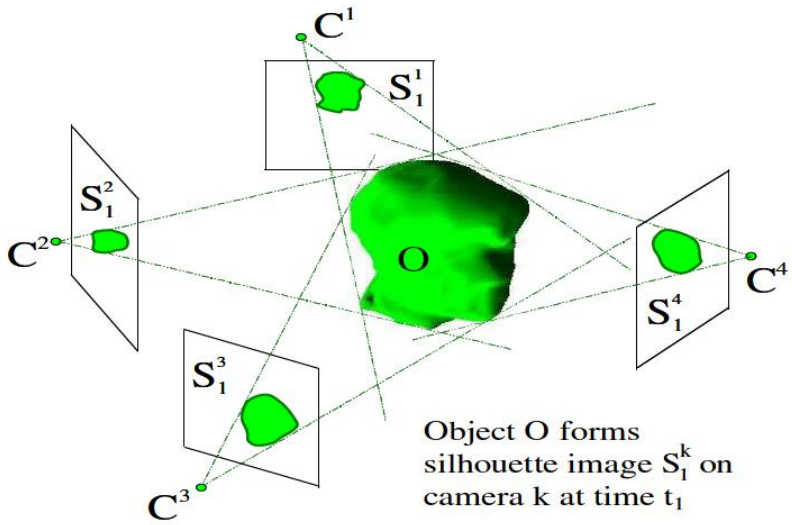

Figure 5.1: The Shape-From-Silhouette problem scenario. A head-shaped object $\boldsymbol{O}$ is surrounded by four cameras at time $\boldsymbol{t_1}$. The silhouette images and camera centers are represented by $\boldsymbol{S_j^k}$ and $\boldsymbol{C^k}$ respectively (Baker & Kanade, 2005).

Introduced by Baumgart, the computer-vision-based algorithm can be applied to reconstruct the image sequence of a certain object into a 3D model (Figure 5.1)(Baumgart, 1974). Thus, we further developed a computer-vision-based algorithm to reconstruct 3D models of the zebrafish and quantify the properties of interest as digital readouts for the zebrafish phenotyping studies. As shown in Figure 5.2, the ART platform was designed

to work in a flow-cytometry-like workflow. Each zebrafish larva was considered a "large particle" and was handled with the process of sample loading, rotational imaging, 3D model reconstruction from multi-angle images, quantification of the morphological abnormalities, sample unloading. By handling a group of samples, the ART platform can provide digital readouts for statistical analysis on the morphological characteristics of interest in the zebrafish phenotyping research. The goal of the developing the ART technique is to handle the zebrafish and provide quantitative data in a similar manner that the conventional flow cytometry deal with cells.

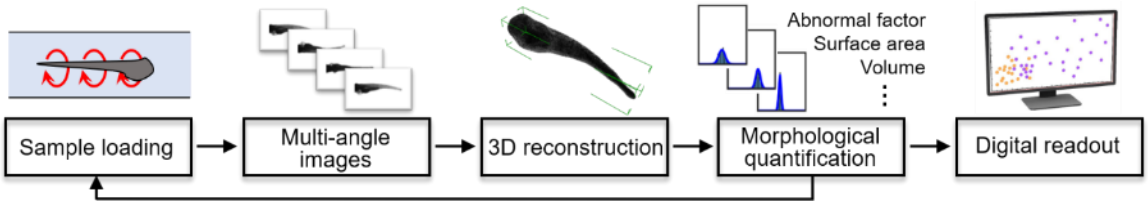

Figure 5.2: Cytometry-like workflow of the acoustofluidic rotational tweezing (ART) platform. For each sample, the platform performs the steps of sample loading, rotational imaging, 3D model reconstruction from multi-angle images, quantification of the morphological abnormalities, sample unloading. After handling all the samples in the group, the system provides digital readouts for zebrafish phenotyping studies.

5.2 3D multispectral imaging using the ART device

5.2.1 Zebrafish larvae preparation

The zebrafish (*Danio rerio*) transgenic line (2CLIP; *Tg(fabp10:DsRed; ela3l:GFP)*^{gz12}) was used for 3D multispectral imaging (Farooq et al., 2008). This transgenic line expresses green fluorescent protein in the pancreas and red fluorescent protein in the liver. Zebrafish (Danio rerio) studies were approved by the Institutional Animal Care & Use

Committee at Duke University (protocol # A154-18-06). All the experiments were performed on up to 5 days post fertilization (dpf).

Zebrafish embryos/larvae were cultured in egg water at 28°C and 14-hour light/10-hour dark conditions. The zebrafish larvae were anesthetized with 1× Tricaine (~0.2 mg/ml; Sigma, USA) during rotational manipulation. 1% Pluronic® F-127 surfactant (Sigma, USA) was added to the solution to improve the smoothness of the rotational motion. For 3D multispectral imaging of the internal organs, 0.003% 1-phenyl-2-thiourea (PTU, Sigma, USA) was added to the egg water to inhibit melanogenesis and to reduce the zebrafish skin melanization (Karlsson, Von Hofsten, & Olsson, 2001). After the process, the fluorescent signal of the internal organs can be observed more clearly.

5.2.2 3D multispectral imaging

During the 3D multispectral imaging, the ART chip is mounted to an upright microscope (BX51WI, Olympus). The optical images and videos are recorded using the microscope with a 2.5X objective lens (MPLFLN2.5X, Olympus), a CCD camera (CoolSNAP HQ2, Photometrics), and the CellSens 1.18 software (Olympus Corp., JPN). The zebrafish larvae are loaded to the ART chip for imaging. By applying a bright-field light, the external morphology of the larval body can be visualized. Expanding on this capability, if the larvae have been tagged with fluorescent markers or genetically engineered to express fluorescent proteins in certain portions of the internal systems (e.g., organs, skeletons, nerves), the fluorescent signals can be visualized *in vivo* by using

appropriate fluorescent light sources. The contour of the fluorescent area shows the distribution of the fluorescent markers or the morphology of the highlighted internal systems.

As shown in Figure 5.3, an anesthetized 2 CLIP (5 dpf) zebrafish larva, which expresses green fluorescent proteins in the pancreas and red fluorescent proteins in the liver, was loaded to the ART chip. The larval body, liver, and pancreas can be observed in the bright-field, dsRed fluorescent illumination, and GFP fluorescent illumination, respectively. By merging the optical images of the three light fields, the composite optical image shows the relative position of the liver and pancreas within the larval body.

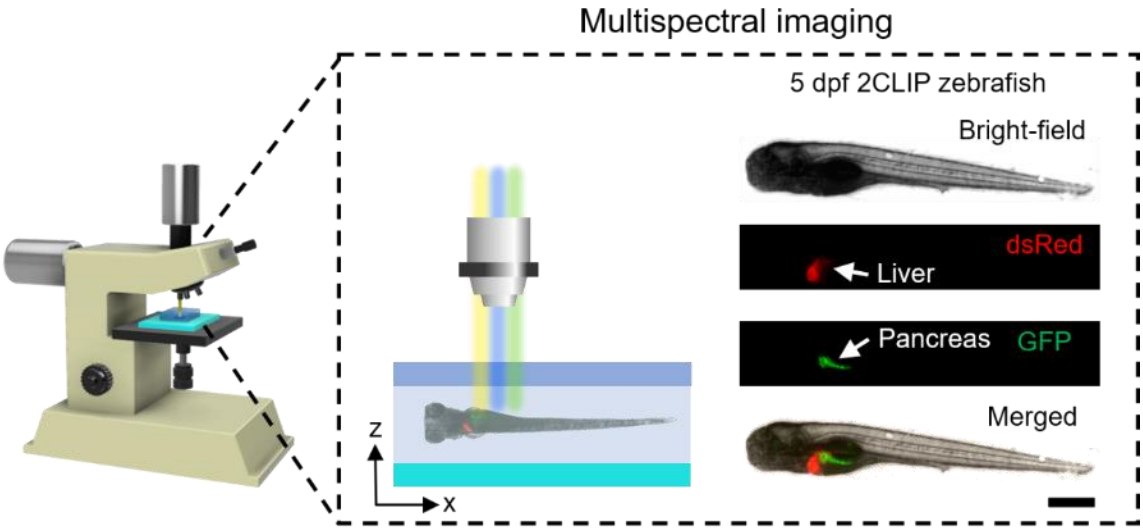

Figure 5.3: Multispectral imaging of a 5 dpf 2CLIP zebrafish larva. A 2CLIP zebrafish larva is imaged under a bright-field, dsRED fluorescent illumination, and GFP fluorescent illumination for the imaging of the body, liver, and pancreas, respectively. The merged optical microscopic image of the three light fields reveals the relative positions of the organs within the zebrafish body from the lateral view.

As demonstrated in the previous section, when the AC signals are applied to the interdigital transducer, surface acoustic waves are turned on. The single vortex streaming tube in the channel can trap and a zebrafish larva inside the channel and uniformly rotate it (Figure 5.4a). Thus, not only the multispectral image, but also the images at different viewing perspectives can be captured to show the morphology of the zebrafish larval body and highlighted internal systems more comprehensively. As shown in Figure 5.4b, with the stable rotational manipulation of the ART chip and the 3D multispectral imaging, 2D images from multiple axial-views of the zebrafish and its organs are captured. By merging the images from the same viewing angle, the composite optical images shows the relative position of the organs and larval body comprehensively.

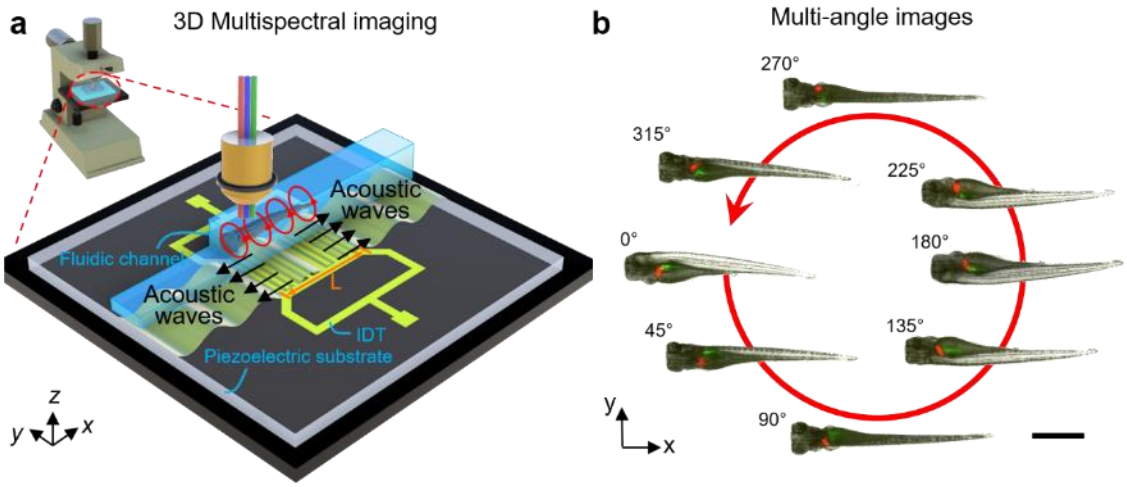

Figure 5.4: 3D multispectral imaging. a, Illustration of the experimental configuration of mounting the ART device to an optical microscope to perform 3D multispectral imaging. b, The composite optical images of the bright-field (body), DsRed (liver), and GFP (pancreas) images from different viewing perspectives. Scale bar: 1 mm.

5.3 3D model reconstruction

The ART with 3D multispectral imaging achieves the visualization of the larval body and internal systems with fluorescent proteins from multiple viewing perspectives. Based on the multispectral 2D images, we developed a 3D reconstruction method based on the shape-from-silhouette algorithm to reconstruct the assembled 3D models with internal organs and larval body. The assembled 3D models provide the location and shape of the body and internal organ structure, as well as comprehensive quantitative data of the morphological characteristics in each section (Figure 5.5).

5.3.1 Camera matrix

One of the most important parameters in the 3D reconstruction is the determination of the camera matrix which connects the 3D coordinates in the real world with the 2D position in the image. The classic camera matrix can be denoted as: $P = K[R|t]$, $K_{3\times3}$ is the camera intrinsic matrix that contains the camera configuration itself as:

$$K = \begin{bmatrix} f_x & s & x_0 \\ 0 & f_y & y_0 \\ 0 & 0 & 1 \end{bmatrix}$$

where $(f_x \;\; f_y)$ is the focal length in pixels that can be derived as: $f_x = f/dx$ and $f_y = f/dy$, dx, dy are the length of the single pixel in the image, $(x_0 \;\; y_0)$ is the image center, and s is the shear factor of the camera. It can be decomposed into three matrixes as:

$$\begin{bmatrix} f_x & s & x_0 \\ 0 & f_y & y_0 \\ 0 & 0 & 1 \end{bmatrix} = \begin{bmatrix} 1 & 0 & x_0 \\ 0 & 1 & y_0 \\ 0 & 0 & 1 \end{bmatrix} \times \begin{bmatrix} f_x & 0 & 0 \\ 0 & f_y & 0 \\ 0 & 0 & 1 \end{bmatrix} \times \begin{bmatrix} 1 & \frac{s}{f_x} & 0 \\ 0 & 1 & 0 \\ 0 & 0 & 1 \end{bmatrix}$$

which correspond to the 2D translation, scaling, and shear, respectively. $[R|t]$ serves as the extrinsic matrix including the rotation matrix and the translation matrix, which can be referred to as the camera motion in 3D. The rotation matrix R can be decomposed into the rotation components along three axes: $R_{3\times3} = R_X \times R_Y \times R_Z$ where, for our case, the rotation angle of the x-axis is changing with different frames during rotation. And the 3D translation vector t can be parametrized as $t_{3\times1} = [0, fcos(\varphi), fsin(\varphi)]^T$ following the general definition.

5.3.2 3D reconstruction pipeline

The digital reconstruction pipeline is briefly summarized as the following six steps. (1) Capture the background image in an empty channel before the zebrafish enters, then load the zebrafish and record a sequence of images for one rotation cycle corresponding to an angle θ from 0 to 2π. (2) Perform preliminary image processing by subtracting the background image from the series of rotational images, which digitally and visually isolates the segments of the zebrafish. (3) Binarize the image series to obtain the 2D silhouettes (Figure 5.5b). (4) Initialize a 3D grid of voxels according to the 2D silhouette's boundary and size. (5) Back-project the 2D profiles into the 3D framework from the outside "world perspective" and obtain the matching intersections. (6) From this point, we can generate a watertight 3D visual "hull" of the target object (Figure 5.5c). Note that although our experimental configuration is different from the common camera system for applying SFS (a moving object vs a moving camera), the tensor describing the

camera frame of reference (i.e., the camera matrix) can be considered identical since the camera center is defined as the world origin. Thus, the relationship between the 2D image and 3D coordinates in the real world can be expressed as: $a_n = K[R_n|t]A_n$, where a_n, A_n are corresponding 2D and 3D coordinates, K is the intrinsic matrix of the camera, and $[R_n|t]$ is the extrinsic matrix which can be divided into a rotation matrix R_n and a translation matrix t. Here, n denotes the nth visual angle that relates to the rotation angle of the zebrafish.

The series of images captured using the three illumination fields are recorded sequentially and then angularly aligned to obtain one composite series of images. The angular alignment is achieved by recording one extra image of the fluorescent fields with a slight overexposure, such that the outline of the zebrafish can be identified and matched with the corresponding angular perspective of the respective bright field image. Then, the fluorescent image series are aligned starting from the angle corresponding to the extra matching image. After the fusion of the three illumination fields, the 3D multispectral model is calculated using the same camera matrix, and the size of each voxel of the organs (*i.e.*, liver and pancreas) is set to be 5 to 10 times smaller than the whole body to achieve a finer reconstruction resolution.

For a single zebrafish 3D reconstruction, images with the total frame number ranging from 15 to 31 are used. The differences in the total number of frames depending on the individual differences in zebrafish (e.g., each zebrafish has a slightly different

rotational velocity). Each 2D image has a resolution of 2048x2048 pixels which corresponds to a field of view of ~5.33x5.33 mm^2 for the whole image. The end of one rotation cycle is determined by identifying the frame i that has the minimum difference with the first image: $i|_{\theta=2\pi} = \arg\min\,(\|a_i - a_1\|)$. After the number of the frames N in one cycle is determined, the rotation angle can be estimated by $\theta_i = 2\pi(i-1)/N$ as the acoustofluidic device generates a stable rotation with a constant angular velocity for each zebrafish. A photomask is designed with a checkerboard pattern to obtain an accurate camera intrinsic matrix. By taking multiple images of the photomask at different orientations, the camera intrinsic matrix can be calibrated using the camera calibrator toolbox in MATLAB R2016b (MathWorks, USA). Once the camera model parameters are identified, a representation comprised of 3D volumetric voxels can be reconstructed from the 2D binary axial-view images by intersecting all the voxels whose 2D projection is covered by the silhouettes: $V = \bigcap_{i=1:N} v_i$, $v_i = \{A(x,y,z)|S_i(a'_i) \neq 0; a'_i = P_i A'_i\}$, where A'_i is the 3D coordinates of the initial voxels, a'_i is the 2D projection of the initial voxels in ith viewpoint, P_i is the camera matrix in the ith viewpoint, S_i denotes the approximation function determining whether the 2D projection of the voxels is within the silhouettes image. Then the marching cubes algorithm is used to generate a "watertight" surface with a dense point cloud and triangulated meshes from the reconstructed 3D voxel sets. Moreover, for the batch reconstruction process of the image flow model, optimization of the camera matrix is conducted by detecting and updating the translation vector t and

the region of interest (ROI) since the zebrafish may rotate in a position that has slightly shifted from the center of the image. For this case, a frame of the ROI is defined as a square region with a minimum side length that can cover the segments in the image series and the center of the ROI serves as the center of the zebrafish or of its organs. MeshLab 2016.12 (Cignoni et al., 2008) and SolidWorks 2016 (SolidWorks Corp., USA) are used for 3D model texture mapping, rendering and visualization. The 3D reconstruction is implemented using Matlab programming on a desktop with an Intel i7 CPU and 64GB RAM. The runtime for the program to reconstruct a 3D model depends on the total number of image frames. It ranges from 7.97 s to 10.40s for a zebrafish body reconstruction and 12.44s to 17.34s for an organ, excluding the time to digitally save the .STL file (3D model). The data were visualized as curves, histograms, and scatter plots by OriginLab 2018 (OriginLab Corp., USA).

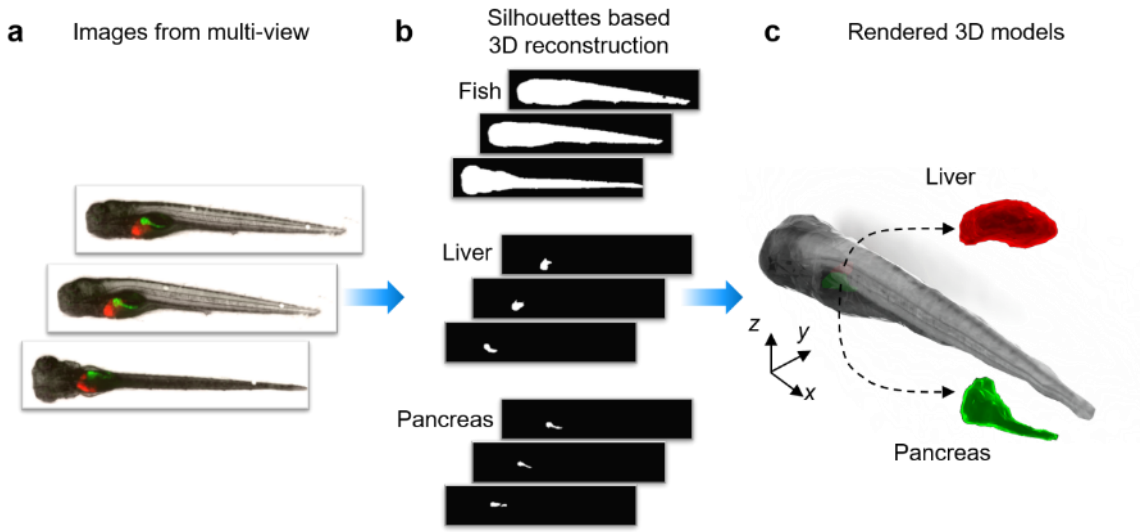

Figure 5.5: Silhouettes based 3D reconstruction. a, The multi-view and multispectral images of a 5 dpf 2CLIP zebrafish larva. b, 2D silhouettes of the fish body, liver, and

pancreas obtained by binarizing the optical images. c, A rendered 3D model with fish body, liver, and pancreas.

5.4 validation of the accuracy of the 3D models

With the abovementioned SFS 3D reconstruction methods, we are able to generate assembled 3D models of the zebrafish larvae. In this section, we evaluated the accuracy of the 3D models to verify the reliability of our 3D reconstruction method.

5.4.1 Zebrafish larvae models

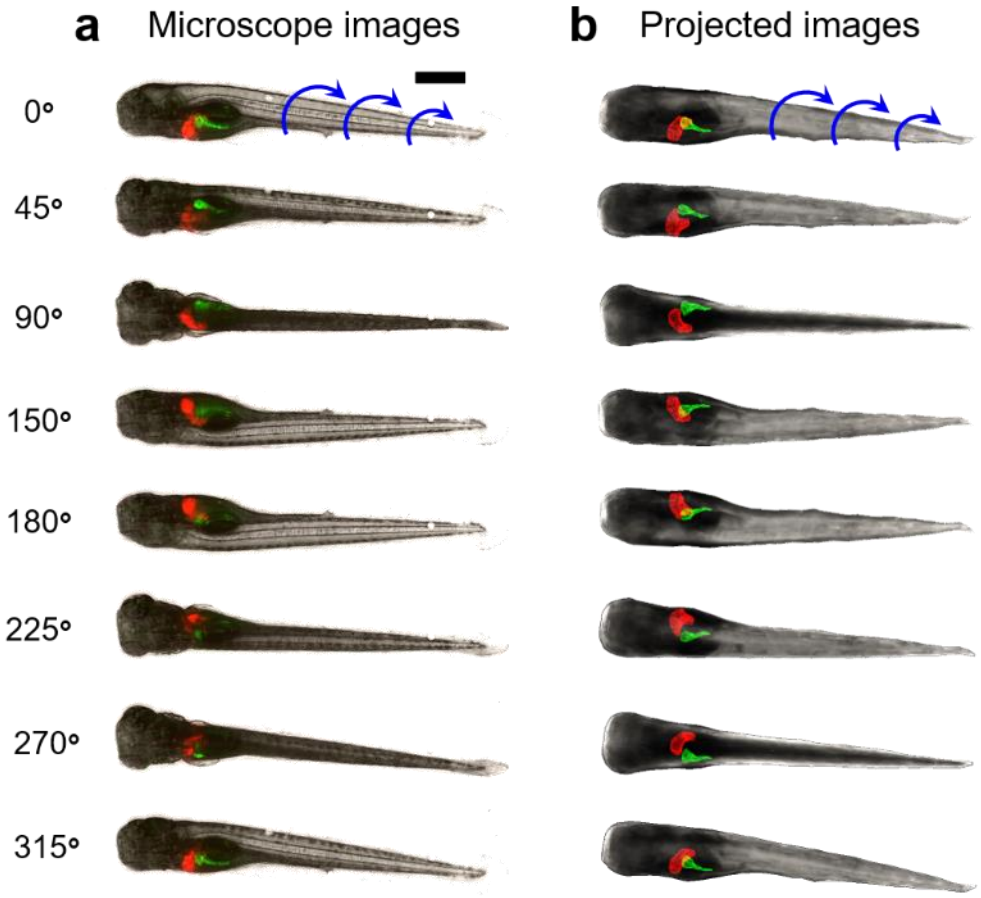

Figure 5.6: Comparison between the optical microscope image sequence and projected 3D model images at the corresponding viewing angles. Scale bar: 500 μm.

For validation, first, we compared the projected images of the reconstructed 3D model with multispectral microscope images at the corresponding viewing orientations. As shown in Figure 5.6, no obvious differences between the optical images and projected images were tell based on visual comparison.

Hough transform quantify the major features in the 2D images by plotting the angles (θ) and corresponding norms (ρ) of the small features in the image in the x- and y-axis, respectively. It is commonly used in computer vision to quickly find differences in similar images. For further validation, the correspondence of the projected images of the 3D model and optical image at the corresponding viewing orientation was evaluated quantitatively by comparing their Hough transforms. For example, as shown in Figure 5.7, no obvious difference was observed between the Hough transform plots of the merged optical image and projected image of the assembled 3D model. This result verifies the consistence between the reconstructed 3D model and the optical images of the real zebrafish larva.

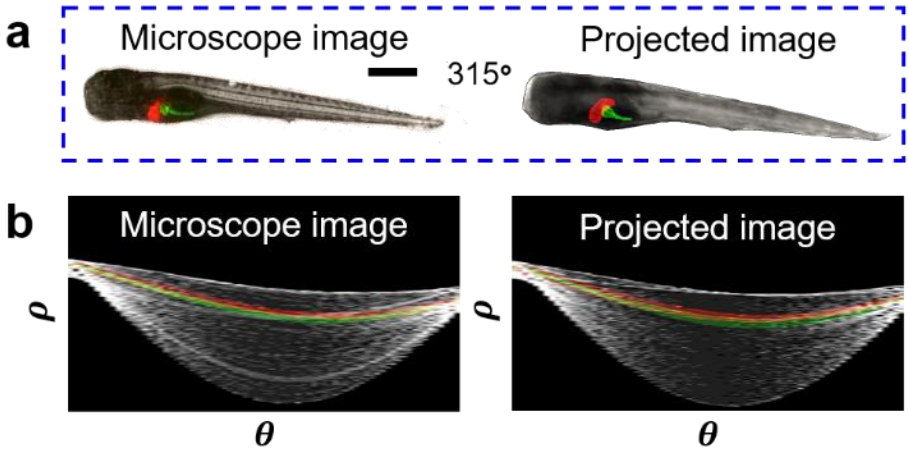

Figure 5.7: Comparison between the Hough transform plots of the features of the microscope image and the projected image at 315° in Figure 5.6. Scale bar: 500 μm.

To further quantify the accuracy of the reconstructed 3D model from a three-dimensional point of view, the binary cross-entropy loss was calculated to evaluate the variance of the 3D model from all viewpoints. First, the 3D point clouds of the 3D model were re-projected back to the 2D planes from different viewpoints to get the re-projected 2D points. The cross-entropy loss of one viewpoint is calculated by identifying if the re-projected 2D points on a viewpoint are also present in the original 2D silhouette of the corresponding microscope images: $\mathcal{L}_i = 1/N \sum_1^N \ell_{0-1}(p, \hat{p})$, where N is the number of the re-projected 2D points; p and $\hat{p}$ are 2D points in silhouette and the re-projected image, respectively; and $\ell_{0-1}(p, \hat{p})$ indicates whether the loss function (ℓ) is either 0 or 1 (the loss function is equal to 0 if the re-projected point is also found in the silhouette image, and not present for a value of 1). Then, the total binary cross-entropy loss of the whole 3D

model is calculated as the average from all viewpoints: $L = 1/fn \sum_{1}^{fn} \mathcal{L}_i$, where fn is the number of frames/viewpoints.

Figure 5.8 shows the binary cross-entropy loss which three-dimensionally quantifies the accuracy of the 3D model in Figure 5.6. It was calculated by comparing optical microscope images in Figure 5.6a and the corresponding re-projected images of the 3D reconstructed point clouds from different viewing angles for the larval body, liver, and pancreas. This quantitative validation indicated that the re-projections from our 3D model reconstructed using our method had a >90% level of fitting compared to the original images. Based on these results, we verified that our 3D reconstruction method can generate 3D models which can (1) accurately provide the 3D shape and the relative position between the body and the internal structures of interest and (2) quantify the morphological characteristics (profile, volume, surface area, etc.).

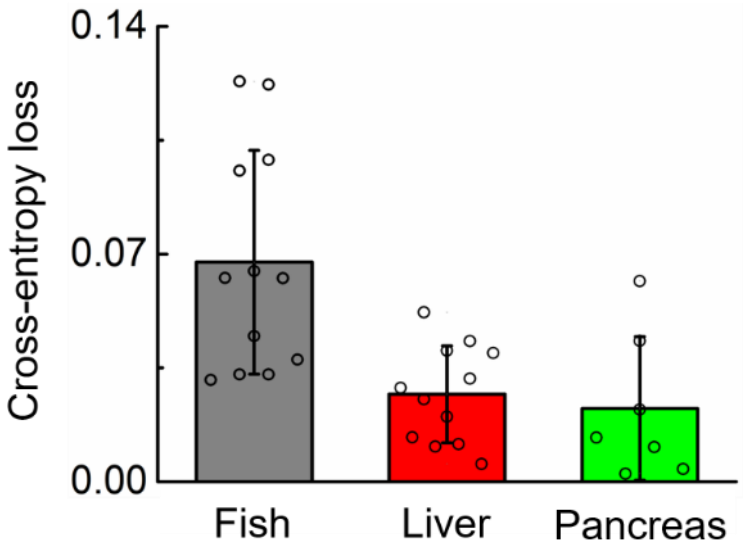

Figure 5.8: The binary cross-entropy loss for 3D reconstructed models of zebrafish larvae, livers, and pancreases. The binary cross-entropy was calculated by comparing optical microscope images and the corresponding re-projected images of the 3D reconstructed point clouds from different viewpoints. n=12 for fish body and liver, n=7 for pancreas. Data are graphed as the mean ± SD.

5.4.2 Zebrafish yolk models

In addition, we performed the rotational imaging and 3D reconstruction of a zebrafish embryo to validate the reliability of our 3D reconstruction method. Figure 5.9a shows an optical image of a quasi-spherical yolk with a radius of 354.03-μm. This yolk is rotationally imaged and reconstructed using the ART system. Owing to its relatively regular geometry, the volume (V) and surface area (SA) of a yolk (prior to tail extension) can be estimated as a sphere with V = 1.86×10^8 μm^3 and SA = 1.57×10^5 μm^2, respectively (Figure 5.9b). The volume and surface area measured based on the 3D model reconstructed using our algorithm (V=1.87×10^8 μm^3 and SA=1.59×10^5 μm^2) is similar to

that of the spherical estimation. This results imply that the ART system with multispectral imaging and 3D reconstruction algorism is reliable to provide quantitative evaluations.

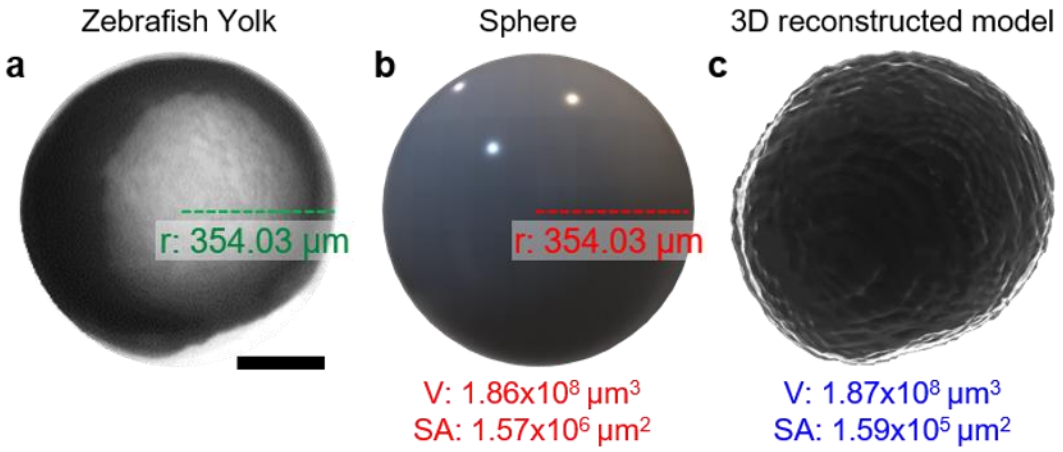

Figure 5.9: Validation of the 3D reconstruction by reconstruction and size evaluation of a zebrafish yolk. a, An optical image of a quasi-spherical yolk. b, A sphere with a similar radius to the yolk in (a). The volume and surface area were calculated to be 1.86×10^8 μm^3 and 1.57×10^6 μm^2, respectively. c, The 3D reconstructed model of the yolk in (a). The volume and surface area of the 3D reconstructed model was evaluated to be 1.87×10^8 μm^3 and 1.59×10^5 μm^2, respectively, which are close to the estimated values computed from the shape of the sphere in b. Representative image set of the projected images is from three independent reconstruction calculation (n=3). Scale bar: 200 μm.

5.4.1 Zebrafish liver models

As an additional validation, we conducted a study in which we reconstructed five 3D models of a 5-dpf larval liver based on image sequences captured during five different rotation cycles using our 3D reconstruction algorithm. As shown in Figure 5.10, when projected from the same viewing angle, the projected images of the five 3D models yielded similar contours. In addition, the volume and surface area of each model was evaluated and compared. The mean standard deviations of the volume and surface area were

calculated to be 6.5003±0.0618 (x10^5 μm^3) and 1.5803±0.1286 (x10^4 μm^2), respectively (Figure 5.10). The small STD indicates that the reconstructed model is consistent between different rotation cycles and our ART system with multispectral imaging and 3D reconstruction algorism is reliable.

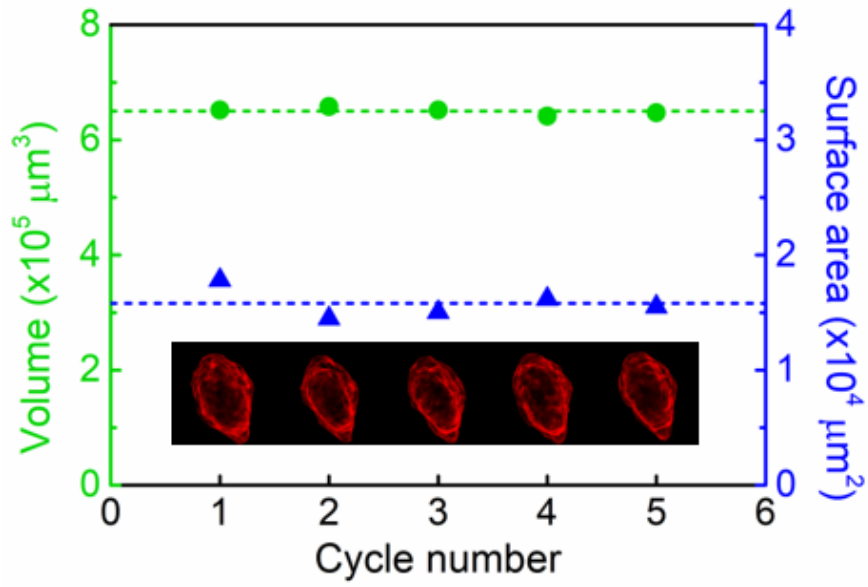

Figure 5.10: 3D reconstruction of the same liver based on image sequences captured in five rotation cycles.

5.4.1 Conclusion

The results of the abovementioned three validation studies proof that (1) the ART system with multispectral imaging can provide stable rotational manipulation for zebrafish larvae, and (2) 3D reconstruction method we customized for the ART system can precisely and accurately generate 3D models. These 3D models can provide qualitative and quantitative 3D data for zebrafish phenotyping research.

5.5 Discussion and conclusion

Considering the size of the objects to reconstruct, the dimensions of the pixel volume used for zebrafish body and organ reconstruction were set as 20×20×20 μm^3 and 5×5×5 μm^3, respectively. In the zebrafish larvae's body, the dimensions of cross-section gradually shrink along the body. As a result, selecting a larger pixel size for body reconstruction may induce a roughness artifact to the zebrafish tail. This could be optimized by applying a smaller pixel volume or using pixels with variable dimensions along the body. In order to achieve continuous and rapid phenotyping of a large population of zebrafish samples, a tradeoff was made between the precision of model and the speed of 3D reconstruction speed.

The accurate 3D reconstruction requires uniform rotational manipulation. Any uneven rotation angle between each video frame would affect the resulting 3D reconstruction. As the corresponding angles are related to the camera matrix that was used to determine the isosurface of the 3D model, any rotational non-uniformity corresponding to an incorrect estimate for the image angle will cause distortions in the 3D model. As mentioned in Section 4.5.2, the optimal acoustic voltage (~12.75 V_{PP}) was used to generate a strong acoustic streaming and sufficient drag force to overcome the inertia of the zebrafish. This activation generates a stable rotation mode in which the force torque would be zero. And, since angular momentum is conserved, this optimal acoustic voltage results in uniform rotation.

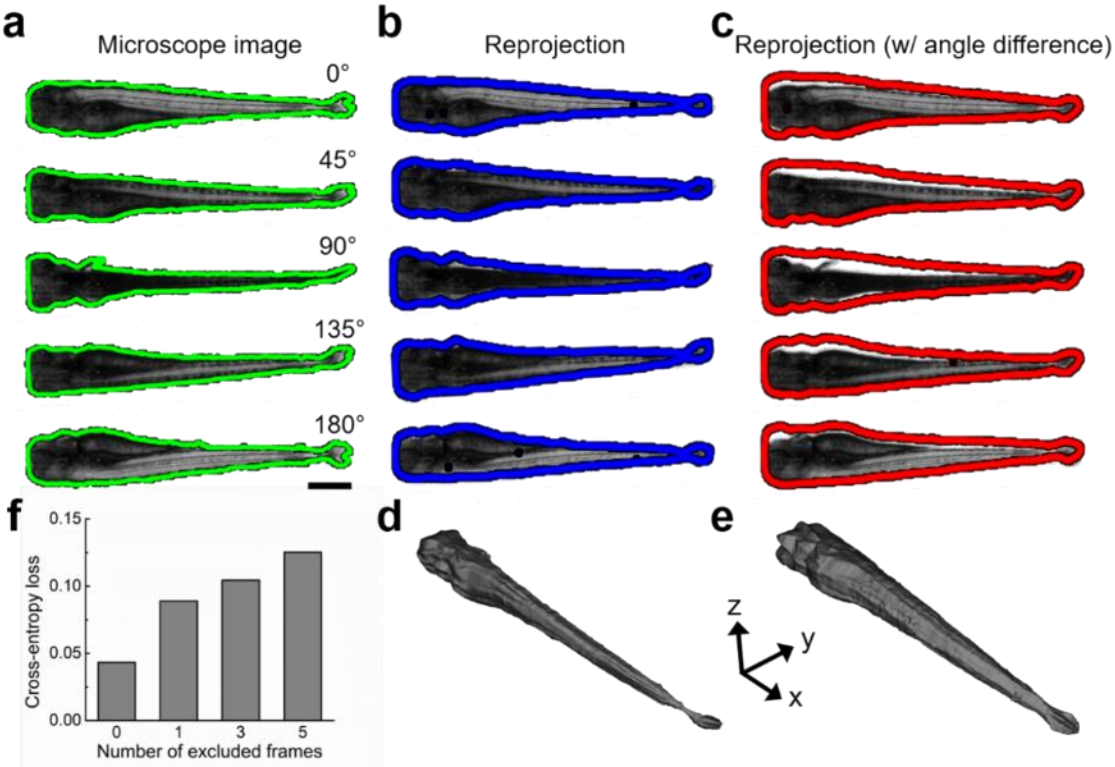

Figure 5.11: Comparison of the silhouette outlines between the microscope images, digital re-projection images, and the re-projection images with a known uneven angle distribution. a-c, The outlines of different re-projection cases as compared with the actual microscope images. d, The 3D model of the zebrafish reconstructed from the original image stack. e, The 3D model of the zebrafish reconstructed from video with frame removed in order to demonstrate angle unevenness. f, The relationship between the cross-entropy loss with respect to the number of the missing frames, as a measure of rotational uniformity.

Here, we used a proof by contradiction to show that the ART system can achieve rotational manipulation with relatively uniform rotation angle. Specifically, we firstly assumed the angle is uniform and reconstructed the 3D zebrafish model. Then the 2D digital re-projection can be calculated for different angles. If the re-projection matches with the microscope images at the corresponding angles, this 3D model can be considered

as accurate and also proves the angle information used were correct. As shown in Figure 5.11, we compared the outlines of the image silhouettes for three different cases. The green contours in Figure 5.11a are the outlines of the microscope images. The blue contours in Figure 5.11b, which are the outlines of the re-projection, match with the contours of the microscope images at the corresponding viewing angles. In order to demonstrate the effect of incorrect angular alignment, we recorded a video of one rotation cycle and deleted several continuous frames in order to mimic an uneven, non-uniform rotation. As shown in Figure 5.11c, using the video with five excluded frames, we reconstructed a new 3D model using the original angular setup (Figure 5.11e), and the outlines of the silhouette show an obvious difference compared to the microscope zebrafish images. In comparison, the re-projection from the original 3D model (Figure 5.11d) indicates a proper match to the microscope images. We also quantified the effect of the angle differences by calculating the cross-entropy loss for different numbers of excluded frames (Figure 5.11f). The result indicates that without the excluded frames (uniform rotation motion in the system), the loss is 0.04 which means, on average, the digitally re-projected image has a 4% error compared to the microscope image. When one frame is excluded, the angle information becomes uneven, thus, the loss has increased about ~2 times and is above the average loss shown in Figure 3 in the manuscript. With more excluded frames, the degree of the angle unevenness becomes larger and the loss is increased, correspondingly. This

result, although obtained indirectly, indicates that the digital reconstruction is relatively consistent with the microscope image and the rotation speed is relatively uniform.

In this chapter, we have integrated the ART chip with the optical microscope and a customized 3D reconstruction algorithm. With all these units, the ART platform achieves stable and uniform rotational manipulation to zebrafish larva, 3D multispectral imaging of larval body and internal systems with fluorescent signals, and accurate 3D model reconstruction. With the accurate 3D models, the ART system possesses the potential to provide qualitative and quantitative 3D data for zebrafish phenotyping research. In the next chapter, we first demonstrated methods to quantify the morphological properties of the zebrafish larvae based on the 3D models. Then, we incorporated a semi-automatic flow system to the ART platform which enables successive processing a large amount of zebrafish samples. Then, we performed a proof-of-concept demonstration by phenotyping a 5 dpf zebrafish larvae using the ART system.

6. Zebrafish Phenotyping Using the ART Platform

As mentioned in Chapter 4 and Chapter 5, we develop a 3D reconstruction pipeline that yields accurate 3D models based on the multi-view images for quantitative evaluation of basic morphological characteristics and advanced combinations of metrics. In this chapter, we expand the capability of the ART platform by incorporating a semi-automatic flow system and developing a method to quantify the morphological properties based on the 3D models. This improvement enables high-throughput zebrafish 3D multispectral imaging and quantitative evaluation for the phenotyping studies.

In Chapter 6, we demonstrated high-throughput quantitative phenotyping using the ART platform. Sections 6.1 introduces the motivation of the development of this platform. Section 6.2 presents the methods of the flow system, zebrafish sample preparation, and zebrafish health assessment. Section 6.3 and Section 6.4 demonstrated using the ART system to phenotype the zebrafish larval body shape and liver size, respectively. Lastly, a discussion is given on the comprehensive capabilities and performance of the ART system. The work presented in this chapter has been published on *Nature Communications* (C. Chen et al., 2021).

6.1 Motivation

The zebrafish (*Danio rerio*) has been broadly used for the phenotyping studies in the medical, biological, and pathological research fields (Howe et al., 2017; MacRae & Peterson, 2015). Owing to the high reproduction rate and large number of progeny from

zebrafish, large-scale phenotyping-based studies can be rapidly performed on sufficiently amount of samples to obtain statistically significant and reliable conclusions (Arifin & Zahiruddin, 2017). As vertebrate model organism, zebrafish have highly functional and comprehensive organ systems with a high degree of genetic and functional similarity to humans. These characteristics make zebrafish the preeminent subject for human disease modeling and *in vivo* chemical screening for small molecule drugs discovery (Kari et al., 2007; MacRae & Peterson, 2015; J. L. Tan & Zon, 2011; Ward & Lieschke, 2002). These studies require (1) visualization of a large number of zebrafish samples and (2) quantitative evaluation of the morphological properties of interest to generate accurate phenotyping results. Thus, we sought to develop an acoustofluidic rotational tweezing (ART) platform that integrates the functions of (1) acoustic-based contactless rotational manipulation, (2) multi-view multispectral imaging, (3) 3D model reconstruction and quantitative evaluation of morphological abnormalities, and (4) phenotypic analysis based on quantitative reference standard for batches of zebrafish larvae.

6.2 Methods

In this sub-section, we introduce the setup of the ART system with a semi-automatic flow system and the routine use of this system for zebrafish phenotyping. To evaluate the biocompatibility of routine use of the ART platform, the viability checks were performed by evaluating the health of the zebrafish sample.

6.2.1 Flow system

To continuously process a group of zebrafish larva, we developed a semi-automatic flow system for sample loading, rotational imaging, and unloading. The ART chip used in this continuous flow mode is shown in Figure 6.1.

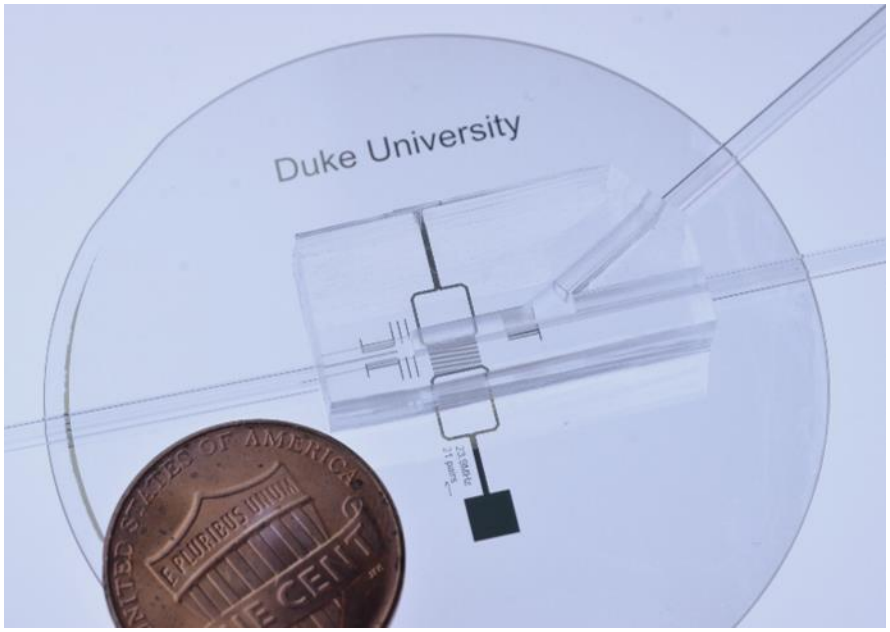

Figure 6.1: A photo showing the assembled ART chip for zebrafish phenotyping.

This ART chip contains a Y-shaped channel with three branches. The ends of the capillaries in each branches were connected to flexible silicone tubing with a 1.59-mm inner diameter (EW-06411-62, Masterflex, USA). As shown in Figure 6.2, end of the tubing connected to branch "C" was connected to a 10-ml syringe (302995, BD Medical, USA) mounted to a syringe pump (78-8210, KD Scientific, Inc., USA). The syringe pump controls the flow direction to load the zebrafish samples from the inlet (branch "A") or unload the zebrafish samples from the outlet (branch "B"). The tubing connected to the branches "A"

and “B” were mounted to a three-way pinch valve (98302-42, Cole-Parmer, Inc., USA) The two channels of the valve is one normally open, one normally closed. Thus, the flow in one branch of either “A” and “B” was blocked when the sample passed through the other branch. The motion of the pump and the valve was controlled by a programmable Arduino board (Elegoo, UNO R3).

The semi-automatic flow system contains three pre-programmed modes of sample loading, rotational imaging, unloading. The status of the syringe pump and three-way valve in each mode are shown in Figure 6.2 and Table 6.1. The acoustic waves are active during the entire process and the switching between the operating modes of the flow system was performed manually. In the sample loading mode, the pump withdrew the sample from the inlet while the valve was set to the status of A-open/B-closed. We manually directed the end of the tubing at inlet towards a zebrafish at the beginning of the sample loading process to improve the sample loading efficiency. When the sample reached the imaging area, the pump was stopped so that the sample can stay in the IDT area and be rotationally imaged. After the sample was imaged, the status of the three-way valve was switched to A-closed/B-open mode so that the pump can dispense the fluid and sample through the outlet to a container with fresh DI water.

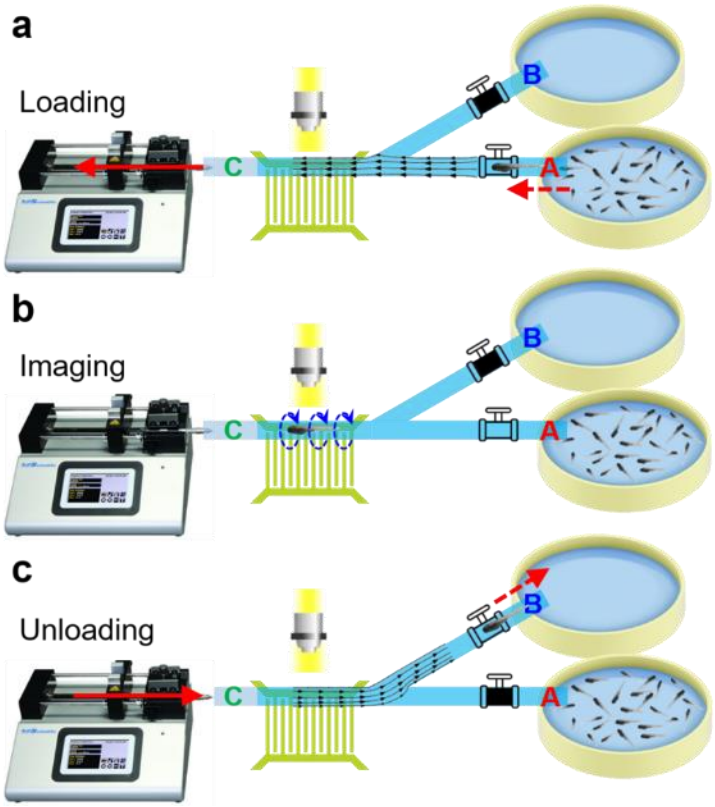

Figure 6.2: Schematic representation of the operating modes of the flow system. Two valves are illustrated for flow clarification only. a, Sample loading mode b, Rotational imaging mode. c, Sample unloading mode.

Table 6.1: Status of the acoustics, syringe pump, and valve in each mode of the flow system.

Mode	Acoustics	Pump	Valve
Loading	On	On, withdraw	A-open/B-closed
Imaging	On	Off	A-open/B-closed
Unloading	On	On, push	A-closed/B-open

Table 6.2: Average time of each step. * Each time and standard deviation are averaged from n=20.

Step	Time ± s.d.* (s)
Loading	5.5 ± 0.6
Rotation and imaging (1 cycle)	1.3 ± 0.3
3D reconstruction (body and organs)	39.6 ± 5.1
Unloading	2.9 ± 0.6

6.2.2 Zebrafish larvae preparation

The zebrafish (*Danio rerio*) transgenic line (2CLIP; *Tg(fabp10:DsRed; ela3l:GFP)*^{gz12}), which expresses green fluorescent protein in the pancreas and red fluorescent protein in the liver, was used for the zebrafish phenotyping studies in this chapter (Farooq et al., 2008). Zebrafish (Danio rerio) studies were approved by the Institutional Animal Care & Use Committee at Duke University (protocol # A154-18-06). All the experiments were performed on up to 5 days post fertilization (dpf).

Zebrafish embryos/larvae were cultured in egg water with 0.003% 1-phenyl-2-thiourea (PTU, Sigma, USA) at 28°C and 14-hour light/10-hour dark conditions. The PTU inhibits melanogenesis so that the pigmentation on the zebrafish skin can be reduced for clearer imaging of the fluorescent signal in the internal organs (Karlsson et al., 2001). For ethanol (EtOH) exposure, the zebrafish larvae in the experimental group were moved to egg water containing 1.5% EtOH at 4 dpf and cultured for 24 hours.

During the rotational imaging, zebrafish larvae were moved to DI water containing 1× Tricaine (~0.2 mg/ml; Sigma, USA) and 1% Pluronic® F-127 surfactant

(Sigma, USA) in order to anasthetize the sample and improve the smooth of the rotational manipulation. The immersion time of the zebrafish larvae in this solution is ~3 minutes (Table 6.2).

6.2.3 Assessment of zebrafish health

We preformed the viability checks to evaluate the biocompatibility of routine use of the ART platform, which contains the sample loading, three cycles of rotational imaging, and sample unloading (Figure 6.1). The maximum processing time for each step are 6.1 s, 12.9 s, and 3.5 s, respectively. Thus, the total processing time of each zebrafish larvae based on the routine use of the ART platform is less than 22.5 s. During the experiment, each time we moved 10 zebrafish larvae to a container with solution contains 1× tricaine (0.2 mg/ml) and 1% Pluronic® F-127, performed the rotational imaging to them one by one, and collect them in another container with DI water after imaging. In this routine process, the immersion time of the zebrafish larvae in this solution is ~3 minutes.

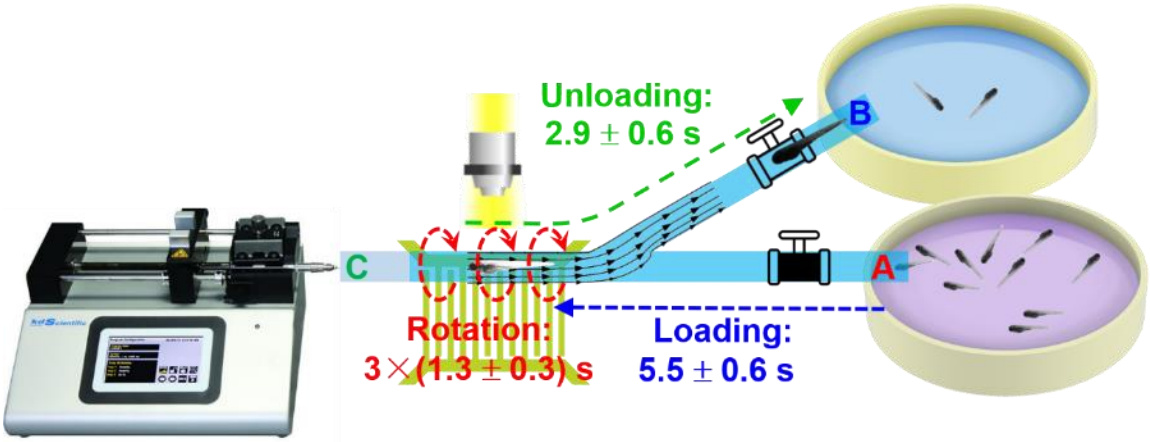

Figure 6.3: The processing time of the routine use of the ART platform for zebrafish 3D multispectral imaging. The maximum processing time for the sample loading, rotational

imaging in three different light fields, and sample unloading are 6.1 s, 12.9 s, and 3.5 s, respectively.

In the viability checks, we assessed the health of the zebrafish larvae in three groups of 50 2CLIP zebrafish larvae (Figure 6.4). The three groups of the zebrafish samples were treated as follows at their 2 dpf: (1) Group 1 (control group): 1× Tricaine for 5 min; (2) Group 2: 1× Tricaine + 1% Pluronic® F-127 for 5 min; (3) Group 3: 1× Tricaine + 1% Pluronic® F-127 for 5 min, and rotational imaged using the ART system for 30 s during this immersion time (Figure 6.4a). After the treatment, we collected the zebrafish larvae in cell strainers, gently rinsed them with fresh DI water, and cultured them for 48 h. At their 4 dpf, we evaluated the morphological appearance, survivability, response to touch stimuli, swim bladder appearance, and heartbeat of the zebrafish samples to assess their health.

From the visual observation of the morphological appearance, no abnormalities in body bending were observed in all the groups. As shown in Figure 6.4b, c, the survival rate, touch response, swim bladder appearance at 4 dpf, and heart rate in the Group 2 and Group 3 matched those of controls. The result of the health assessment shows that neither 5-minutes immersion in 1% Pluronic® F-127 nor 5-min immersion in 1% Pluronic® F-127 and 30-seconds rotational imaging using the ART platform causes obvious harmful effects to 2 dpf zebrafish larvae. Considering that the total time of the solution immersion and the rotational imaging in these viability tests is longer than our routine process, the health

assessment demonstrates that the routine use of the ART system does not cause obvious harmful effects to zebrafish larvae.

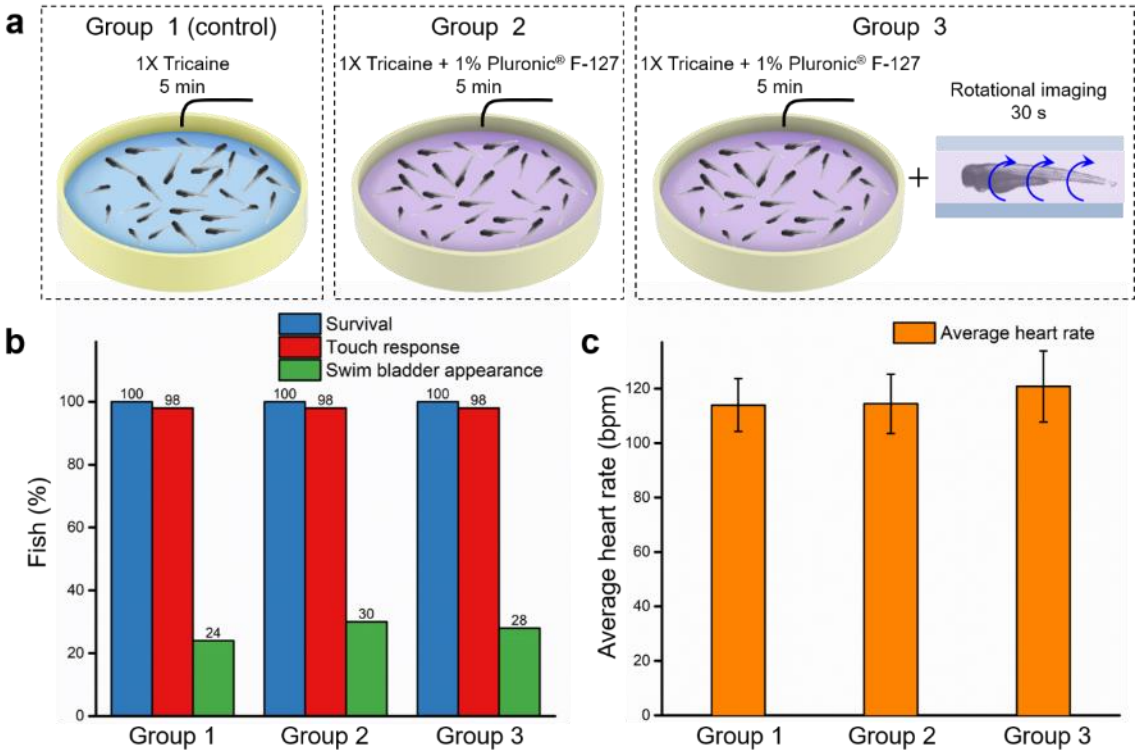

Figure 6.4: Assessment of zebrafish health. a, Schematics showing the test conditions of the three groups of 50 2CLIP zebrafish larvae studied in the health assessment. b, The rate of survival, touch response, and swim bladder appearance at 4 dpf of each group (n=50 for each rate). c, Average heart rate of each group of 50 fish. n=50 for each group. Data are graphed as the mean ± SD.

6.3 Phenotype ethanol-induced morphological abnormalities in larval body

In this sub-section, we applied the ART system to study the morphological abnormalities in the body of the zebrafish larvae resulting from EtOH exposure. The zebrafish larvae in the experimental group were exposed to 1.5% EtOH for 24 hours at

their 4-dpf and processed using the ART system at their 5-dpf (Figure 6.5). A control group was raised without EtOH for comparison. Details about zebrafish sample preparation are stated in Section 6.2.2.

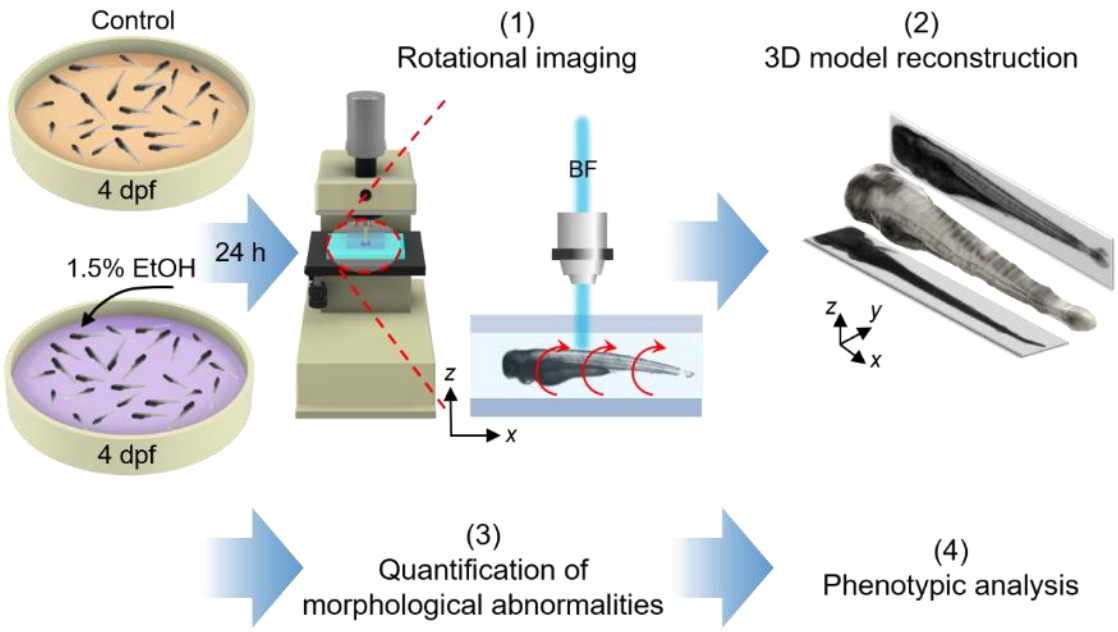

Figure 6.5: Procedure of using the ART system to phenotype ethanol-induced morphological abnormalities in zebrafish larval body. The entire procedure contains four steps as follow: (1) rotational imaging in the bright light field, (2) 3D model reconstruction of zebrafish body, (3) quantification of the morphological abnormalities in zebrafish body, and (4) phenotypic analysis based on the quantitative evaluation of the morphological abnormalities.

6.3.1 3D models

Using the ART system, each zebrafish sample were processed following four steps: (1) rotational imaging in the bright light field, (2) 3D model reconstruction of zebrafish body, (3) quantification of the morphological abnormalities in zebrafish body, and (4) phenotypic analysis based on the quantitative evaluation of the morphological

abnormalities. Based on the multi-view images, we reconstructed 3D model of the body of the zebrafish in control group and the experimental group. The morphological abnormalities resulting from the acute EtOH exposure can be qualified and quantified based on the 3D models.

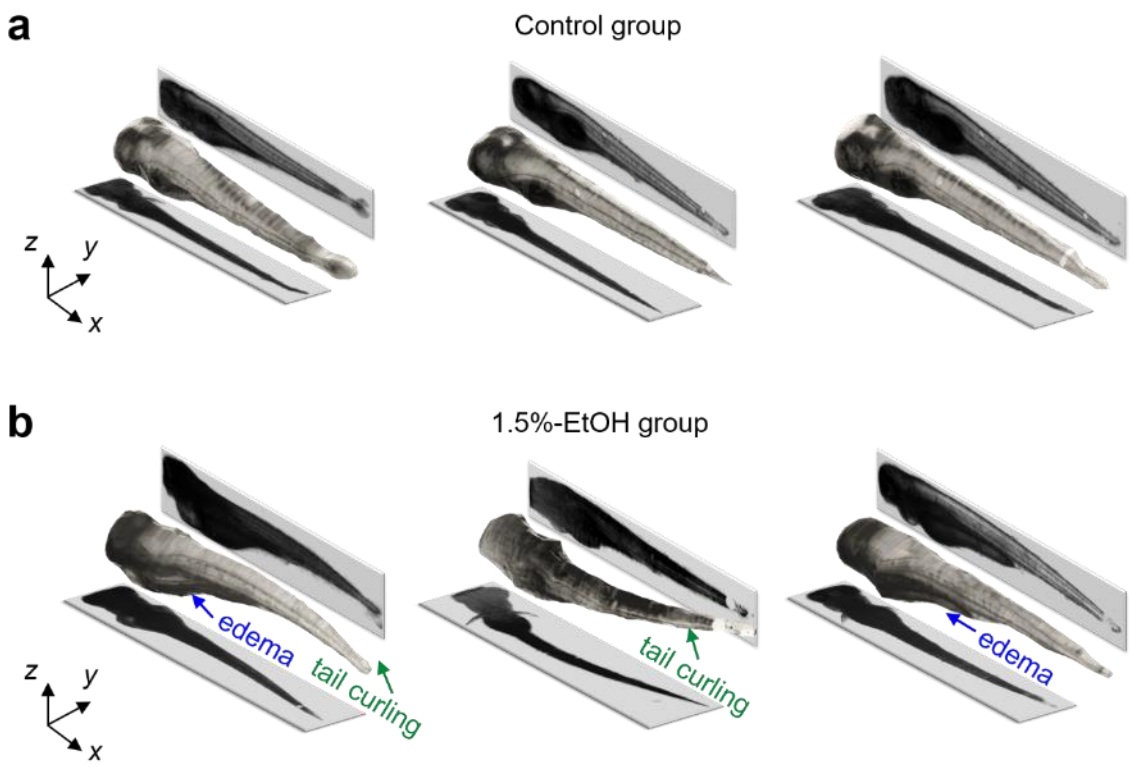

Figure 6.6: 3D reconstructed models of zebrafish larvae. a, 3D models of three zebrafish larvae from the control group. b, 3D models of three zebrafish larvae from the 1.5%-EtOH group, in which the abnormalities of tail curling and edema were observed.

Figure 6.6a and b show three representative 3D reconstructed models of zebrafish larvae from the control group and 1.5%-EtOH group, respectively. Base on the observation of the 3D models, the zebrafish larvae in the control group show consistent body sizes and straight configuration in tails. In comparison, the representative 3D

models in the 1.5%-EtOH group show commonly observed morphological abnormalities, which includes tail curling and edema. This implies that the acute EtOH exposure can induce edema and tail curling in the zebrafish body.

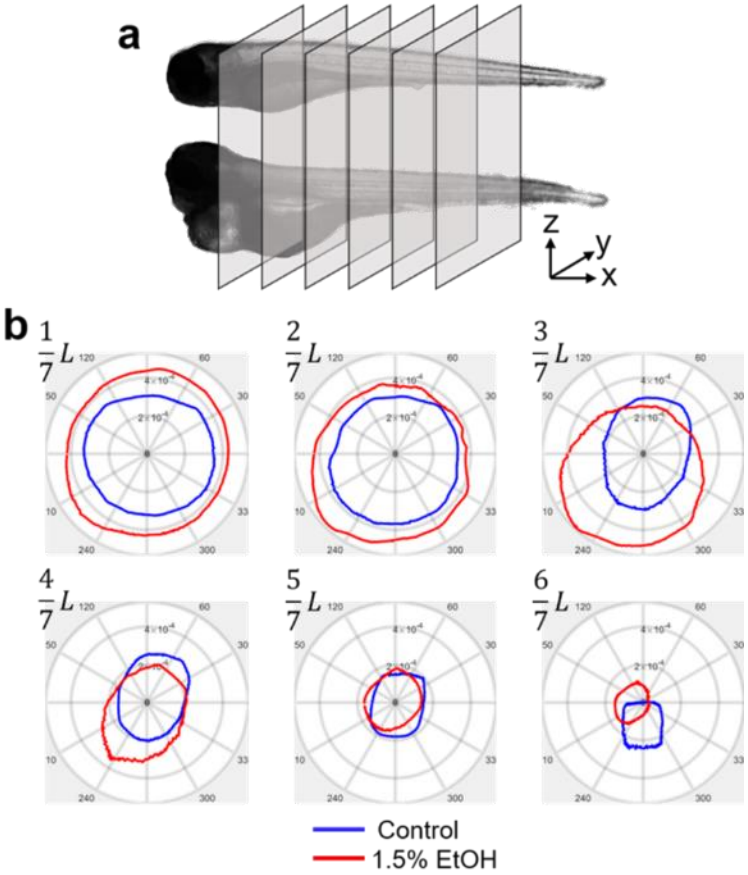

Figure 6.7: An outline analysis in the transverse (y-z) plane for size differences along x-axis. a, Illustrative images comparing the zebrafish larva without (top) and with (bottom) EtOH treatment. b, Comparisons of zebrafish outlines in the transverse plane showing the morphology difference along the zebrafish larva body. L represents the length of the larval body.

The rotational imaging allows to capture morphological characteristics from the 2D images in the lateral views. Benefiting from the digital examination of the resulting 3D model, the morphological information in the transverse plane (y-z plane), which cannot

be obtained from rotational imaging, can also be detected. Figure 6.7a shows a fish treated without EtOH (top) and a fish treated with EtOH (bottom). Based on their 3D models, their outlines on multiple transverse planes can be captured. Figure 6.7b shows comparison of the outlines of the two zebrafish sample. In the first 3/7 of the zebrafish body, the contour of the EtOH-treated larva is larger than those of the untreated larva. This indicates the edema induced by acute EtOH exposure. Comparing the outlines on the transvers plane at the 6/7 of the zebrafish body, the position offset of the contour of the EtOH-treated zebrafish larva indicates the abnormality in the tail curvature.

6.3.2 Quantification of morphological abnormalities based on 3D models

With the 3D models, visual observation of the 3D shapes and the outlines on the transverse planes can offer some insights of morphological information. Moreover, 3D models can offer quantitative metrics and provide consistent criteria for objective statistical analysis. With the quantitative data, the phenotyping results can be more objective and reliable.

The edema and tail curling are inherently reflected on the shape of the zebrafish. Here, we developed an analytical method to provide a quantitative parameter which quantifies morphological properties of the reconstructed 3D models. Taking this parameter as a criterion, the degree of the morphological defects in zebrafish can be quantified. The 3D geometric characteristics of the larval body can be quantitatively illustrated by the distribution of the normal vectors on the surface of reconstructed 3D

models. Thus, the morphological properties can be quantified by a parameter reflecting the distribution of the normal vectors. To obtain this parameter, we first calculated the normal vectors on the surface of zebrafish larvae based on the 3D model (Figure 6.8). Then, we calculated the angle (θ) between the x-axis and each normal vector. Last, we plotted histograms of the distribution of angles (θ) with Gaussian fits. In this way, the geometric characteristics of the larval body can be embodied by the Gaussian fitting curve and quantitatively reflected on the value of the variance of the Gaussian fitting curve (σ^2).

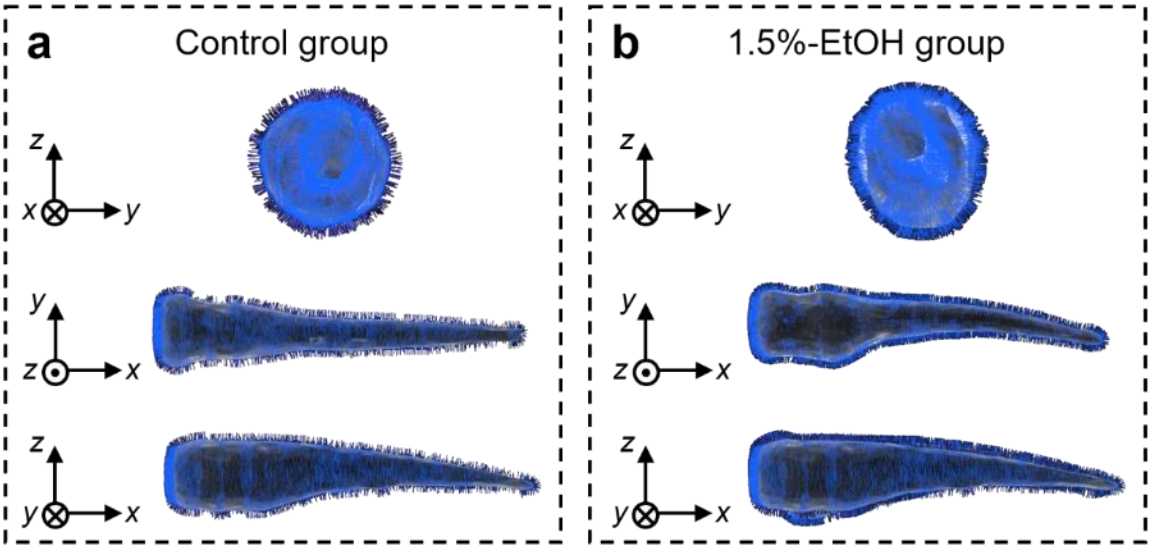

Figure 6.8: Distribution of normal vectors on the surface of reconstructed 3D models of a zebrafish larva. a, A 3D model of a zebrafish larva from the control group. b, A 3D model of a zebrafish larva from the 1.5%-EtOH group.

To better illustrate how the variance (σ^2) of the angle (θ) distribution Gaussian fitting curve quantitatively embodies the geometric characteristics of the larval body, we compared the variance of the angle distribution (σ^2) of four zebrafish larvae: a larva in control group, an unaffected larva in the experimental group, a larva in the experimental

group with edema, and a larva in the experimental group with tail curling. As shown in Figure 6.9a, we evenly divided the larval body into nice sections along the x-axis. The normal vector angles in each section characterize the geometry in the corresponding section. Then, for each larva, we plotted the histograms of the distribution of angles (θ) for the normal vectors in each section (Figure 6.9b). The curves in Figure 6.9c show the variance of the angle distribution (σ^2) along the body of the four larvae. The unaffected larva shows the similar distribution of the σ^2 along the body to the control group. This indicates that the unaffected larva possesses similar geometry to the fish in the control group. On the contrary, the σ^2 distribution of the fish with edema and tail curling displays large difference with the that of the control group. Specifically, the edema is shown to mainly contribute to larger variances in the first two thirds of the body, and tail curling is mainly located in the last one third of the body. Since the edema abnormality appears in almost all EtOH-treated zebrafish, the variance also shows slightly larger variance in the first two thirds of zebrafish for the zebrafish model with tail curling.

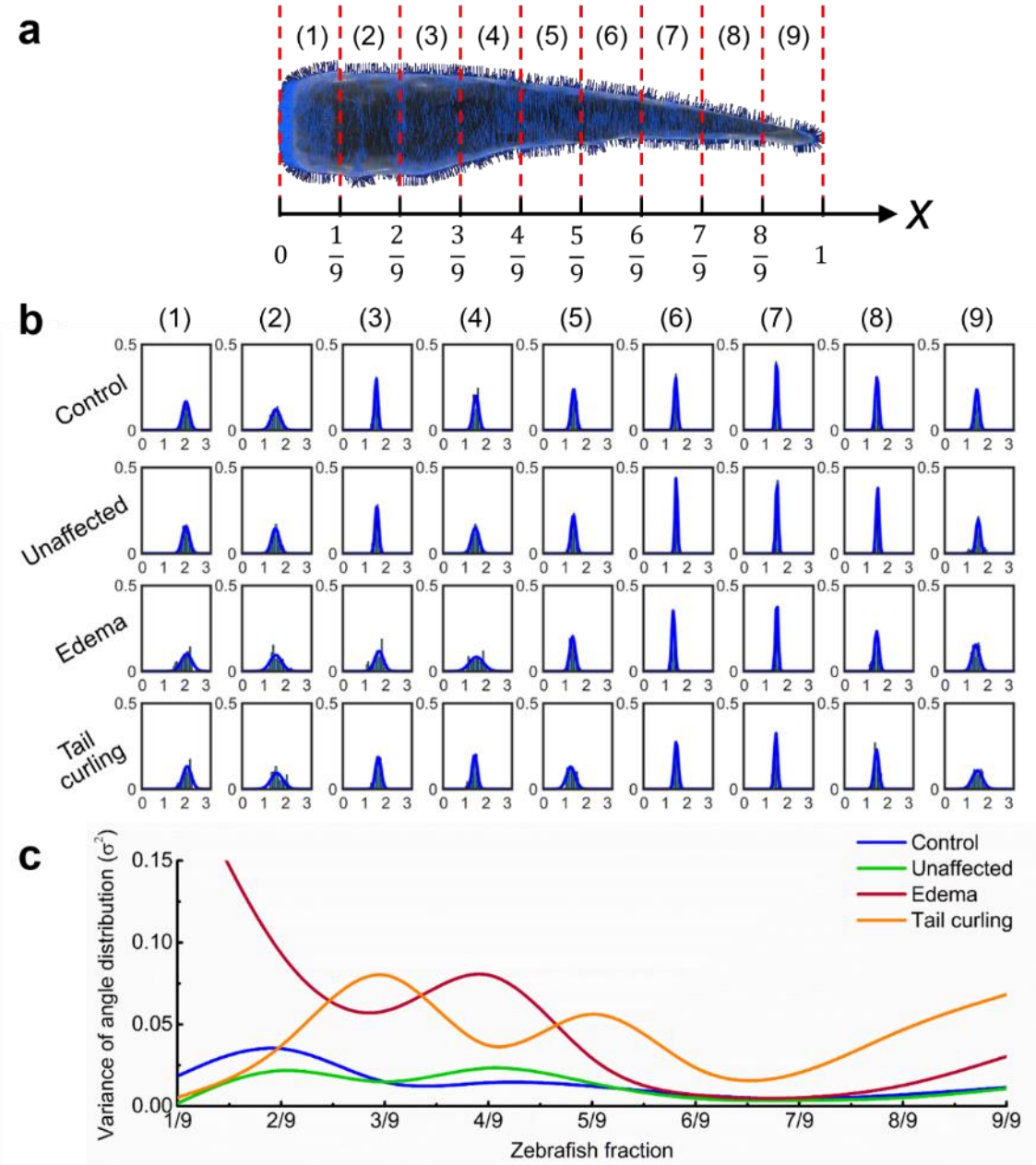

Figure 6.9: The angle distribution and variance of normal vectors relative to the x-axis along the zebrafish body. a, The nine even-divided sections of the larval body. b, The angle distribution for four zebrafish larvae: control, unaffected, edema, and tail curling. c, The variance of the angle distribution along the body.

As the edema and the tail curling mainly located in the first two thirds and the last one third of the larval body, respectively, the angle distribution (σ^2) of the anterior two thirds and posterior one third of the larval body were calculated to quantify the level of edema and tail curling, respectively. As such, we plotted the angle distribution (histogram and Gaussian fitting curve) of these two sections to quantify the level of edema (Figure 6.10a-d) and tail curling (Figure 6.10e-h). As shown in Figure 6.10, with larger deformations, the angles have a wider distribution based on the histogram and Gaussian fitting curve, as reflected on the value of the variance (σ^2). Thus, this analytical method based on the reconstructed 3D models can be used as a baseline standard to quantify the degree of abnormalities.

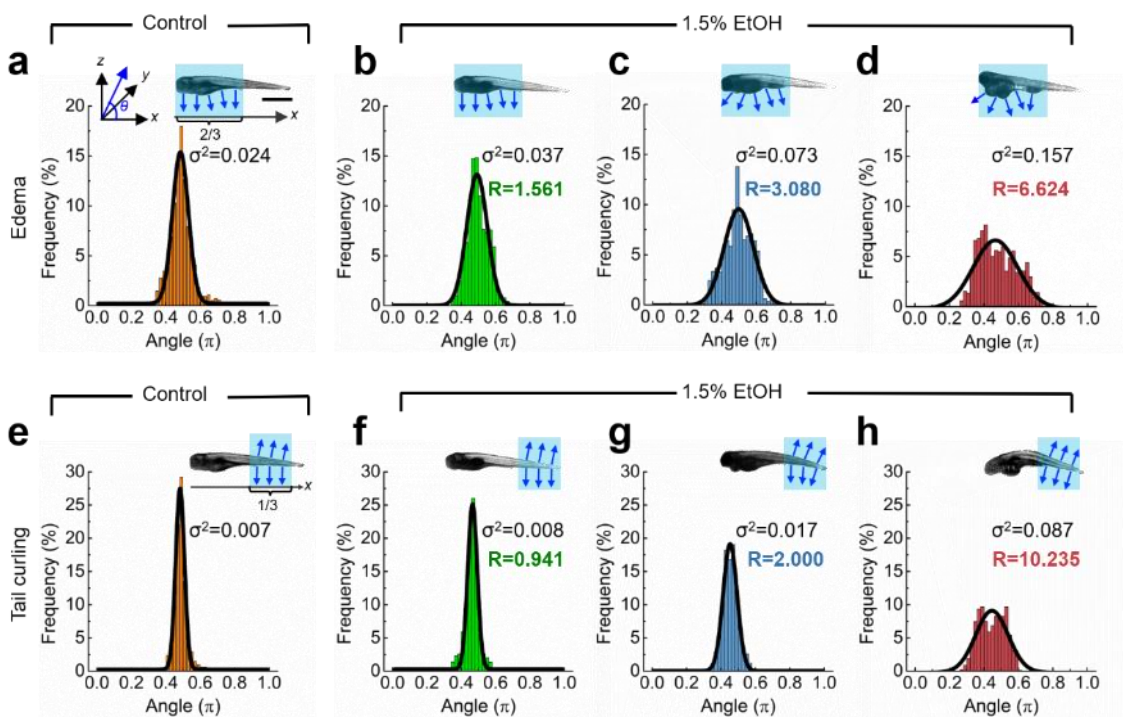

Figure 6.10: Distributions of the angle (θ) between normal vectors and the x-axis for zebrafish 3D models. a-d, Angle distribution ($\boldsymbol{\sigma^2}$) of the anterior two thirds of the larval body were calculated to quantify the level of edema. e-h, Angle distribution ($\boldsymbol{\sigma^2}$) of the posterior one third of the larval body were calculated to quantify the level of tail curling. a, A larva without abnormality of edema. b-d, Larvae with increasing degrees of edema. e, A larva without abnormality of tail curling. f-h, Larvae with increasing degrees of tail curling.

To further compare the abnormalities in the experimental group with that of the control group, we defined a factor called the "abnormality factor". The "abnormality factor" was defined as $\mathbf{R} = \boldsymbol{\sigma^2}/\boldsymbol{\sigma_0^2}$, where $\boldsymbol{\sigma^2}$ and $\boldsymbol{\sigma_0^2}$ are the variance in the angle distribution of the target zebrafish in the experimental group over the averaged variance of zebrafish of the control group. The value of the abnormality factor (**R**) quantifies the degree of the abnormalities and the morphological impact of EtOH exposure.

To obtain the averaged variance of zebrafish of the control group, we calculated the Gaussian fitting curves of the angle distribution of 15 larvae in the control group. As shown in Figure 6.11, the averaged variances of the angle distribution for edema and tail evaluation are $\sigma_{0\mathrm{E}}^2 = 0.0237 \pm 0.0091$ and $\sigma_{0\mathrm{T}}^2 = 0.0085 \pm 0.0032$, respectively. Based on this, the abnormality factors for edema of the zebrafish larvae shown in Figure 6.10b-d were calculated to be $R_E = 1.561$, $R_E = 3.080$, and $R_E = 6.624$, respectively. And the abnormality factors for tail curling of the zebrafish larvae shown in Figure 6.10f-h were calculated to be $R_T = 0.941$, $R_T = 2.000$, and $R_T = 10.235$, respectively. The larger value

of the R_E indicates a more sever degree of edema. The larger value of the abnormality factor (R) indicates a more sever degree of morphological abnormalities.

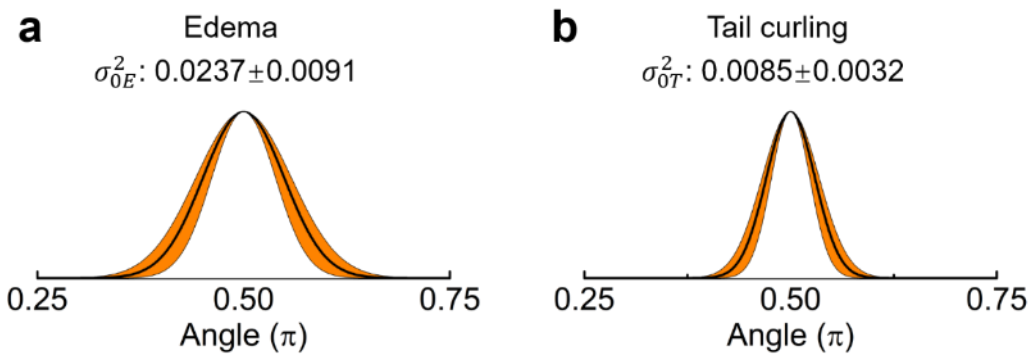

Figure 6.11: Gaussian fitting curves of the angle distribution statistics of 15 larvae in the control group.

6.3.3 Zebrafish phenotyping based on the abnormality factor

Based on the value of the abnormality factor, we categorized the EtOH-induced morphological abnormalities into six groups corresponding to the morphological traits (i.e., edema and tail curling) and levels of abnormalities (i.e., unaffected, moderate, and severe) measured in the imaged fish. Figure 6.12a shows the statistical distribution of the "abnormality factors" for edema and tail curling of the control group (n=15) and the 1.5%-EtOH group (n=35). Taking the value of R as a quantitative reference standard, we can classify the degree of edema and tail curling to three levels, i.e., unaffected (R≤1.5), moderate (1.5<R≤4), or severe (R>4). Using these levels, we calculated the phenotype percentage with these morphological abnormalities after the 1.5% EtOH exposure (Figure 6.12b). This quantitative evaluation of morphological abnormality provides a reference and quantification standard that is connected to traditional empirical criteria. While

edema or tail curling may be induced by different mechanism (e.g., body curling may be induced by shrinkage on one side or expansion on the other or by over or undergrowth of tissue), the statistical study of these abnormalities will aid in the identification of the single or multiple experimental variables which can induce this effect. Furthermore, a retrospective analysis of the resulting 3D model database can quickly locate specific abnormal zebrafish to perform further detailed physiological measurements (e.g., higher resolution imaging on certain parts of the zebrafish).

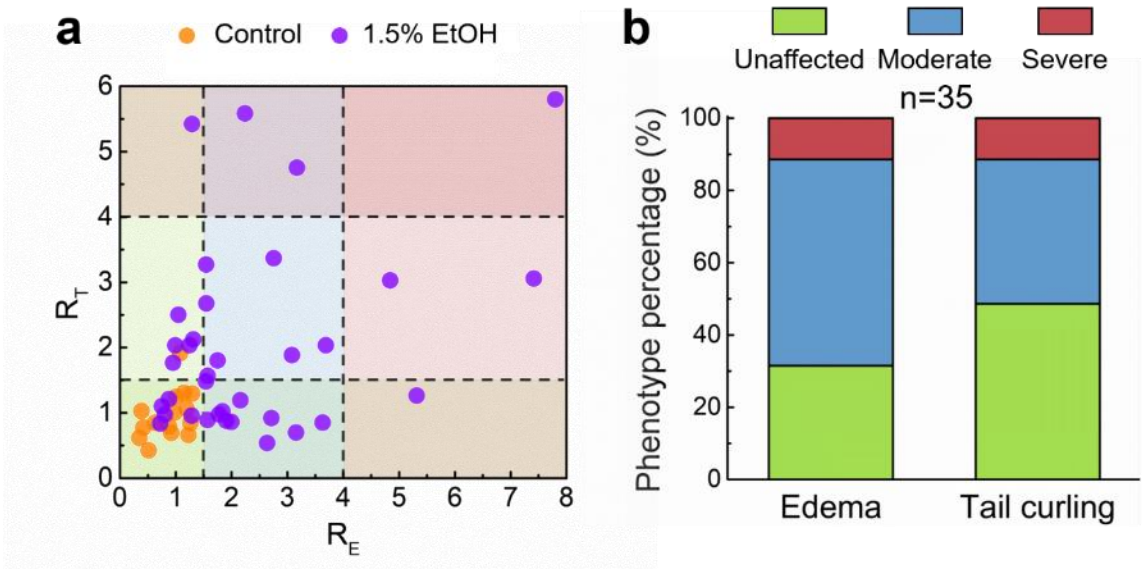

Figure 6.12: Morphological phenotyping based on automated quantitative measurements. a, Statistical distribution of the "abnormality factors" ($\mathbf{R} = \boldsymbol{\sigma}^2/\boldsymbol{\sigma}_0^2$) for edema and tail curling in the control group (n=15) and the 1.5%-EtOH group (n=35). Based on statistical analysis, the larvae within the range of R⩽1.5, 1.5<R⩽4, and R>4 are categorized as unaffected, moderate, and severe, respectively, for morphological abnormality level. b, The percentage of phenotype classification (as unaffected, moderate, or severe) of the morphological abnormalities after the 1.5% EtOH exposure.

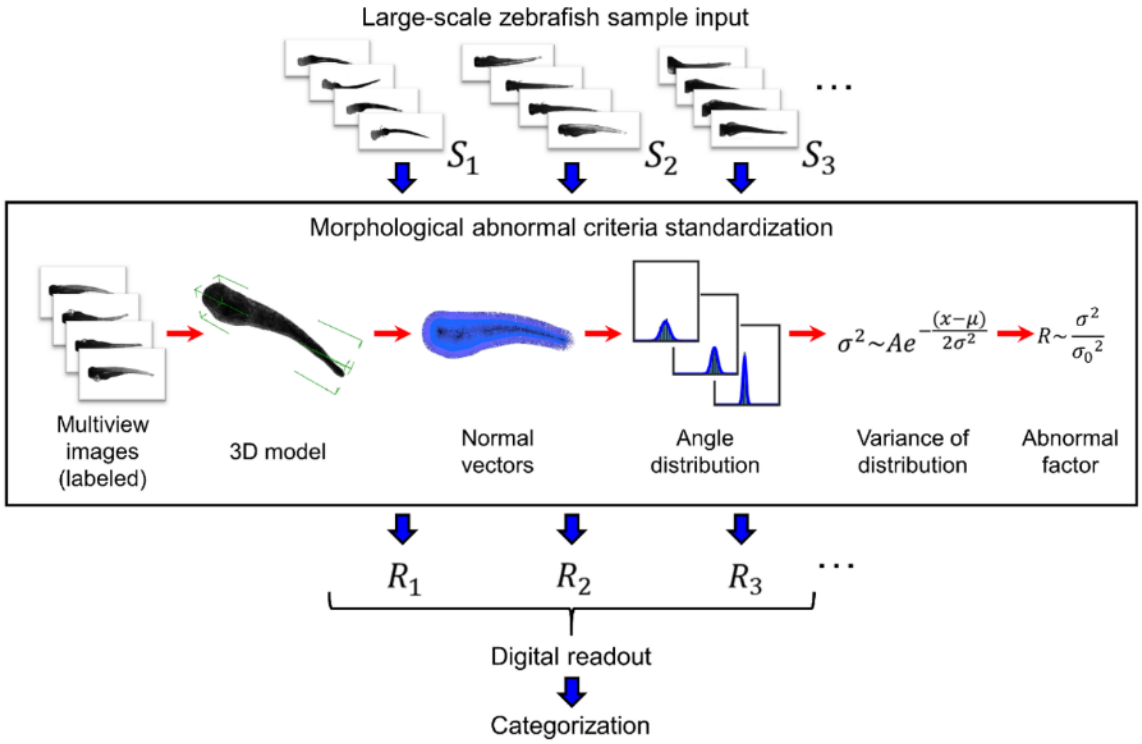

Figure 6.13: Flow chart of the abnormal level characterization and pipeline for morphological abnormal criteria standardization. The standardization process is indicated in the black frame that connects the empirical criteria with the numbers. As the process builds, large-scale zebrafish samples can be fed into the system to generate digitalized readouts for abnormal level quantification and used for categorization. The three categories for edema and tail curling are identified based on the statistical angle distribution for each category as: (1) Unaffected: $\boldsymbol{R \leq 1.5}$, (2) Moderate: $\boldsymbol{1.5 < R \leq 4}$, (3) Severe: $\boldsymbol{R > 4}$.

Using our ART platform, we can also determine the percentage of the phenotype's frequency via the aforementioned automated quantification process (see Figure 6.13 for the entire process flow). Our results showed that edema is a more common morphological abnormality, as induced by acute EtOH exposure, when compared to the frequency of tail curling, with ~70% of the larvae displaying edema at the belly after EtOH exposure, and ~10% being classified as a severe deformation. In comparison, ~50% of the EtOH-exposed

population displayed tail curling, of which roughly 10% were considered severe. These findings are consistent with recent published research which has shown a strong correlation between edema and EtOH exposure. This has drawn parallels to the impact on human infants suffering from fetal alcohol syndrome (X. Li et al., 2016; Passeri, Cinaroglu, Gao, & Sadler, 2009).

6.4 Phenotype ethanol-induced morphological abnormalities in larval liver

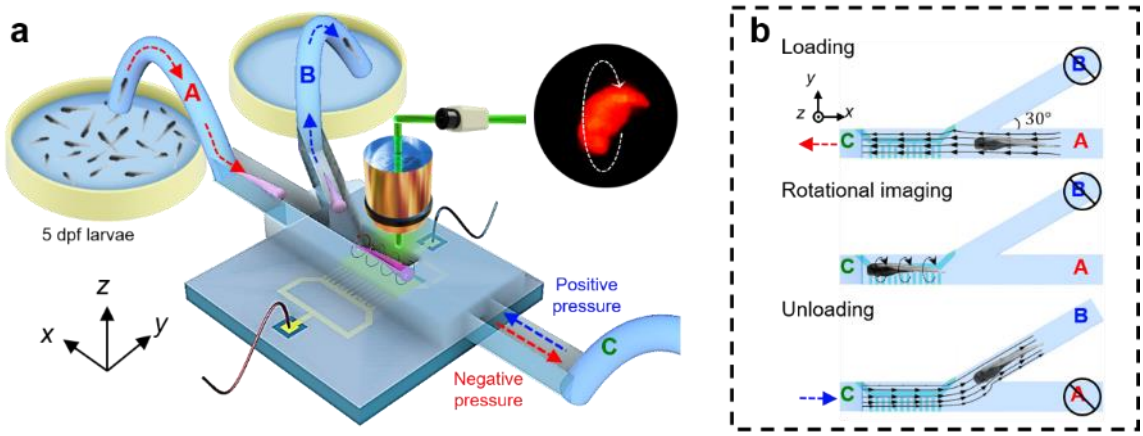

Figure 6.14: Schematic illustration shows the setup for imaging zebrafish samples. a, The setup of the semi-automated flow control system of the ART platform. b, The flow settings for sample loading, rotational imaging, and the unloading processes.

In addition to the morphological abnormalities in the larval body, acute EtOH exposure has also been reported to induce abnormalities in the zebrafish liver. This is similar to the negative impact that alcohol abuse can have on liver function in humans, presenting itself as steatosis, or "alcoholic fatty liver disease" (Goessling, North, & Zon, 2007; Howarth, Passeri, & Sadler, 2011; Zang, Maddison, & Chen, 2018). Here, we

demonstrate a step towards automated 3D reconstruction of zebrafish larvae using the ART system.

As shown in Figure 6.14, a Y-shaped channel with 3 branches enables the successive process of high-throughput sample loading, rotational imaging, and sample unloading. Briefly, branch "C" was connected to a syringe pump for controlling the flow direction to load the sample from inlet "A" or unload the sample from outlet "B". The branches "A" and "B" were mounted to a three-way pinch valve, in which one channel is normally open while another one is normally closed. Using this valve, the flow in one branch of either "A" and "B" was blocked when the sample passed through the other branch. Fig. Figure 6.14b shows the status of the syringe pump and the pinch valve in the three pre-programmed modes of sample loading, imaging, and unloading. Using this semi-automated ART system, we rotationally imaged the zebrafish samples under DsRed fluorescent illumination and reconstructed the 3D models of the livers. We successively performed this imaging and 3D reconstruction process on a group of 1.5%-EtOH-treated zebrafish sample and a group of control samples to investigate the effect of EtOH on the liver size within the developing larva.

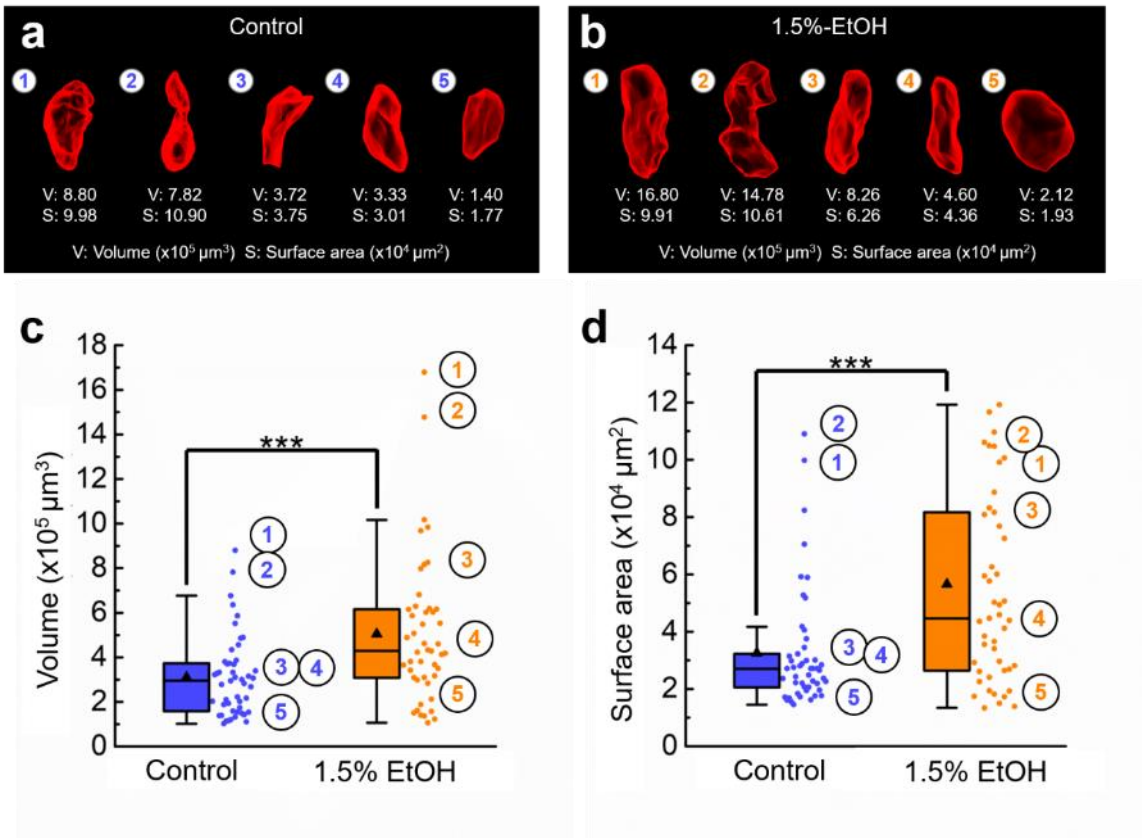

Figure 6.15: 3D models and quantification of zebrafish liver. a, Typical reconstructed 3D models and quantification of zebrafish livers from the control group. b, Typical reconstructed 3D models and quantification of zebrafish livers from the 1.5%-EtOH group. c, d, Statistics of the liver volume distribution and the surface area distribution of the control group and 1.5%-EtOH group, respectively. (One-way ANOVA, ***:P<0.0005, P=0.000461 for volume and P=0.000316 for surface area). All boxplots indicate median (center line), mean (triangle), 25th and 75th percentiles (bounds of box), and ±1.5 × IQR (interquartile range) (whiskers).

Figure 6.15a and Figure 6.15b show five typical 3D reconstructed models of zebrafish livers and quantification of the liver size from the control group and 1.5%-EtOH group, respectively. Liver size quantification via volume and surface area measurements were gathered from 49 samples in the control group and 47 samples in the 1.5%-EtOH.

The size of the livers from the two groups were compared by statistical analysis (One-way ANOVA). From the 3D reconstruction, we found that the livers of the 1.5%-EtOH group typically had larger average sizes and less regular shapes than those of the control group. The liver volume distribution (Figure 6.15c) and liver surface area distribution (Figure 6.15d) show that, on average, EtOH exposure caused liver sizes to enlarge 73.7% by surface area (3.26x105 μm^3 for the control group vs. 5.66x105 μm^3 for the EtOH group) and increased 62.7% by volume (3.10×104 μm^2 for the control group vs. 5.07x104 μm^2 for the EtOH group). The increase in the liver surface area of the EtOH-exposed group is most likely attributed to an increase in surface roughness and liver shape variance, which increased the surface area faster than the liver volume. By analyzing the 3D model generated using the ART system, we extracted the outline features from three standard planes (i.e., sagittal plane (x-z), coronal plane (x-y), and transverse plane (y-z), as shown in Figure 6.16. The comparison of the outline features shows that while the overall liver volume will increase after EtOH exposure, the liver shape has also been changed from a "V" like shape to a rounder shape. This is most possibly due to the increase in cell volume and compression against adjacent tissues (e.g., edema effect in zebrafish belly). Our ART system was thus used to demonstrate that EtOH exposure can induce morphological changes in the liver, such as enlarged size and surface roughness, and this can be measured in a semi-automated manner. Altogether, these results demonstrate the

capabilities of ART for conducting high-throughput morphological phenotyping of live vertebrates.

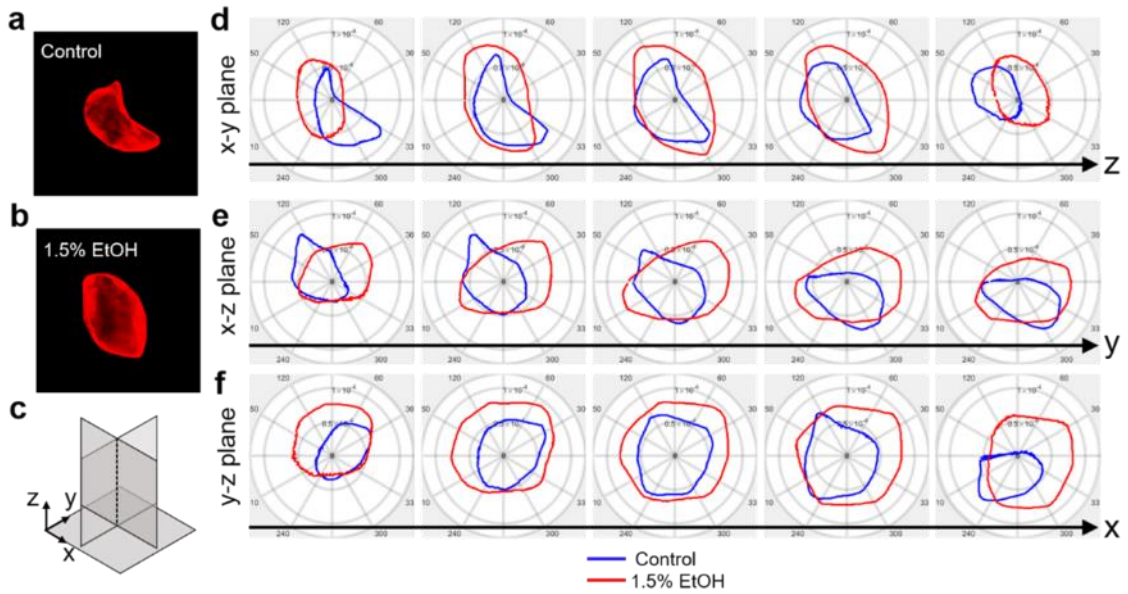

Figure 6.16: Outline contours from the projection of the typical reconstructed 3D model of a zebrafish liver in the (a) control and (b)1.5%-EtOH groups. a, 3D model of a liver in the control group. b, 3D model of a liver in the 1.5%-EtOH group. c, Schematic shows the coordinate axis and the x-y, x-z, and y-z projection planes. d-f, Contours of the projection of the 3D model of the liver in (a) and (b).

6.5 Discussion and conclusion

In Chapter 4, Chapter 5, and Chapter 6, we have demonstrated an acoustofluidic rotational tweezing (ART) platform that integrates the functions of (1) acoustic-based contactless rotational manipulation, (2) multi-view multispectral imaging, (3) 3D model reconstruction and quantitative evaluation of morphological abnormalities, and (4) phenotypic analysis based on quantitative reference standard for batches of zebrafish larvae.

Our acoustofluidic technology was successfully demonstrated to stably and rapidly rotate model organisms with different sizes and shapes in a contactless manner. This could potentially benefit not only large-scale morphological evaluations but also enable the long-term, periodic phenotype quantification of model organisms at different stages of development. Although not originally targeting for use with advanced imaging systems, our ART system does contain specific features comparable to the state-of-art 3D phenotyping techniques. For example, optical projection tomography, as one of the most powerful imaging methods for live rodents, can provide label-free structural images for morphometrics in developmental biology. 3D morphology information can be generated in a single imaging session (Hallgrimsson et al., 2015; Singh et al., 2016). Also, Micro-CT, a commonly used technique for visualization of skeletal tissue or embryonic soft tissues, can provide images with high spatial resolution (Hallgrimsson et al., 2015; Singh et al., 2016). Each method has advantages and limitations. For example, optical projection tomography will need fixation of the sample during imaging which may potentially make it difficult to preserve certain morphology information (Singh et al., 2016). Meanwhile, due to the imaging mechanism, real-time viewing will be difficult to obtain(Singh et al., 2016; Vinegoni et al., 2009). Micro-CT, on the other hand, has a similar potential issue with morphology distortion due to fixation or desiccation as scanning in a liquid medium would be problematic due to the low contrast between tissue and water (Schmidt et al., 2010). Compared to these methods, the advantages of our ART system are the non-contact

feature and phenotyping in a near-continuous flow mode that can efficiently image and digitize a large number of specimens. Meanwhile, the overall system is more compact and flexible as different imaging or analysis tool can be integrated. It would also be worth noting that just like optical projection tomography, the imaging quality of our system would depend on the optical imaging lens. Different lenses would be needed to achieve various depth of focus and resolutions. Furthermore, the system could be further developed to enable fully automated processing which serves as a target for our next stage of research.

We performed a proof-of-concept demonstration by phenotyping a large population of 5 dpf zebrafish larvae with respect to changes to body morphology and liver size due to EtOH exposure. Leveraging our acoustofluidic rotational imaging mechanism and recent advances in computer vision techniques, we can reconstruct a 3D model with a composite of bright-field and fluorescent images of the zebrafish and highlighted portions in a rapid and efficient manner. Any uneven rotation angle between each video frame would affect the resulting 3D reconstruction. As the corresponding angles are related to the camera matrix (rotation matrix) that was used to determine the isosurface of the 3D model, any rotational non-uniformity corresponding to an incorrect estimate for the image angle will cause distortions in the 3D model. In order to have a consistent rotation angle in our experiment, the optimal acoustic voltage was used to generate a strong acoustic streaming and drag force. Thus, in this stable rotation mode,

the force torque would be zero and since angular momentum is conserved, this effectively results in uniform rotation (Figure 5.11). This 3D reconstruction produced a high-resolution model for the detailed analysis of phenotypic data. While classic 3D scanning and reconstruction techniques (e.g., confocal laser scanning microscopy) suffer from discretization artifacts, our acoustofluidic method takes images from multiple angles and combines the images via 3D reconstruction, hence minimizing optical interference effects resulting from various depth. A complete cycle of loading, rotational imaging under three different light fields, 3D reconstruction of the body and organs, and unloading a zebrafish usually took less than 59.1 seconds using the ART with 3D multispectral imaging (Table 6.2). During the entire process, each cycle of rotation required ~1 second. Combined with the loading and unloading time, the complete rotational imaging of one specimen required less than 11.2 seconds for imaging under a single light field and less than 14.4 seconds for imaging under three different light fields. This rotational imaging speed of the ART platform is comparable to that of the VAST system(Pardo-Martin et al., 2010), whereas the sample loading efficiency is slightly lower. This process could be improved by integrating a robotic arm that draws zebrafish samples from a 96-well plate or adding a propeller inside the reservoir. Combining all the features of our ART system, we are able to quickly examine a large population of specimens and produce digital 3D multispectral models of each specimen for subsequent detailed analysis. Considering the zebrafish larvae or the structures of interest as “large particles”, the workflow of the ART system is

similar to that the flow cytometry systems process with cell samples. As shown in Figure 5.2, this workflow dramatically reduces the time required for tasks involving microscope-based multispectral examination of small animal models. Moreover, the statistical data is drawn from quantified consistent criteria for phenotyping studies. This can accelerate drug discovery as well as minimize the number of personnel hours required and subjective interference compared to previous manual specimen loading and observation methods.

Previous studies looking into morphological abnormalities in zebrafish have relied on the subjective evaluation of the abnormality level. With our platform, we can rotate and image the fish from different viewing angles for enhanced observation, and we can directly transfer the complete, multispectral, digital zebrafish model into an automated machine-vision-based analysis program. This technique is performed using only a conventional optical microscope and could potentially standardize the process of morphological phenotyping. Altogether, we believe our ART platform shows great potential as the basis for non-contact live vertebrate manipulation and transport with culturing, 3D imaging, and semi-automated analysis capabilities for applications such as drug discovery, personalized cancer therapy testing, and the evaluation of environmental toxicity effects.

7. Conclusion and Prospects

In this chapter, we first summarized the achievement in Section 7.1. Then in Section 7.2 the prospects of developing systems to utilize the acoustics-induced fluid motion for more versatile biotechnological applications is discussed.

7.1 Achievements

In this dissertation, we have firstly introduced the underlying mechanism and theory of acoustic induced fluid motion, mainly including the acoustic streaming and interface deformation. Then we have presented that the vortex streaming can be initiated by acoustic waves and utilized for the manipulation of object with the size from centimeter range to nanometer range. Based on this principle, we have been exploring more advanced and innovative acoustofluidic techniques which perform versatile and accurate manipulation of various biological objects (e.g., exosomes, cells, C. elegans, and zebrafish larvae). My dissertation work has centered around exploring the acoustic streaming effect in various microfluidic devices and developing the acoustic rotational tweezing (ART) platform for zebrafish larvae phenotyping. Specifically, we have designed an acoustofluidic device with an innovative working mechanism that can generate an acoustic streaming vortex to rotate zebrafish larvae for multi-view imaging. While it is difficult for common acoustic methods to generate large vortex streaming with high intensity, our design is harnesses by the imbalanced body force generated by surface acoustic wave and fluid channel confinement. Thus, a “polarized” acoustic streaming can

be formed perpendicular to the plane where surface acoustic wave propagates. By designing a Y-shape channel fitted with programmable pinch valves for sample loading/unloading, the device achieves high-throughput imaging of batches of zebrafish larvae at a speed of ~1 rotation/second. Meanwhile, a computer-vision-based algorithm is developed in order to generate 3D reconstruction models of the larvae using the multi-view images; this algorithm enables quantitative evaluation of the morphological abnormalities of each sample. This is the first acoustofluidic platform that achieves contactless manipulation of zebrafish larvae, and it is the first platform with a cytometry-like workflow designed specifically for handling zebrafish larvae. With integrated functions including sample loading/unloading, acoustic-enabled contactless rotation and multi-view imaging, 3D model reconstruction, and quantitative phenotypic analysis, the platform can efficiently provide quantitative digital readouts for zebrafish phenotyping; this technology is beneficial for various biomedical and biotechnological applications, including drug discovery acceleration and personalized medicine based on animal models. Compared to existing zebrafish handling platforms, our ART technique is contactless, inexpensive, easy to use, and most importantly, provides quantitative evaluation of abnormalities for a large volume of samples in an efficient manner. We believe our platform moves one step forward for applying acoustofluidic technique to practical statistical phenotyping studies.

Furthermore, during the development of various acoustofluidic platforms, we have developed multiple theoretical models that can be utilized for analyzing the acoustic generated fluid motion in the domain with different scales. For example, the boundary driven streaming significantly simplified the numerical model by dividing the classic perturbation theory into inner and outer boundary layer streaming calculation. This two-step numerical simulation method substantially reduced the calculation amount and fits well with the experimental streamline. On the other hand, the Reynold stress-based streaming can be applied to different acoustofluidic models with a strong capability to predict the streaming pattern in different fluid system and provide guidance to different acoustofluidic device designs.

7.2 Prospects

Despite the substantial success in the development of both the theoretical analysis and applications using acoustofluidic technique, great lengths are required in order to generate real impact for practical usage. Meanwhile, as a multidisciplinary research field, the further combination between the acoustofluidic method and other research topics could be envisioned.

From the physics point of view, Navier-Stokes equation has been a difficult topic that appeals to the researchers in various fields. While acoustic waves propagation will inevitably bring the fluid motion effect, there have been numerous studies researching the minimization of the effect, especially for the purpose of manipulation. However, when

applied to objects that have the size outside of the wavelength range, the fluid motion could still be problematic. Thus, utilizing the fluid motion and making the fluid motion coordinate with acoustic waves would still possibly be an ideal way to handle the manipulation in different scenarios. For example, when in the need of precisely manipulating very small object (e.g., nanoparticles), the conflict between the required frequency and the large attenuation during the wave propagation makes the bottleneck of practical usage. On the other hand, when manipulating the object with relatively large size (e.g., cm scale) in the liquid, the lower frequency acoustic wave may not provide sufficient force and precision, while the higher frequency acoustic wave may directly propagate through the object without generating the force on the boundary between the object and surrounding fluid. Thus, deeper understanding and utilization of the fluid motion could benefit to the acoustofluidic manipulation in different ways. Furthermore, as in our study, while we could calculate the acoustic and streaming field for interface deformation or inner streaming, the 3D flow field calculation that can indicate both the deformation and streaming will be extreme difficult, especially when dealing with a large fluid domain. This potentially could be solved or simplified if other simulation methods are introduced. One potential solution is utilizing the Smoothed-particle hydrodynamics method, which is a meshfree Lagrangian method and can be applied to more complex fluid motion in large domains(wikipedia, n.d.-b). This method could specifically benefit

to the acoustofluidic motion evaluation as the essence of the phenomenon is the fluid particle movement.

From the application aspect, the acoustic tweezers technique is currently under rapid development. Various demonstrations have indicated the great potential applying acoustic manipulation to different applications, e.g., in-vivo manipulation(Ghanem et al., 2020), volumetric display(Hirayama, Plasencia, Masuda, & Subramanian, 2019), and cell separation(Wu et al., 2017). In the airborne acoustic manipulation, while the influence usually is small, the fluid motion may still induce slight disturbance during the manipulation. For underwater manipulation, the microstreaming induced by acoustic wave or structure boundary conditions could potentially have larger influences for manipulation. Acoustofluidic methods also possess several unique features for life science studies, and will play a critical role for higher health monitoring is required. Future acoustofluidic techniques may also be combined with more research fields and be utilized for data generation instead of staying a purely functional workflow. Our acoustofluidic zebrafish phenotyping study is an example of the fusion of different techniques. With the development and collaboration of different research fields, the more integrated and comprehensive acoustofluidic platforms can be envisioned for various applications in the field of biomedical, materials science, chemistry etc.

References

Adamson, K. I., Sheridan, E., & Grierson, A. J. (2018). Use of zebrafish models to investigate rare human disease. *Journal of Medical Genetics*, *55*(10), 641–654. https://doi.org/10.1136/jmedgenet-2018-105358

Ahmed, D., Ozcelik, A., Bojanala, N., Nama, N., Upadhyay, A., Chen, Y., … Huang, T. J. (2016). Rotational manipulation of single cells and organisms using acoustic waves. *Nature Communications*, *7*, 11085.

Ahmed, D., Ozcelik, A., Bojanala, N., Nama, N., Upadhyay, A., Chen, Y., … Huang, T. J. (2016). Rotational manipulation of single cells and organisms using acoustic waves. *Nature Communications*, *6*, 1–11. https://doi.org/10.1038/ncomms11085

Alghane, M., Chen, B. X., Fu, Y. Q., Li, Y., Desmulliez, M. P. Y., Mohammed, M. I., & Walton, A. J. (2012). Nonlinear hydrodynamic effects induced by Rayleigh surface acoustic wave in sessile droplets. *Physical Review E - Statistical, Nonlinear, and Soft Matter Physics*, *86*(5), 2–7. https://doi.org/10.1103/PhysRevE.86.056304

Alghane, M., Chen, B. X., Fu, Y. Q., Li, Y., Luo, J. K., & Walton, A. J. (2011). Experimental and numerical investigation of acoustic streaming excited by using a surface acoustic wave device on a 128° YX-LiNbO3 substrate. *Journal of Micromechanics and Microengineering*, *21*(1). https://doi.org/10.1088/0960-1317/21/1/015005

Alghane, M., Fu, Y. Q., Chen, B. X., Li, Y., Desmulliez, M. P. Y., & Walton, A. J. (2012). Frequency effect on streaming phenomenon induced by Rayleigh surface acoustic wave in microdroplets. *Journal of Applied Physics*, *112*(8), 084902. https://doi.org/10.1063/1.4758282

Alghane, M. M. (2013). Surface acoustic wave streaming in a microfluidic system. Heriot-Watt University.

Arifin, W. N., & Zahiruddin, W. M. (2017). Sample size calculation in animal studies using resource equation approach. *Malaysian Journal of Medical Sciences*, *24*(5), 101–105. https://doi.org/10.21315/mjms2017.24.5.11

Atanasoff, J. V, & Hart, P. J. (1941). Dynamical determinitation of the elastic constants and their temperature coefficients for quartz. *Physical Review*, *59*(1), 85.

Baker, S., & Kanade, T. (2005). Shape-from-silhouette across time part i: Theory and algorithms. *International Journal of Computer Vision*, *62*(3), 221–247.

Barnkob, R., Augustsson, P., Laurell, T., & Bruus, H. (2012). Acoustic radiation-and streaming-induced microparticle velocities determined by microparticle image velocimetry in an ultrasound symmetry plane. *Physical Review E*, *86*(5), 56307.

Baumgart, B. G. (1974). *Geometric modeling for computer vision*. STANFORD UNIV CA DEPT OF COMPUTER SCIENCE.

Bertin, N., Chraïbi, H., Wunenburger, R., Delville, J. P., & Brasselet, E. (2012). Universal Morphologies of fluid interfaces deformed by the radiation pressure of acoustic or electromagnetic waves. *Physical Review Letters*, *109*(24), 1–5. https://doi.org/10.1103/PhysRevLett.109.244304

Brunet, P., Baudoin, M., Matar, O. B., & Zoueshtiagh, F. (2010). Droplet displacements and oscillations induced by ultrasonic surface acoustic waves: a quantitative study. *Physical Review E*, *81*(3), 36315.

Chen, C., Gu, Y., Philippe, J., Zhang, P., Bachman, H., Zhang, J., … Davis, E. E. (2021). Acoustofluidic rotational tweezing enables high-speed contactless morphological phenotyping of zebrafish larvae. *Nature Communications*, *12*(1), 1–13.

Chen, C., Zhang, S. P., Mao, Z., Nama, N., Gu, Y., Huang, P.-H., … Huang, T. J. (2018). Three-dimensional numerical simulation and experimental investigation of boundary-driven streaming in surface acoustic wave microfluidics. *Lab on a Chip*, *18*(23), 3645–3654.

Chen, K., Sui, C., Wu, Y., Ao, Z., Guo, S., & Guo, F. (2018). A digital acoustofluidic device for on-demand and oil-free droplet generation. *Nanotechnology*, *30*(8), 84001.

Chono, K., Shimizu, N., Matsui, Y., Kondoh, J., & Shiokawa, S. (2004). Development of novel atomization system based on SAW streaming. *Japanese Journal of Applied Physics*, *43*(5S), 2987.

Cignoni, P., Callieri, M., Corsini, M., Dellepiane, M., Ganovelli, F., & Ranzuglia, G. (2008). Meshlab: an open-source mesh processing tool. In *Eurographics Italian chapter conference* (Vol. 2008, pp. 129–136). Salerno.

Cinbis, C., Mansour, N. N., & Khuri-Yakoub, B. T. (1993). Effect of surface tension on the acoustic radiation pressure-induced motion of the water–air interface. *The Journal of the Acoustical Society of America*, *94*(4), 2365. https://doi.org/10.1121/1.407456

Collins, D. J., Khoo, B. L., Ma, Z., Winkler, A., Weser, R., Schmidt, H., … Ai, Y. (2017). Selective particle and cell capture in a continuous flow using micro-vortex acoustic

streaming. *Lab Chip*, *17*, 1769–1777. https://doi.org/10.1039/C7LC00215G

Collins, D. J., Ma, Z., Han, J., & Ai, Y. (2017). Continuous micro-vortex-based nanoparticle manipulation via focused surface acoustic waves. *Lab on a Chip*, *17*(1), 91–103. https://doi.org/10.1039/C6LC01142J

Datta, S. (1986). *Surface acoustic wave devices*. Prentice Hall.

Dentry, M. B., Yeo, L. Y., & Friend, J. R. (2014). Frequency effects on the scale and behavior of acoustic streaming. *Physical Review E - Statistical, Nonlinear, and Soft Matter Physics*, *89*(1), 1–11. https://doi.org/10.1103/PhysRevE.89.013203

Devendran, C., Collins, D. J., Ai, Y., & Neild, A. (2017). Huygens-Fresnel Acoustic Interference and the Development of Robust Time-Averaged Patterns from Traveling Surface Acoustic Waves. *Physical Review Letters*, *118*(15), 1–6. https://doi.org/10.1103/PhysRevLett.118.154501

Ding, X., Lin, S.-C. S., Kiraly, B., Yue, H., Li, S., Chiang, I.-K., … Huang, T. J. (2012). On-chip manipulation of single microparticles, cells, and organisms using surface acoustic waves. *Proceedings of the National Academy of Sciences*, *109*(28), 11105–11109.

Du, X. Y., Swanwick, M. E., Fu, Y. Q., Luo, J. K., Flewitt, A. J., Lee, D. S., … Milne, W. I. (2009). Surface acoustic wave induced streaming and pumping in 128° Y-cut LiNbO 3 for microfluidic applications. *Journal of Micromechanics and Microengineering*, *19*(3), 035016. https://doi.org/10.1088/0960-1317/19/3/035016

Elrod, S. A., Hadimioglu, B., Khuri-Yakub, B. T., Rawson, E. G., Richley, E., Quate, C. F., … Lundgren, T. S. (1989). Nozzleless droplet formation with focused acoustic beams. *Journal of Applied Physics*, *65*(9), 3441–3447.

Farooq, M., Sulochana, K. N., Pan, X., To, J., Sheng, D., Gong, Z., & Ge, R. (2008). Histone deacetylase 3 (hdac3) is specifically required for liver development in zebrafish. *Developmental Biology*, *317*(1), 336–353. https://doi.org/10.1016/j.ydbio.2008.02.034

Feenstra, P. J. (1978). *Modeling and control of surface acoustic wave motors* (Vol. 30).

Foresti, D., & Poulikakos, D. (2014). Acoustophoretic contactless elevation, orbital transport and spinning of matter in air. *Physical Review Letters*, *112*(2), 24301.

Friend, J., & Yeo, L. Y. (2011). Microscale acoustofluidics: Microfluidics driven via acoustics and ultrasonics. *Reviews of Modern Physics*, *83*(2), 647.

Frommelt, T., Gogel, D., Kostur, M., Talkner, P., Hänggi, P., & Wixforth, A. (2008). Flow patterns and transport in Rayleigh surface acoustic wave streaming: Combined finite element method and raytracing numerics versus experiments. *IEEE Transactions on Ultrasonics, Ferroelectrics, and Frequency Control*, *55*(10), 2298–2305. https://doi.org/10.1109/TUFFC.928

Fu, Y. Q., Luo, J. K., Nguyen, N. T., Walton, A. J., Flewitt, A. J., Zu, X. T., … Milne, W. I. (2017). Advances in piezoelectric thin films for acoustic biosensors, acoustofluidics and lab-on-chip applications. *Progress in Materials Science*. https://doi.org/10.1016/j.pmatsci.2017.04.006

Gehrig, J., Reischl, M., Va Kalmár, Ẽ, Ferg, M., Hadzhiev, Y., Zaucker, A., … Müller, F. (2009). Automated high-throughput mapping of promoter-enhancer interactions in zebrafish embryos. *Nature Methods*, *6*(12), 911–916. https://doi.org/10.1038/nmeth.1396

Ghanem, M. A., Maxwell, A. D., Wang, Y.-N., Cunitz, B. W., Khokhlova, V. A., Sapozhnikov, O. A., & Bailey, M. R. (2020). Noninvasive acoustic manipulation of objects in a living body. *Proceedings of the National Academy of Sciences*, *117*(29), 16848–16855.

Goessling, W., North, T. E., & Zon, L. I. (2007). Ultrasound biomicroscopy permits in vivo characterization of zebrafish liver tumors. *Nature Methods*, *4*(7), 551–553.

Gor'kov, L. (n.d.). On the forces acting on a small particle in an acoustic field in an ideal fluid, 1962. In *Sov. Phys. Dokl* (Vol. 6, p. 773).

Gu, Y., Chen, C., Mao, Z., Bachman, H., Becker, R., Rufo, J., … Yang, S. (2021). Acoustofluidic centrifuge for nanoparticle enrichment and separation. *Science Advances*, *7*(1), eabc0467.

Gu, Y., Chen, C., Rufo, J., Shen, C., Wang, Z., Huang, P.-H., … Huang, T. J. (2020). Acoustofluidic Holography for Micro- to Nanoscale Particle Manipulation. *ACS Nano*, *14*(11), 14635–14645. https://doi.org/10.1021/acsnano.0c03754

Guo, F., Li, P., French, J. B., Mao, Z., Zhao, H., Li, S., … Huang, T. J. (2015). Controlling cell–cell interactions using surface acoustic waves. *Proceedings of the National Academy of Sciences*, *112*(1), 43–48. https://doi.org/10.1073/pnas.1422068112

Guo, F., Mao, Z., Chen, Y., Xie, Z., Lata, J. P., Li, P., … Dao, M. (2016). Three-dimensional manipulation of single cells using surface acoustic waves. *Proceedings of the National Academy of Sciences*, *113*(6), 1522–1527.

Guo, F., Mao, Z., Chen, Y., Xie, Z., Lata, J. P., Li, P., … Huang, T. J. (2016). Three-dimensional manipulation of single cells using surface acoustic waves. *Proceedings of the National Academy of Sciences*, *113*(6), 1522–1527. https://doi.org/10.1073/pnas.1524813113

Hallgrimsson, B., Percival, C. J., Green, R., Young, N. M., Mio, W., & Marcucio, R. (2015). Morphometrics, 3D imaging, and craniofacial development. In *Current topics in developmental biology* (Vol. 115, pp. 561–597). Elsevier.

Hansen, C. H. (2001). Fundamentals of acoustics. *Occupational Exposure to Noise: Evaluation, Prevention and Control. World Health Organization*, 23–52.

Henn, K., & Braunbeck, T. (2011). Dechorionation as a tool to improve the fish embryo toxicity test (FET) with the zebrafish (Danio rerio). *Comparative Biochemistry and Physiology Part C: Toxicology & Pharmacology*, *153*(1), 91–98.

Hirayama, R., Plasencia, D. M., Masuda, N., & Subramanian, S. (2019). A volumetric display for visual, tactile and audio presentation using acoustic trapping. *Nature*, *575*(7782), 320–323.

Holmgren, O., Makkonen, T., Knuutila, J. V., Kalo, M., Plessky, V. P., & Steichen, W. (2007). Side radiation of Rayleigh waves from synchronous SAW resonators. *IEEE Transactions on Ultrasonics, Ferroelectrics, and Frequency Control*, *54*(4), 861–869. https://doi.org/10.1109/TUFFC.2007.320

Howarth, D. L., Passeri, M., & Sadler, K. C. (2011). Drinks Like a Fish: Using Zebrafish to Understand Alcoholic Liver Disease. *Alcoholism: Clinical and Experimental Research*, *35*(5), 826–829. https://doi.org/10.1111/j.1530-0277.2010.01407.x

Howe, D. G., Bradford, Y. M., Eagle, A., Fashena, D., Frazer, K., Kalita, P., … Westerfield, M. (2017). The Zebrafish Model Organism Database: New support for human disease models, mutation details, gene expression phenotypes and searching. *Nucleic Acids Research*, *45*(D1), D758–D768. https://doi.org/10.1093/nar/gkw1116

Huang, P.-H., Nama, N., Mao, Z., Li, P., Rufo, J., Chen, Y., … Huang, T. J. (2014). A reliable and programmable acoustofluidic pump powered by oscillating sharp-edge structures. *Lab Chip*, *14*(22), 4319–4323. https://doi.org/10.1039/C4LC00806E

Inoue, S., Nakamura, K., Nakazawa, H., Tsutsumi, J., Ueda, M., & Satoh, Y. (2013). Analysis of Rayleigh wave radiations from leaky SAW resonators. *IEEE International Ultrasonics Symposium, IUS*, 1953–1956.

https://doi.org/10.1109/ULTSYM.2013.0498

Kannan, T. (2006). Finite Element Analysis of Surface Acoustic Wave Resonators. *Doctoral Dissertation*, 1–115. Retrieved from http://scholar.google.com/scholar?hl=en&btnG=Search&q=intitle:Finite+Element+Analysis+of+Surface+Acoustic+Wave+Resonators#0

Kari, G., Rodeck, U., & Dicker, A. P. (2007). Zebrafish: An emerging model system for human disease and drug discovery. *Clinical Pharmacology and Therapeutics*, *82*(1), 70–80. https://doi.org/10.1038/sj.clpt.6100223

Karimi, M., & Akdogan, G. (2012). Comparison of different drag coefficient correlations in the CFD modelling of a Laboratory-Scale Rushton-Turbine Flotation Tank. *The Ninth International ….*

Karlsson, J., Von Hofsten, J., & Olsson, P. E. (2001). Generating transparent zebrafish: A refined method to improve detection of gene expression during embryonic development. *Marine Biotechnology*, *3*(6), 522–527. https://doi.org/10.1007/s1012601-0053-4

King, L. V. (1934). On the acoustic radiation pressure on spheres. *Proceedings of the Royal Society of London. Series A-Mathematical and Physical Sciences*, *147*(861), 212–240.

Kinsler, L. E., Frey, A. R., Coppens, A. B., & Sanders, J. V. (1999). *Fundamentals of acoustics*. John wiley & sons.

Koskela, J., Knuuttila, J. V., Makkonen, T., Plessky, V. P., & Salomaa, M. M. (2001). Acoustic loss mechanisms in leaky SAW resonators on lithium tantalate. *IEEE Transactions on Ultrasonics, Ferroelectrics, and Frequency Control*, *48*(6), 1517–1526. https://doi.org/10.1109/58.971702

Lei, J., Hill, M., & Glynne-Jones, P. (2014). Numerical simulation of 3D boundary-driven acoustic streaming in microfluidic devices. *Lab on a Chip*, *14*(3), 532–541. https://doi.org/10.1039/c3lc50985k

Li, B., & Kwok, D. Y. (2003). Discrete Boltzmann Equation for Microfluidics. *Physical Review Letters*, *90*(12), 4. https://doi.org/10.1103/PhysRevLett.90.124502

Li, H., Friend, J. R., & Yeo, L. Y. (2007). A scaffold cell seeding method driven by surface acoustic waves. *Biomaterials*, *28*(28), 4098–4104.

Li, P., Mao, Z., Peng, Z., Zhou, L., Chen, Y., Huang, P.-H., … Dao, M. (2015). Acoustic

separation of circulating tumor cells. *Proceedings of the National Academy of Sciences*, *112*(16), 4970–4975.

Li, X., Gao, A., Wang, Y., Chen, M., Peng, J., Yan, H., … Chen, D. (2016). Alcohol exposure leads to unrecoverable cardiovascular defects along with edema and motor function changes in developing zebrafish larvae. *Biology Open*, *5*(8), 1128–1133.

Lighthill, S. J. (1978). Acoustic streaming. *Journal of Sound and Vibration*, *61*(3), 391–418. https://doi.org/10.1016/0022-460X(78)90388-7

Łodygowski, T., & Sumelka, W. (2006). Limitations in application of finite element method in acoustic numerical simulation. *Journal of Theoretical and Applied Mechanics*, *44*(4), 849–865. Retrieved from http://yadda.icm.edu.pl/baztech/element/bwmeta1.element.baztech-article-BWM2-0056-0037

Lu, G., Duan, Y. Y., & Wang, X. D. (2015). Experimental study on the dynamic wetting of dilute nanofluids. *Colloids and Surfaces A: Physicochemical and Engineering Aspects*, *486*, 6–13. https://doi.org/10.1016/j.colsurfa.2015.09.009

MacRae, C. A., & Peterson, R. T. (2015). Zebrafish as tools for drug discovery. *Nature Reviews Drug Discovery*, *14*(10), 721–731. https://doi.org/10.1038/nrd4627

Manor, O., Yeo, L. Y., & Friend, J. R. (2012). The appearance of boundary layers and drift flows due to high-frequency surface waves. *Journal of Fluid Mechanics*, *707*, 482–495. https://doi.org/10.1017/jfm.2012.293

Mao, Z., Li, P., Wu, M., Bachman, H., Mesyngier, N., Guo, X., … Huang, T. J. (2017). Enriching Nanoparticles via Acoustofluidics. *ACS Nano*, *11*(1), 603–612. https://doi.org/10.1021/acsnano.6b06784

Martel, J. M., & Toner, M. (2014). Inertial focusing in microfluidics. *Annual Review of Biomedical Engineering*, *16*, 371–396.

Martinez-Sales, M., García-Ximénez, F., & Espinós, F. (2014). Zebrafish (Danio rerio) as a possible bioindicator of epigenetic factors present in drinking water that may affect reproductive function: Is chorion an issue? *Zygote*, *23*(3), 447–452. https://doi.org/10.1017/S0967199414000045

Marzo, A., Seah, S. A., Drinkwater, B. W., Sahoo, D. R., Long, B., & Subramanian, S. (2015). Holographic acoustic elements for manipulation of levitated objects. *Nature*

Communications, *6*(1), 1–7.

Melde, K., Mark, A. G., Qiu, T., & Fischer, P. (2016). Holograms for acoustics. *Nature*, *537*(7621), 518–522. https://doi.org/10.1038/nature19755

Mitchell, A. J., & Wimpenny, J. W. T. (1997). The effects of agar concentration on the growth and morphology of submerged colonies of motile and non-motile bacteria. *Journal of Applied Microbiology*, *83*(1), 76–84. https://doi.org/10.1046/j.1365-2672.1997.00192.x

Morgan, D. R. (1973). Surface acoustic wave devices and applications: 1. Introductory review. *Ultrasonics*, *11*(3), 121–131.

Muller, P. B., & Bruus, H. (2015). Theoretical study of time-dependent, ultrasound-induced acoustic streaming in microchannels. *Physical Review E - Statistical, Nonlinear, and Soft Matter Physics*, *92*(6), 1–13. https://doi.org/10.1103/PhysRevE.92.063018

Murochi, N., Sugimoto, M., Matsui, Y., & Kondoh, J. (2007). Deposition of thin film using a surface acoustic wave device. *Japanese Journal of Applied Physics*, *46*(7S), 4754.

Mutafopulos, K., Lu, P. J., Garry, R., Spink, P., & Weitz, D. A. (2020). Selective cell encapsulation, lysis, pico-injection and size-controlled droplet generation using traveling surface acoustic waves in a microfluidic device. *Lab on a Chip*, *20*(21), 3914–3921.

Nama, N., Barnkob, R., Mao, Z., Kähler, C. J., Costanzo, F., & Huang, T. J. (2015). Numerical study of acoustophoretic motion of particles in a PDMS microchannel driven by surface acoustic waves. *Lab Chip*, *15*(12), 2700–2709. https://doi.org/10.1039/C5LC00231A

Nama, N., Huang, P.-H., Huang, T. J., & Costanzo, F. (2014). Investigation of acoustic streaming patterns around oscillating sharp edges. *Lab Chip*, *14*(15), 2824–2836. https://doi.org/10.1039/C4LC00191E

Ozcelik, A., Nama, N., Huang, P., Kaynak, M., McReynolds, M. R., Hanna-Rose, W., & Huang, T. J. (2016). Acoustofluidic rotational manipulation of cells and organisms using oscillating solid structures. *Small*, *12*(37), 5120–5125.

Ozcelik, A., Rufo, J., Guo, F., Gu, Y., Li, P., Lata, J., & Huang, T. J. (2018). Acoustic tweezers for the life sciences. *Nature Methods*, *15*(12), 1021–1028. https://doi.org/10.1038/s41592-018-0222-9

Pardo-Martin, C., Allalou, A., Medina, J., Eimon, P. M., Wahlby, C., & Yanik, M. F. (2013). High-throughput hyperdimensional vertebrate phenotyping. *Nature Communications*, *4*. https://doi.org/10.1038/ncomms2475

Pardo-Martin, C., Chang, T. Y., Koo, B. K., Gilleland, C. L., Wasserman, S. C., & Yanik, M. F. (2010). High-throughput in vivo vertebrate screening. *Nature Methods*, *7*(8), 634–636. https://doi.org/10.1038/nmeth.1481

Passeri, M. J., Cinaroglu, A., Gao, C., & Sadler, K. C. (2009). Hepatic steatosis in response to acute alcohol exposure in zebrafish requires sterol regulatory element binding protein activation. *Hepatology*, *49*(2), 443–452. https://doi.org/10.1002/hep.22667

Pulak, R. (2016). Tools for automating the imaging of zebrafish larvae. *Methods*, *96*, 118–126.

Rajapaksa, A., Qi, A., Yeo, L. Y., Coppel, R., & Friend, J. R. (2014). Enabling practical surface acoustic wave nebulizer drug delivery via amplitude modulation. *Lab on a Chip*, *14*(11), 1858–1865.

Rayleigh, Lord. (1879). On the capillary phenomena of jets. *Proc. R. Soc. London*, *29*(196–199), 71–97.

Rayleigh, Lord. (1884). On the circulation of air observed in Kundt's tubes and on some allied acoustical problems. *Philosophical Transactions of the Royal Society of London*, *175*, 1–21. https://doi.org/10.1098/rspb.201

Rayleigh, Lord. (1902). XXXIV. on the pressure of vibrations. *The London, Edinburgh, and Dublin Philosophical Magazine and Journal of Science*, *3*(15), 338–346.

Sadhal, S. S. (2012). Acoustofluidics 13: Analysis of acoustic streaming by perturbation methods. *Lab on a Chip*, *12*(13), 2292–2300. https://doi.org/10.1039/c2lc40202e

Salim, Z. T., Hashim, U., & Arshad, M. K. M. (2016). FEM Modeling and Simulation of a Layered SAW device Based on ZnO / 128 ° YX LiNbO 3. *IEEE ICSE Proc.*, 5–8.

Sano, A., Matsui, Y., & Shiokawa, S. (1998). New manipulator based on surface acoustic wave streaming. *Japanese Journal of Applied Physics*, *37*(5S), 2979.

Schmidt, E. J., Parsons, T. E., Jamniczky, H. A., Gitelman, J., Trpkov, C., Boughner, J. C., … Hallgrímsson, B. (2010). Micro-computed tomography-based phenotypic approaches in embryology: procedural artifacts on assessments of embryonic craniofacial growth and development. *BMC Developmental Biology*, *10*(1), 18.

Shilton, R. J., Travagliati, M., Beltram, F., & Cecchini, M. (2014). Nanoliter-droplet acoustic streaming via ultra high frequency surface acoustic waves. *Advanced Materials*, *26*(29), 4941–4946. https://doi.org/10.1002/adma.201400091

Singh, M., Raghunathan, R., Piazza, V., Davis-Loiacono, A. M., Cable, A., Vedakkan, T. J., … Wu, C. (2016). Applicability, usability, and limitations of murine embryonic imaging with optical coherence tomography and optical projection tomography. *Biomedical Optics Express*, *7*(6), 2295–2310.

Strobl, K., Schneider, M. F., Wixforth, A., Sritharan, K., & Guttenberg, Z. (2006). Acoustic mixing at low Reynolds number. *Applied Physics Letters*, *88*, 54102.

Tan, J. L., & Zon, L. I. (2011). Chemical Screening in Zebrafish for Novel Biological and Therapeutic Discovery. *Methods in Cell Biology*, *105*, 491–516. https://doi.org/10.1016/B978-0-12-381320-6.00021-7

Tan, M. K., Friend, J. R., Matar, O. K., & Yeo, L. Y. (2010). Capillary wave motion excited by high frequency surface acoustic waves. *Physics of Fluids*, *22*(11). https://doi.org/10.1063/1.3505044

Teixidó, E., Kießling, T. R., Krupp, E., Quevedo, C., Muriana, A., & Scholz, S. (2019). Automated Morphological Feature Assessment for Zebrafish Embryo Developmental Toxicity Screens. *Toxicological Sciences*, *167*(2), 438–449. https://doi.org/10.1093/toxsci/kfy250

Terry, S. C., Jerman, J. H., & Angell, J. B. (1979). A gas chromatographic air analyzer fabricated on a silicon wafer. *IEEE Transactions on Electron Devices*, *26*(12), 1880–1886.

Tseng, W.-K., Lin, J.-L., Sung, W.-C., Chen, S.-H., & Lee, G.-B. (2006). Active micro-mixers using surface acoustic waves on Y-cut 128 LiNbO3. *Journal of Micromechanics and Microengineering*, *16*(3), 539.

Viktorov, I. A. (1967). *Rayleigh and Lamb waves: physical theory and applications. Transl. from Russian. With a foreword by Warren P. Mason*. Plenum press.

Vinegoni, C., Fexon, L., Feruglio, P. F., Pivovarov, M., Figueiredo, J.-L., Nahrendorf, M., … Weissleder, R. (2009). High throughput transmission optical projection tomography using low cost graphics processing unit. *Optics Express*, *17*(25), 22320–22332.

Ward, A. C., & Lieschke, G. J. (2002). The zebrafish as a model system for human

disease. *Frontiers in Bioscience : A Journal and Virtual Library*, *7*, 827–833. https://doi.org/10.2741/ward

wikipedia. (n.d.-a). https://en.wikipedia.org/wiki/Acoustic_wave.

wikipedia. (n.d.-b). https://en.wikipedia.org/wiki/Smoothed-particle_hydrodynamics.

Wiklund, M., Green, R., & Ohlin, M. (2012). Acoustofluidics 14: Applications of acoustic streaming in microfluidic devices. *Lab on a Chip*, *12*(14), 2438–2451.

Wu, M., Ouyang, Y., Wang, Z., Zhang, R., Huang, P.-H., Chen, C., … Dao, M. (2017). Isolation of exosomes from whole blood by integrating acoustics and microfluidics. *Proceedings of the National Academy of Sciences*, 201709210.

Yang, F., Gao, C., Wang, P., Zhang, G. J., & Chen, Z. (2016). Fish-on-a-chip: Microfluidics for zebrafish research. *Lab on a Chip*, *16*(7), 1106–1125. https://doi.org/10.1039/c6lc00044d

Yang, Y., Ma, T., Li, S., Zhang, Q., Huang, J., Liu, Y., … Niu, L. (2021). Self-Navigated 3D Acoustic Tweezers in Complex Media Based on Time Reversal. *Research*, *2021*.

Yang, Z., Cole, K. L. H., Qiu, Y., Somorjai, I. M. L., Wijesinghe, P., Nylk, J., … Dholakia, K. (2019). Light sheet microscopy with acoustic sample confinement. *Nature Communications*, *10*(1), 1–8. https://doi.org/10.1038/s41467-019-08514-5

Yanik, M. F., Rohde, C. B., & Pardo-Martin, C. (2011). *Technologies for Micromanipulating, Imaging, and Phenotyping Small Invertebrates and Vertebrates*. *Annual Review of Biomedical Engineering* (Vol. 13). https://doi.org/10.1146/annurev-bioeng-071910-124703

Yeo, L. Y., & Friend, J. R. (2009). Ultrafast microfluidics using surface acoustic waves. *Biomicrofluidics*, *3*(1), 012002. https://doi.org/10.1063/1.3056040

Yilmaz, F., & Gundogdu, M. Y. (2009). Analysis of conventional drag and lift models for multiphase CFD modeling of blood flow. *Korea-Australia Rheology Journal*, *21*(3), 161–173.

Yosioka, K., & Kawasima, Y. (1955). Acoustic radiation pressure on a compressible sphere. *Acta Acustica United with Acustica*, *5*(3), 167–173.

Zang, L., Maddison, L. A., & Chen, W. (2018). Zebrafish as a model for obesity and diabetes. *Frontiers in Cell and Developmental Biology*, *6*, 91.

Zhang, J., Hartman, J. H., Chen, C., Yang, S., Li, Q., Tian, Z., … Huang, T. J. (2020). Fluorescence-based sorting of Caenorhabditis elegans via acoustofluidics. *Lab on a Chip*, *20*(10), 1729–1739.

Zhang, J., Yang, S., Chen, C., Hartman, J. H., Huang, P. H., Wang, L., … Huang, T. J. (2019). Surface acoustic waves enable rotational manipulation of Caenorhabditis elegans. *Lab on a Chip*, *19*(6), 984–992. https://doi.org/10.1039/C8LC01012A

Zhang, S. P., Lata, J., Chen, C., Mai, J., Guo, F., Tian, Z., … Li, P. (2018). Digital acoustofluidics enables contactless and programmable liquid handling. *Nature Communications*, *9*.

Biography

Chuyi Chen earned her bachelor's degree of science in 2013 from Nanjing University, Jiangsu, China. In 2016, she obtained her master's degree of science in physics from Nanjing University. After that, she joined the Acoustofluidic Lab in the Department of Mechanical Engineering and Materials Science at Duke University. Following is a list of her publications:

1. **Chen, C.**, Gu, Y., Philippe, J., Zhang, P., Bachman, H., Zhang, J., Mai, J., Rufo, J., Rawls, J.F., Davis, E.E., Katsanis, N. and Huang, T.J., 2021. **Acoustofluidic Rotational Tweezing Enables High-Speed Contactless Morphological Phenotyping of Zebrafish Larvae.** *Nature Communications*, 12(1), pp.1-13.

2. **Chen, C.**, Zhang, S.P., Mao, Z., Nama, N., Gu, Y., Huang, P.H., Jing, Y., Guo, X., Costanzo, F. and Huang, T.J., 2018. **Three-dimensional numerical simulation and experimental investigation of boundary-driven streaming in surface acoustic wave microfluidics.** *Lab on a Chip*, 18(23), pp.3645-3654.

3. **Chen, C.**, Zhang, P., Mao, Z., Gu, Y., Costanzo, F. and Huang, T.J., 2018. **Inter-digital transducers activated acoustic streaming in viscous liquid.** *The Journal of the Acoustical Society of America*, 143(3), pp.1753-1753.

4. **Chen, C.**, Gu, Y., Tu, J., Guo, X. and Zhang, D., 2016. **Microbubble oscillating in a microvessel filled with viscous fluid: A finite element modeling study.** *Ultrasonics*, 66, pp.54-64.

5. Gu, Y., **Chen, C.**, Mao, Z., Bachman, H., Becker, R., Rufo, J., Wang, Z., Zhang, P., Mai, J., Yang, S., Zhang, J., Zhao, S., Ouyang, Y., Wong, D.T.W., Sadovsky, Y. and Huang, T.J., 2020. **Acoustofluidic centrifuge for nanoparticle enrichment and separation.** *Science Advances*, 7(1), p.eabc0467.

6. Gu, Y., **Chen, C.**, Rufo, J., Shen, C., Wang, Z., Huang, P.H., Fu, H., Zhang, P., Cummer, S.A., Tian, Z. and Huang, T.J., 2020. **Acoustofluidic Holography for Micro-to Nanoscale Particle Manipulation.** *ACS nano*, 14, pp.14635-14645.

7. Zhang, P., **Chen, C.**, Su, X., Mai, J., Gu, Y., Tian, Z., Zhu, H., Zhong, Z., Fu, H., Yang, S. and Chakrabarty, K., 2020. **Acoustic streaming vortices enable contactless, digital control of droplets.** *Science Advances*, 6(24), p.eaba0606.

8. Bachman, H., **Chen, C.**, Rufo, J., Zhao, S., Yang, S., Tian, Z., Nama, N., Huang, P.H. and Huang, T.J., 2020. **An acoustofluidic device for efficient mixing over a wide range of flow rates.** *Lab on a Chip*, 20(7), pp.1238-1248.

9. Gu, Y., **Chen, C.**, Wang, Z., Huang, P.H., Fu, H., Wang, L., Wu, M., Chen, Y., Gao, T., Gong, J. and Kwun, J., 2019. **Plastic-based acoustofluidic devices for high-throughput, biocompatible platelet separation.** *Lab on a Chip*, 19(3), pp.394-402.

10. Wu, M., **Chen, C.**, Wang, Z., Bachman, H., Ouyang, Y., Huang, P.H., Sadovsky, Y. and Huang, T.J., 2019. **Separating extracellular vesicles and lipoproteins via acoustofluidics.** *Lab on a Chip*, 19(7), pp.1174-1182.

11. Zhang, P., **Chen, C.**, Guo, F., Philippe, J., Gu, Y., Tian, Z., Bachman, H., Ren, L., Yang, S., Zhong, Z. and Huang, P.H., 2019. **Contactless, programmable acoustofluidic manipulation of objects on water.** *Lab on a Chip*, 19(20), pp.3397-3404.

12. Zhang, S.P., Lata, J., **Chen, C.**, Mai, J., Guo, F., Tian, Z., Ren, L., Mao, Z., Huang, P.H., Li, P. and Yang, S., 2018. **Digital acoustofluidics enables contactless and programmable liquid handling.** *Nature Communications*, 9(1), pp.1-11.

13. Gu, Y., **Chen, C.**, Wang, Z., Huang, P.H., Fu, H. and Huang, T.J., 2018. Disposable device for human plateletpheresis. *The Journal of the Acoustical Society of America*, 143(3), pp.1928-1929.

14. Gu, Y., **Chen, C.**, Tu, J., Guo, X., Wu, H. and Zhang, D., 2016. **Harmonic responses and cavitation activity of encapsulated microbubbles coupled with magnetic nanoparticles.** *Ultrasonics Sonochemistry*, 29, pp.309-316.

15. Zhang, J., Hartman, J.H., **Chen, C.**, Yang, S., Li, Q., Tian, Z., Huang, P.H., Wang, L., Meyer, J.N. and Huang, T.J., 2020. **Fluorescence-based sorting of Caenorhabditis elegans via acoustofluidics.** *Lab on a Chip*, 20(10), pp.1729-1739.

16. Zhao, S., Wu, M., Yang, S., Wu, Y., Gu, Y., **Chen, C.**, Ye, J., Xie, Z., Tian, Z., Bachman, H. and Huang, P.H., 2020. **A disposable acoustofluidic chip for nano/microparticle separation using unidirectional acoustic transducers.** *Lab on a Chip*, 20(7), pp.1298-1308.

17. Wang, Z., Li, F., Rufo, J., **Chen, C.**, Yang, S., Li, L., Zhang, J., Cheng, J., Kim, Y., Wu, M. and Abemayor, E., 2020. **Acoustofluidic Salivary Exosome Isolation: A Liquid Biopsy Compatible Approach for Human Papillomavirus–Associated Oropharyngeal Cancer Detection.** *The Journal of Molecular Diagnostics*, 22(1), pp.50-59.

18. Tian, Z., Yang, S., Huang, P.H., Wang, Z., Zhang, P., Gu, Y., Bachman, H., **Chen, C.**, Wu, M., Xie, Y. and Huang, T.J., 2019. **Wave number–spiral acoustic tweezers for dynamic and reconfigurable manipulation of particles and cells.** *Science Advances*, 5(5), p.eaau6062.

19. Zhang, J., Yang, S., **Chen, C.**, Hartman, J.H., Huang, P.H., Wang, L., Tian, Z., Zhang, P., Faulkenberry, D., Meyer, J.N. and Huang, T.J., 2019. **Surface acoustic waves enable rotational manipulation of Caenorhabditis elegans.** *Lab on a Chip*, 19(6), pp.984-992.

20. Wang, Z., Huang, P.H., **Chen, C.**, Bachman, H., Zhao, S., Yang, S. and Huang, T.J., 2019. **Cell lysis via acoustically oscillating sharp edges.** *Lab on a Chip*, 19(24), pp.4021-4032.

21. Huang, P.H., Zhao, S., Bachman, H., Nama, N., Li, Z., **Chen, C.**, Yang, S., Wu, M., Zhang, S.P. and Huang, T.J., 2019. **Acoustofluidic synthesis of particulate nanomaterials.** *Advanced Science*, 6(19), p.1900913.
22. Wu, M., Huang, P.H., Zhang, R., Mao, Z., **Chen, C.**, Kemeny, G., Li, P., Lee, A.V., Gyanchandani, R., Armstrong, A.J. and Dao, M., 2018. **Circulating Tumor Cell Phenotyping via High-Throughput Acoustic Separation.** *Small*, 14(32), p.1801131.
23. Wu, M., Ouyang, Y., Wang, Z., Zhang, R., Huang, P.H., **Chen, C.**, Li, H., Li, P., Quinn, D., Dao, M. and Suresh, S., 2017. **Isolation of exosomes from whole blood by integrating acoustics and microfluidics.** *Proceedings of the National Academy of Sciences*, 114(40), pp.10584-10589.